Montanuniversität Leoben- University of Leoben
Department Metallurgie - Department of Metallurgy
Nichteisenmetallurgie - Nonferrous Metallury

DIPLOMA THESIS

topic:

Influence of microalloying elements on the precipitation behavior of Al-Mg-Si alloys

Eidgenössische Technische Hochschule Zürich
Swiss Federal Institute of Technology Zurich

by:

Marion Werinos

under supervision of:

Univ.-Prof.Dipl.-Ing.Dr.mont. Helmut Antrekowitsch

Dipl.-Ing. Stefan Pogatscher

Univ.-Prof.Dipl.-Ing.Dr.mont. Peter Uggowitzer

in cooperation with:

Laboratory of Metal Physics and Technology (LMPT), ETH Zurich

Leoben, June 2012

Influence of microalloying elements on the precipitation behavior of Al-Mg-Si alloys

Amag Austria Metall AG is a manufacturer of aluminum semi-finished products delivering a significant amount of Al-Mg-Si alloys. Most industrially important age-hardenable Al-Mg-Si alloys show a so-called adverse effect of natural pre-aging on artificial aging which negatively influences not only the age hardening kinetics but also the hardening potential during artificial aging.

The aim of this work is to find a way to prohibit or weaken this negative effect of natural pre-aging on artificial aging by the addition of microalloying elements to the widely used aluminum wrought alloy AA6061.

A broad literature research should provide the basis for the interpretation of experimental results. After an introduction into the precipitation sequence in Al-Mg-Si alloys and fundamentals of vacancy assisted diffusion, theories treating the negative effect should be examined more closely. A theory developed at the Chair of Nonferrous Metallurgy regarding interactions between the main alloying elements Si and Mg with quenched-in vacancies as the main reason for the negative effect of natural pre-aging on artificial aging should be linked to the effect of microalloying elements. Therefore a detailed study focusing on the role of solute-vacancy interactions in an aluminum host has to be performed.

The selection of microalloying elements should be aided by knowledge gained out of the literature research and thermodynamic calculations. Hardness measurements, atom probe tomography, optical emission spectroscopy and inductively coupled plasma mass spectrometry, are to be used as material characterization methods.

Leoben, June 2012

Eidesstattliche Erklärung

Ich erkläre an Eides statt, dass ich diese Arbeit selbständig und ohne fremde Hilfe verfasst, andere als die angegebenen Quellen und Hilfsmittel nicht benutzt, wörtlich und inhaltlich entnommene Stellen als solche kenntlich gemacht habe.

I declare in lieu of oath, that I wrote this thesis and performed the associated research myself, using only literature cited in this volume.

Marion Werinos

Leoben, June 2012

Acknowledgements

Especially I would like to thank Stefan Pogatscher, who arouse my interest in the topic and like that persuaded me to start with this thesis. Also thank you for your guidance, your advices and for always so spontaneously taking your time for me.

I am also grateful to Prof. Helmut Antrekowitsch, the head of the Chair of Nonferrous Metallurgy, for giving me the opportunity to carry out this thesis and reviewing it.

Further special thanks to Prof. Peter Uggowitzer from the ETH Zurich for his support, advises and the survey of this thesis. He made it possible for me to work with Frank Moszner in carrying out the atom probe tomography analyses at the ETH Zurich. I had the pleasure to get to know him personally during my trip to his Laboratory of Metal Physics and Technology.

Many thanks to Thomas Link and also Erich Troger from the Chair of Nonferrous Metallurgy for having so much patience in preparing and analyzing my samples for this thesis. I am also thankful to Thomas Ebner from Amag Rolling, who carried out the rolling process of the main study samples.

In general I want to thank all colleagues from the Chair of Nonferrous Metallurgy for the amusing time and their help. I gained many friends and I am looking forward to doing my PHD with you as colleagues.

Special thanks to all friends for the great time in Leoben and the many experiences we shared. Most of all I would like to thank Astrid Wachauer and her partner Franz J. Schmied for helping with software related problems.

Inexpressible thanks to my entire family and my boyfriend who always so much supported my study in Leoben.

Furthermore, I want to thank Amag Rolling for providing sample material and the possibility to carry on with this work in the framework of my dissertation.

Abstract

This work deals with a phenomenon called the negative effect of natural pre-aging on artificial aging, shown by many industrial important Al-Mg-Si alloys. An extensive literature research including the precipitation sequence in Al-Mg-Si alloys, fundamentals of vacancy assisted diffusion and theories treating the negative effect, served as a basis for the interpretation of experimental results. The approach of the work is based on a theory regarding interactions between the main alloying elements Si and Mg with quenched-in vacancies as the main reason for the negative effect of natural pre-aging on artificial aging. In the experimental part selected microalloying elements (Li, Ca, Sr, Ba, Ag, Cd, In, Ge, Sn, Sb, Pb and Bi) were added to the industrial important alloy AA6061. Some of these microalloying elements are believed to interact with vacancies in the aluminum matrix and are able to prohibit the negative effect of natural pre-aging on artificial aging. Using calculations from literature-based data of element-vacancy interactions in pure aluminum facilitated not only to verify the aforementioned theory, but also to interpret the effect which some tested microalloying elements exhibited on the overall precipitation kinetics of AA6061.

Kurzfassung

Diese Arbeit befasst sich mit dem Phänomen des negativen Effektes einer Kaltauslagerung auf die nachfolgende Warmauslagerung in Al-Mg-Si-Legierungen. Eine umfangreiche Literaturrecherche behandelt die Ausscheidungssequenz in Al-Mg-Si-Legierungen, Grundlagen der leerstellenunterstützten Diffusion und Theorien zu dem negativen Kaltauslagerungseffekt und diente weiters als Basis zur Interpretation experimenteller Ergebnisse. Der gewählte Ansatz basiert auf einer Theorie, welche Interaktionen zwischen den Hauptlegierungselementen Si und Mg mit eingeschreckten Leerstellen als den Grund für den negativen Kaltauslagerungseffekt auf eine nachfolgende Wärmebehandlung erachtet. Im experimentellen Teil erfolgte die Zugabe von ausgewählten Mikrolegierungselementen (Li, Ca, Sr, Ba, Ag, Cd, In, Ge, Sn, Sb, Pb und Bi) zur industriell wichtigen Legierung AA6061, da von einigen dieser Mikrolegierungselemente angenommen wird, dass sie mit Leerstellen interagieren und den negativen Kaltauslagerungseffekt auf die nachfolgende Wärmebehandlung verhindern könnten. Berechnungen unter Verwendung von Literaturdaten zu Element-Leerstellen-Interaktionen in Reinaluminium ermöglichten nicht nur eine Verifizierung der zuvor erwähnten Theorie, sondern auch den Effekt, welchen einige der getesteten Mikrolegierungselemente auf die Ausscheidungskinetik in AA6061 aufwiesen, zu interpretieren.

Contents

1 Introduction

After Alfred Wilm more than 100 years ago accidentally discovered aging in an Al-Cu-Mg alloy, known today as the "2000" series of aluminum-based engineering alloys, it took about 30 years to explain how age hardening works. Only in 1939 Guinier and Preston could prove that small precipitates were responsible for this hardening although they weren't visible in the microscopes of those days. Not long after Wilm made his discovery, Al-Mg-Si alloys were developed in the 1920s.

Today the Al-Mg-Si alloy system is the basis of numerous age hardenable wrought and casting alloys. Due to another denotation they are also called 6xxx alloys. Al-Mg-Si alloys are used as construction materials in many different ways such as rolled, extruded, forged and die-cast products. They can be hardened by artificial aging (AA), i.e. by normally baking the solid solution at about 150 to 180 °C after quenching (note that all abbreviations are also listed at the end of this work among "Acronyms"). A characteristic property of many Al-Mg-Si alloys is the so-called adverse effect of room temperature (RT) "natural" aging on a subsequent AA step which was discovered a long time ago. The precipitates of Al-Mg-Si alloys which are responsible for the hardness maxima at natural and artificial aging are known since the end of the twentieth century though they couldn't be fully characterized till today. Further the role of the vacancy concentration, the Mg/Si-ratio, the nucleation mechanism of the initial and intermediate phases as well as their stability and transformation behavior only got clearer in recent decades [1–3].

To make the reader more sensitive about the background why the study of the exact microstructure evolution is so complicated for these alloys several reasons are now going to be outlined. Afterward one can much easier understand that age hardening in the technologically and economically less important Al-Cu has been studied more often and more successfully in the past [1]. Reasons are:

- Decisive processes happen on the nanometer level and are therefore not directly observable, even with high-resolution transmission electron microscopy (TEM) and Fourier-image analysis [2]
- The content of Mg and Si is very low, i.e. $\leq$1.5 or $\leq$1.2 wt.% for both elements [1]

- In addition Mg, Al, and Si are neighboring elements in the periodic table — this results in a very similar electron density for these three elements [1]

As a consequence of the last point X-rays, which interact with electrons, are diffracted from the different atoms in a similar way. X-ray small-angle scattering also yields weak signals from clusters enriched in Mg and Si that are embedded in an Aluminum (Al)-rich solid solution because the scattering length density difference between the cluster and the matrix, which controls scattering, is very small. Furthermore element contrast is low in electron microscopy as far as a Z-contrast is concerned. There are also no isotopes with scattering lengths that differ enough to enhance contrast. Of all the imaging techniques, only three-dimensional atom probe (3DAP) has the possibility to resolve the clusters formed during natural aging (NA). Direct visualization of these clusters formed during NA has only been successful for long aging times and in alloys with a high content of alloying elements. The present knowledge about the phase evolution during AA is therefore based on the interpretation of the results of indirect techniques such as thermal analysis, measurements of hardness, resistivity measurement, X-ray scattering, and positron annihilation spectroscopy (PAS). Mainly with the help of 3DAP and PAS important aspects of early precipitation processes became much clearer in recent years, but for Al-Mg-Si alloys they are still not fully resolved [1,2,4].

In the processing of Al-Mg-Si alloys it is practically unavoidable to have an intermediate storage at RT between quenching and AA. This is often also necessary because then forming is easily possible. But as NA can have a "negative" effect on AA by changing the age hardening potential and also the age hardening kinetics, it is worthy of detailed study [1,2].

As will be treated in more detail later in sections 2.1.2 and 2.1.4 the occurrence of a negative effect of NA seems to depend on the Mg content and the Mg:Si ratio, respectively. Typically alloys showing the negative response of AA after natural pre-aging (NPA) contain 0.5 to 1 wt.% of both Mg and Si [5]. Studies of Banhart et al. [4] with the help of positron annihilation lifetime spectroscopy (PALS) and differential scanning calorimetry (DSC) revealed the occurrence of a distinct NA stage, called "stage 1", for alloys showing this effect. The analyzed alloys in question possess high Mg content, 0.6 and 0.8 at.% Mg, and their Mg:Si ratio close to 1 seems to promote this stage [4]. Most industrial important Al-Mg-Si alloys are high-strength alloys which show this negative effect of NA on AA as they have to contain a high enough Mg- and Si-content to achieve reasonable precipitation hardening. Only exceptions of industrial relevant 6xxx alloys show a so-called positive effect of NA on AA. An example is the alloy 6060 with much lower Mg- and Si-content. Generally there are several possible reasons for this adverse effect of NA on the kinetics and response of AA discussed in literature which will be adressed later.

To understand now phenomena occurring during the processing, which can considerably influence the alloy properties, detailed knowledge about precipitation processes in Al-Mg-Si alloys during natural and AA is necessary. In the experimental part of this work the widely used aluminum wrought alloy AA6061 is studied. This alloy shows the so-called negative effect of NA on subsequent AA. The aim is to examine and understand the influence of selected microalloying (MA) elements on the precipitation process and hardness development. The role of vacancies in this process will be closely discussed as well.

Studies of Banhart et al. [1] in which only purely ternary alloys were used exhibit that the negative effect is observed already for very short NPA times. Even after 2 minutes of NPA the rate of initial hardening is reduced and the final peak hardness drops. They refer to literature in which the negative effect of NPA sets much slower, and linked this to be due to additional elements contained in engineering alloys. Their explanation is as follows: *"Some additional elements are known to slow down NA due to trapping of vacancies after quenching which are then no longer available to mediate the early clustering process."*

In general trace elements have been found to disproportionally influence structure and properties of Al alloys compared with the amounts added. Most of the trace element effects emerge because they modify the nucleation and/or growth characteristics of the phases which form during precipitation [6]. T. Sato accurately sums this up with [7]: *"Excess vacancies introduced by quenching are especially important in the cluster formation. It is necessary, therefore, to understand the relationship among MA elements, solute atoms, and vacancies to elucidate the fundamental mechanism of MA effects."*

In the light of this a detailed study of the effect of MA elements on the aging behavior of the technological important Al alloy AA6061 focussing also on the role of vacancies seems to be well justified.

2 Literature Review

Starting with a survey of the precipitation sequence in Al alloys and an introduction into derived theories regarding the negative influence of NPA on AA, this chapter further reviews the backgrounds of a theory this work is based on. Vacancies are believed to play an important role in the undesirable co-cluster formation during NA. Their interactions with solute atoms in Al are analyzed before several examples of known MA influences on the precipitation behavior of other Al systems are discussed.

2.1 Precipitation in Aluminum Alloys

One important fact to know is that precipitation sequences of Al alloys like they are frequently given in publications or books are never valid for any temperature. This means that the actual precipitate or precipitates that occur at a particular aging temperature may not form at all at other lower temperatures or they almost instantly evolve into others at higher temperatures, where they aren't stable anymore. There may also be ranges of co-existence of several of these phases. To give an example, for GP zones to form the aging must take place below the relevant GP zones solvus temperature (e.g. figure 2.5(a) in section 2.1.3). If precipitates of a later stage are formed, it is possible for them to nucleate either from pre-existing GP zones, at the sites of these zones, or independently in the matrix. At some aging temperatures, both GP zones and precipitates of a later stage can be present together [1,8].

As a consequence of the certainty that the complete precipitation process of Al-Mg-Si alloys is today recognized as the most complex of all age-hardened Al alloys [8], extracting and comparing information from the literature is to be sure difficult. Some reasons for this have already been mentioned in section 1. On the one hand the real precipitation sequence depends on the alloy composition and the possible presence of trace elements, on the other hand studies in literature are carried out with a lot of different alloys and aging conditions. A varying nomenclature and different mixture of phases found also help to the confusing situation [1]. Furthermore the quenching speed after the solution heat treatment and, as already mentioned earlier, a possible

intermediate storage at RT or in general NPA can considerably influence the precipitation kinetics as well as the formed precipitates [2].

2.1.1 Classification of Al-Mg-Si Alloys

Originally it was possible to divide Al-Mg-Si alloys into three groups depending on their Mg and Si content. These groups also indicate a rough guideline with regard to the strength levels that may be achieved in the T6 condition of individual alloys. Figure 2.1 shows the compositional limits and attainable strengths of some commercial alloys.

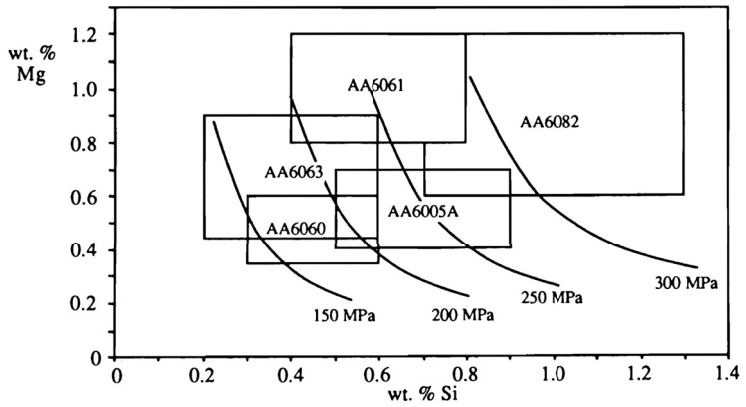

Figure 2.1: Compositional limits of some common Al-Mg-Si alloys, the curves represent common peak aged (T6) values of yield strength [8]

The first group contains alloys with balanced amounts of Mg and Si and a total amount of the two elements between 0.8 % and 1.2 %. One example is the alloy 6063, one of the most widely used of all Al-Mg-Si alloys. These alloys develop moderate strength by age-hardening at 160–190 °C [8].

In both the second and third group Mg and Si add up to more than 1.4 %. These alloys show higher strength on aging and are more quench sensitive than the first group. The second group has balanced compositions of Mg and Si. A common example is the alloy AA6061 (Al-1Mg-0.6Si) with additions of other elements like up to 0.25 % Cu and 0.2 % Cr. The exact composition of the alloy used in this work can be seen from table 4.1 in section 2.1.2. In this alloy Cu improves mechanical properties. The third group contains Si in excess of what is needed to form Mg_2Si. Through this additional Si the alloy has a higher response to age-hardening by both refining the size of the Mg_xSi_y precipitates and causing additional Si precipitates. But as Si has the tendency to segregate to grain boundaries in such alloys, lower ductility and intergranular embrittlement may be the consequence [8].

As will be treated in more detail in section 2.1, the intermediate precipitates which contribute most to the age hardening contain Mg:Si ratios close to 1:1 and not 2:1, as would be expected

because of the equilibrium phase β (Mg_2Si). As a consequence a new, fourth, series of alloys with lower Mg content has been developed. An example is the alloy AA6060 with the modified composition (Al-0.35Mg-0.5Si) which is comparable with the alloy AA6063 with regard to tensile properties, but better extrudable [8].

2.1.2 Precipitation Sequence in Al-Mg-Si Alloys

Figure 2.2 shows two DSC curves obtained by Miao and Laughlin (a) and Edwards (b). In figure 2.2(a) a corresponding hardness plot is pictured as well. With the help of these curves the general precipitation sequence of Al-Mg-Si alloys, as-quenched and heated in the DSC with constant heating rates, can be depicted.

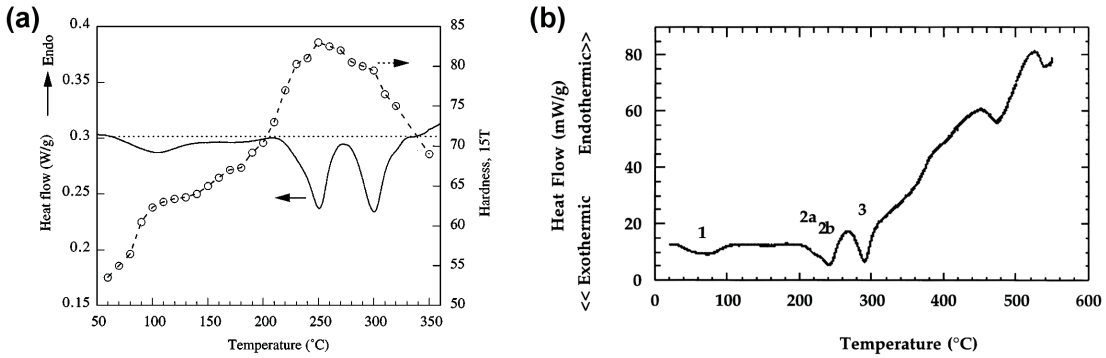

Figure 2.2: (a) DSC curve including a corresponding hardness chart of an as-quenched alloy AA6111 (heating rate 20 °C/min) [9], (b) DSC curve for alloy AA6061 (heating rate 5 °C/min) [10]

In 1998 Edwards et al. [10] tried to describe the precipitation sequence of AA6061 starting from a supersaturated solution (α_{SSS}) as detailed as possible in the following way:

- → Si clusters and Mg clusters
- → Formation of Mg/Si co-clusters
- → β" (GP-II zones)
- → β (Mg_2Si)
- → Dissolution of Mg clusters
- → Precipitates of unknown structure (GP-I zones)
- → β' and B'

The initial exothermic peak, called peak 1 in figure 2.2(b), stands for the formation of either GP zones or clusters [9]. The broadness and asymmetry of this peak lets suggest the presence of two overlapping peaks, as has clearly been resolved in other literature. Edwards et al. [10] interpreted this phenomenon as the combination of a large exothermic peak, due to the formation of co-clusters, and an endothermic peak because of the simultaneous dissolution of Mg clusters. This interpretation is contradicted by a recent study to this precipitation stage which is discussed in more detail in a later section. The following exothermic peaks are characterized by precipitates

of unknown structure (peak 2a), the formation of β'' (peak 2b) and β' with B' (peak 3) [10]. By continuing aging the equilibrium phase β would form.

The aim of the following points is to give an overview about the individual precipitation stages including descriptions of the precipitates formed as far as known today. It is also important to remember that the following characterizations of the individual precipitates refer to continuous heating of the as-quenched stage without NPA.

2.1.2.1 Clusters

As the cluster formation process will be one key topic of this work, the current status of research is going to be reviewed in more detail after the following basic informations:

Clusters are often precursory structures of GP zones but as there are several types of clusters this cannot be generalized. They are fully coherent with the matrix and their composition differs from GP zones. Normally the shape is irregular or spherical with a size of up to 2 nm [7]. In general clusters are a local accumulation of alloying elements or complexes of alloying elements and vacancies with unknown structure and order. Co-clusters probably still contain Al atoms and have low coherence strains [2]. In Al-Mg-Si alloys these clusters do not produce any contrast even in high resolution transmission electron microscopy (HRTEM) for reasons which have already been discussed in section 1 [10,11].

Clusters form for example at ambient temperatures till 50 °C [12] after quenching and before AA. In alloys containing more than 1 % Mg_2Si the presence of these clusters may alter the dispersion of precipitates that form on subsequent aging. [8]

Generally it is believed that both the Mg- and Si-clusters formed immediately after quenching and did not contribute to the first exothermic DSC peak [10]. A more detailed study of this phenomenon by Chang and Banhart [5], see figure 2.3, decomposed this peak in three overlapping cluster peaks through starting the DSC measurement already at -50 °C instead of usually above RT. Like that reactions occurring close to RT are detected as well.

In the course of the study by Edwards et al. [10] specimens that had been given the same heat treatment as in the DSC experiments were analyzed by atom probe field ion microscopy (APFIM). The resultant concentration profiles representing peak 1 showed three types of precipitates: clusters of Si atoms; clusters of Mg atoms; and Mg-Si co-clusters. Quenching and isothermally aging the alloy at 70 °C instead, indicated an evolving precipitation process. At 0.5 h, see figure 2.4(a), there seems to be no clear evidence of a co-segregation of Mg and Si. Later, at longer aging times at 70 °C, in this case 8 h and 60 h, clusters containing both Mg and Si are clearly identifiable, figure 2.4(b). The Mg:Si ratio in the co-clusters investigated

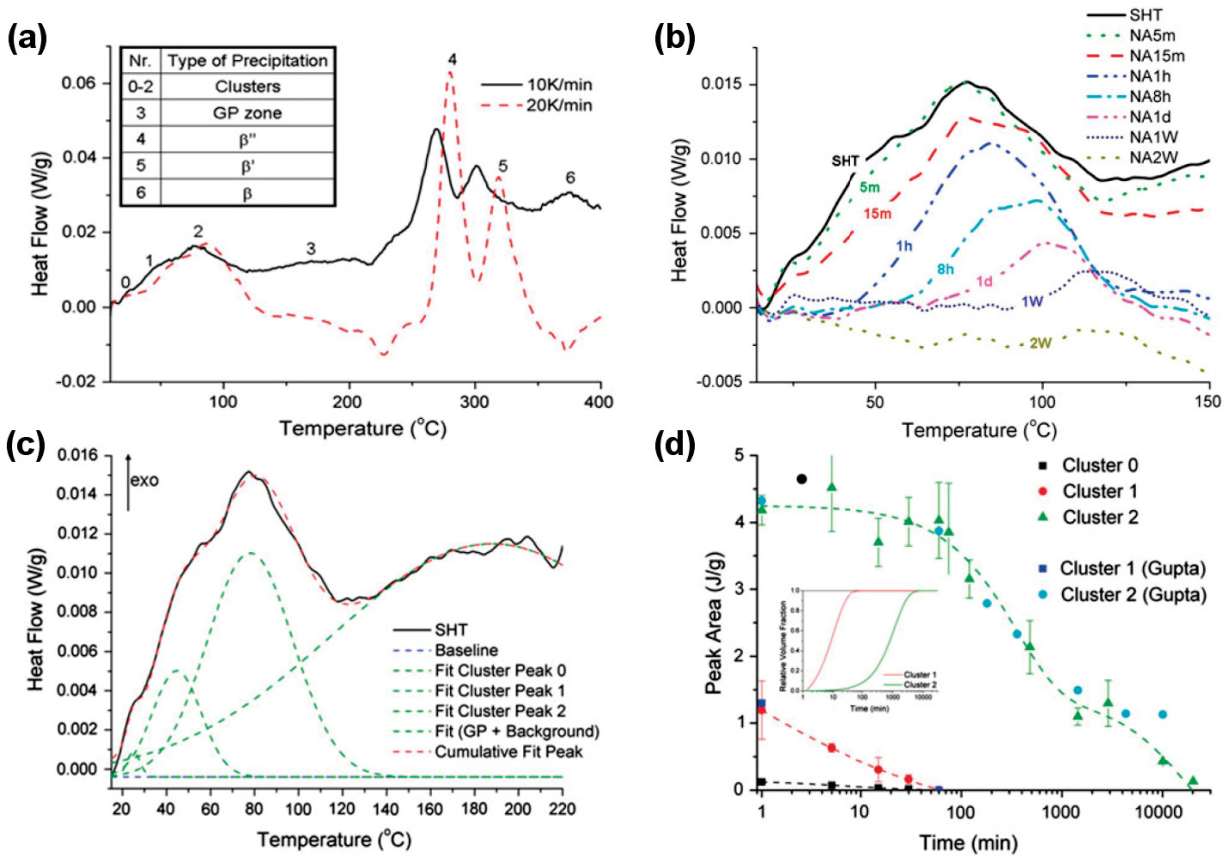

Figure 2.3: (a) DSC curve of the alloy Al-0.59 wt.%Mg-0.82 wt.%Si started at -50 °C with heating rates 10 °C/min (full curve) and 20 °C/min (broken curve), (b) only clustering stages part of previously naturally aged samples (c) calculated peak areas for various cluster types (d) peak area change of clusters with NA time, inset: relative volume fractions of clusters C1 and C2 depending on NA time [5]

increased from about 0.7 at 8 h to approximately 1 at 60 h. Edwards proposed the reason for this increase to be due to the possible dissolution of clusters of Mg atoms which results in Mg being free to combine with the clusters of Si atoms to form co-clusters [10].

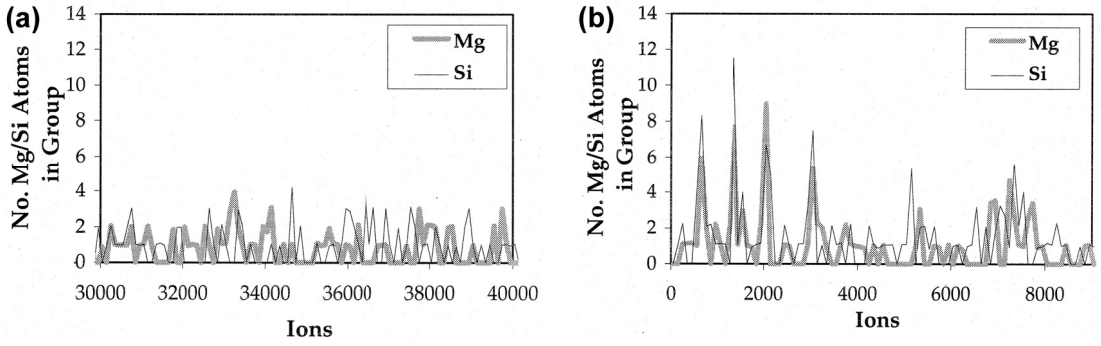

Figure 2.4: APFIM profiles of isothermally at 70 °C aged specimens showing (a) no clear Mg-Si co-segregation after 0.5 h while (b) after 8 h Mg-Si co-clusters are clearly identifiable [10]

The endothermic Mg cluster dissolution is believed to be unlikely by Chang and Banhart [5], see figure 2.3. Figure 2.3(b) shows the clustering stages part of the heat flow curves of previously

naturally aged samples. Calculations of the area of the individual cluster peaks like in figure 2.3(c) leads to figure 2.3(d). The peak areas represent the specific heat released during the individual clustering processes and correspond to the volume fractions of the precipitates. In anticipation of the vacancy topic closely dealt with later in this work, the following scenario is interpreted by the authors: At high temperatures during solutionizing the binding energy E_B of vacancies with either Mg or Si is in the range of the thermal energy, so no solute-vacancy binding occurs. During quenching from 540 to 0 °C most of the thermal vacancies come into contact with solute atoms as they pass the lattice positions on their random walk during which they eventually can be trapped and form solute/vacancy complexes. This happens as long as the binding energy is larger than the RT thermal energy; alternatively they annihilate and shortly after quenching, no more free vacancies exist. Afterward formation of clusters C0 and C1 as detected during the DSC of figure 2.3 should start from an initial state of vacancy-solute pairs. These are clusters containing more than two solute atoms. The clusters of the C1 peak are assumed to be open Si-rich agglomerates from which the vacancies detach easily. This is essential as each vacancy has to transport many solute atoms at a concentration of about $1/100$ of the solute concentration. Formation of C1 is finished after 1 hour of NA corresponding with a slowdown in the resistivity increase measured by [13] further changes of the rate of hardening and the average positron lifetime occur [1]. After about 1 hour of NA C2 starts forming (figure 2.3(d)), suggesting that C2 either forms after C1 or transformed from C1. Measurement results more point into the direction of the second assumption, so that for C2, forming at a much slower rate than C1, Mg enrichment was proposed as the key feature in this clustering stage. After prolonged aging times the size and composition of C2 doesn't change anymore. This examined C2 was found to be unnable to serve as a nucleus for precipitate growth during AA [14]. Further it is notable that the agreement of results obtained by various authors using different Al-Mg-Si alloys like shown in figure 2.3(d) is that well. According to Chang and Banhart this could indicate that clustering is saturated above a certain (unknown) amount of solute [5].

In general the composition of clusters depends on the alloy composition. Murayama et al. [11] studied two alloys using 3DAP measurements, on the one hand Al-0.65Mg-0.70Si (Si-excess) and on the other hand Al-0.70Mg-0.33Si (balanced). For the Si-excess alloy they concluded that the Mg:Si ratio in co-clusters is close to 1:1. The ratio for the balanced alloy is not given for the co-clusters.

2.1.2.2 GP-I zones

Independently of the Al alloy system GP zones are defined as follows: GP zones are subsequent structures of clusters, unlike clusters they possess an inner structure of atomic order [2]. GP

zones are, like clusters, fully coherent with the matrix and their compositions are determined by the metastable miscibility gap [7]. The shape of the zones depends on the lattice parameter difference to the matrix. At low difference zones are spherical (e.g. Al-Zn and Al-Zn-Mg alloys), at higher differences lower coherence strains are aspired and GP zone shapes are needles, rods (Al-Cu-Mg) or disklike. Furthermore, sizes are larger than approximately 2 nm and special orientations to the lattice of the matrix are present [2,7]. Formation of GP zones is associated with diffusion of atoms over relatively short distances assisted by vacant lattice sites that are preserved on quenching. The rate of nucleation and the actual structure can be greatly influenced by the presence of these excess vacant lattice sites [8].

GP-I zones are often only called GP zones in literature [8,10,11] while the term GP zones can also refer to both GP-I zones and GP-II zones [2] or the term means general precipitates defined just earlier. In Al-Mg-Si alloys the term "GP-I zones" therefore seems controversial because they seem spherical, but in reality their structure is not fully defined yet [8,10].

At the DSC peak 2a in figure 2.2(b) Edwards et al. [10] found fine precipitates imaged by strain field contrast. These don't show any clear structure and the same precipitates obtained by aging 10 min at 175 ℃ exhibit a Mg:Si ratio close to one. They believe them to probably be GP(-I) zones.

The study of Murayama et al. [11] yielded 3DAP results of ∼12 % Mg and ∼12 % Si for GP zones in a Si-excess alloy. So they concluded here as well that the Mg:Si ratio in these precipitates is close to 1:1. In contrast they found that GP zones in the balanced alloy contain 14 at.% Mg and 7 at.% Si. This is closer to the atomic ratio expected from the equilibrium phase β, Mg_2Si.

Generally GP-I zones gradually develop out of growing co-clusters in the upper temperature range of NA at about 70 ℃ [2]. They can be resolved in HRTEM [2,11]. This transition causes an exothermic heat release and has to involve some kind of ordering plus possibly the release of Al atoms and/or vacancies from the co-clusters [10].

2.1.2.3 β" Precipitate

The needle shaped β" precipitate was recently found to be coherent along the needle axis but semi-coherent at the needle tip. Therefore it is not really considered as a GP-zone anymore but as another phase in the precipition sequence, although it has been termed GP-II zone in the past. β" can be observed at peak 2b in figure 2.2 at ∼250 ℃ and is already present after 0.5 h at 175 ℃ (size ∼7 nm long). By continuing aging at this temperature the precipitates grow and get predominant at 4 h (length ∼10–15 nm) [10]. As this coincides with peak hardness, see

figure 2.2(a), β" is considered to be responsible for the maximum age-hardening effect. The structure is found to be base-centered monoclinic with a=1.534 nm, b=0.405 nm, c=0.683 nm and β=106 °. The orientation relationship with the Al lattice is: $(001)_{Al}//(010)_{\beta''}$, $[310]_{Al}//[001]_{\beta''}$ [8,10].

3DAP results for a Si-excess alloy studied by Murayama et al. [11] showed ∼23 % Mg and ∼21 % Si for β". A Mg:Si ratio close to 1:1 was concluded. As can be compared to the findings for GP zones discussed earlier, β" in the balanced alloy contains ∼17 % Mg and ∼10 % Si which is also near the atomic ratio of Mg_2Si (β). Edwards et al. [10] similarly found a Mg:Si ratio close to 1:1, though the alloy here – AA6061 – belongs to another group (balanced amounts of Mg and Si with the sum of over 1.4, see section 2.1.1).

One possible composition of β" is Mg_5Si_6, but others are also found in literature. Another finding is that Al is also included in the β" phase [15,16]. But generally the composition seems to depend on the studied alloy [17,18].

Moreover the absence of an endothermic reaction suggests that GP-I zones directly transform to β" without dissolution [8,10]. Co-clusters on the other hand are generally believed to be too small to act as nucleation sites for β" [11].

2.1.2.4 β' and B' Precipitates

These two precipitates occur at peak 3 in figure 2.2 and are associated with overaged microstructures in which hardness already decreases. According to Vissers et al. [19] the rod-shaped β' phase has a hexagonal unit cell, with a=0.715 nm and c=1.215 nm. They found though that three possible arrangements of Si atoms along the c-axis are possible. One arrangement leads to a so-called "tripling" in which a (partial) ordering of Si atoms leads to additional reflections in TEM diffraction data. In the other two arrangements Si atoms are randomly distributed, so c_a=c/3=0.405. These semi-coherent rods are orientated along $\langle 100 \rangle_{Al}$ [8] and their coherency relation with the Al matrix is: $(001)_{Al}//(001)_{\beta'}$, $[-310]_{Al}//[100]_{\beta'}$ [19]. Maruyama et al. [20] found the Mg:Si ratio to be 1.75 for balanced and 1.21 for Si-excess alloys. But these not uniform Mg:Si ratio findings can also be caused by other phases which may exist besides β': the hexagonal B', and others called e.g. U1 and U2, one orthorhombic and the other hexagonal, L etcetera [8,19]. The lath shaped B' is favored by high Si:Mg ratios of the alloy with its own Mg:Si ratio measured as 1.15 [8,10]. Moreover, similar to β', B' possesses a=0.705 nm and c=0.405 nm [8] and has been found by Edwards et al. [10] in AA6061.

2.1.2.5 β Precipitate

The equilibrium phase β is the final stable precipitate in Al-Mg-Si alloys. Formation of such a final equilibrium precipitate involves the complete loss of coherency with the parent lattice. It forms during aging at high temperatures for very long times and is associated with overaged microstructures due to its coarse dispersion and resulting little hardening [8].

The platelet shaped precipitate lies in $\langle 100 \rangle_{Al}$ planes with the plates several micrometers in size. Its structure has been characterized to be the face centered cubic (FCC) anti-fluorite structure CaF_2 with a=0.639 nm. The strength contribution of this precipitate in Al-Mg-Si alloys is low [10,19]. β may transform directly from β' and has the following orientation relationship with the Al lattice: $(100)_{\beta}//(100)_{Al}$, $[110]_{\beta}//[100]_{Al}$ [8]. According to the chemical formula Mg_2Si the Mg:Si ratio equals 2.

2.1.3 Solubility of Metastable Phases

As already discussed in the introduction of this section the GP zones solvus defines the upper temperature limit of stability of the GP zones for different compositions. Note that the term "GP zones" here refers to various precipitates called like that in different Al-alloy systems. The GP zones solvus may be shown as a metastable line in an equilibrium diagram. Its exact location can vary dependent on the concentration of excess vacancies. Solvus lines are also determinable for other metastable precipitates. For the Al-Mg-Si system these are shown in figure 2.5(b). Their pseudo-binary phase diagram, Al-Mg_2Si, is shown in figure 2.5(a). In general the full sequence of GP zones and intermediate precipitates is only possible when the aging temperature of the alloy is below the GP zones solvus [21]. Alloys in which the quench-bath and aging temperatures are both below the GP zones solvus are e.g. some Al-Mg-Si alloys [8].

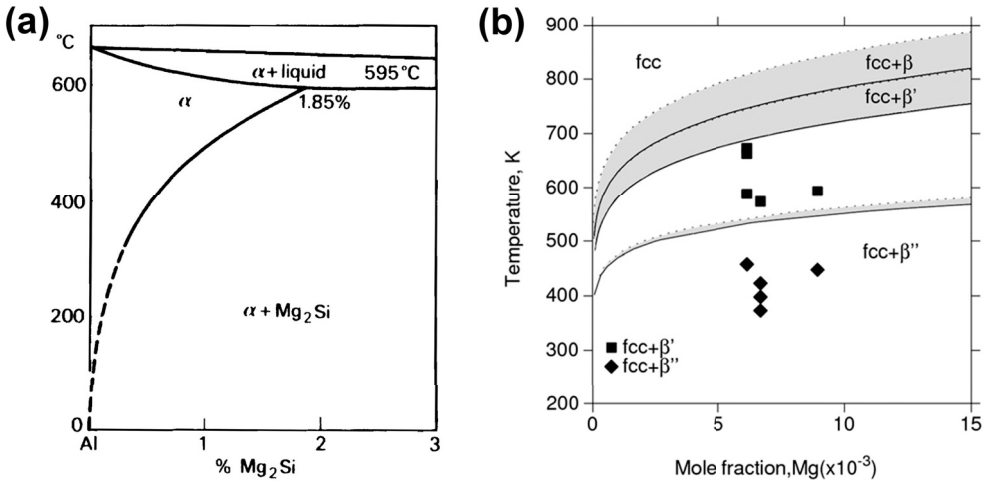

Figure 2.5: (a) Al-Mg_2Si pseudo-binary phase diagram [8] (b) Calculated solvus boundaries in an Al-Mg-Si system containing 0.76 at.% Si; the width of the bands signifies the uncertainty in the solvus [22]

2.1.4 Influence of Natural Pre-Aging on Artificial Aging

Figure 2.6 gives an overview about the influence of NPA on the precipitation kinetics during AA at 160 ℃ for an Al-Mg-Si alloy showing the negative effect of NPA on AA. The figure also plots a hardness curve for NA prior to AA [23]. The general hardness increase of Al-Mg-Si alloys during NA after a solution heat treatment and quenching starts after relatively short times of about 30 minutes followed by a quick rise within one day. Afterward the slope starts decreasing until after 3 days just a weak increase remains. This so-called NA may continue almost indefinitely as it can still be measured after months and years [2].

As can be seen from figure 2.6, after longer NA times AA starts at higher hardness values, but the increase starts after much longer times compared with the curve for AA without NPA. After more than 30 min of NPA the hardness maximum achieved without NPA can't be reached anymore. As a consequence the strength difference between same AA times with and without NPA can be significant [23].

Typically alloys showing the negative effect of NPA on AA contain 0.5 to 1 wt.% of both Mg and Si. Comparing the DSC results for the cluster formation process as described in section 2.1.2.1 with the AA kinetics following NA, Chang and Banhart [5] concluded that already about 60 to 80 % of C1 formation is enough to fully establish the negative effect. More precisely this means that for their alloy, Al-0.59 wt.%Mg-0.82 wt.%Si, the negative effect on AA is being settled after only 10 to 18 minutes of NA, this is shown in the inset of figure 2.3(d). Further, with increasing NA time, the aging response will be similar even for complete C1 formation or existing C2 [5]. It should be noted though that for industrial alloys also containing several other alloying elements or impurities, the negative effect settles after longer NA durations.

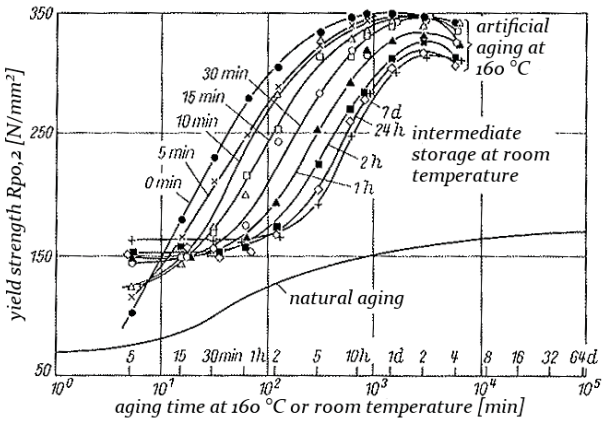

Figure 2.6: Hardness evolution of the alloy AA6082 showing the negative effect of NA on AA [23]

2.1.4.1 Theories Concerning the Negative Effect in Al-Mg-Si Alloys

As already mentioned in section 1 there are some possible reasons for this adverse effect. One point is the after NA low residual supersaturation of alloying elements and vacancies. Another point is the time-dependent reversion of subcritical, at AA temperature unstable clusters. These clusters cannot act as nuclei for the afterward formed peak hardening phase β" . So the reversion is necessary and like that responsible for the retardation of the precipitation of β" as well as for a coarser distribution of precipitate nuclei. At the same time the critical nuclei size rises because of the lower supersaturation [2,11].

Now these reasons will be discussed in the light of a recent study made for the alloy used in this work including the proposed theory of what may really be responsible for the negative effect. Pogatscher et al. [24] for the first time reported the influence of NPA on AA at high temperatures. In their opinion the mechanisms responsible for the effect of NA suggested by other researchers could not explain the different temperature dependencies revealed for various thermal treatments.

As can be seen from figure 2.7 three different heat treatment procedures were compared. Abbreviation 'A' stands for direct aging. At 'B1' and 'B2' quenching was done in water at RT, followed by RT storage for 1.2 x 10^2 s (B1) and 1.2 x 10^6 s (about 2 weeks) (B2) [24].

In principle, figure 2.7(a) follows the above discussed hardness scheme. B2 starts at the value reached after long-term NA (73 HBW). Interestingly A and B1 show the same hardness curves. Figure 2.7(b) exhibits again same curves for A and B1 but with lower peak hardness and already revealing the start of over-aging. B2 in contrast already exhibits a significant reversion followed by a slope of the hardness curve and peak hardness similar to A and B1. At 250 °C, see figure 2.7(c), all relationships between the procedures changed compared to lower temperatures. Heat treatment A now produced the slowest aging kinetics and lowest peak hardness. B1 shows

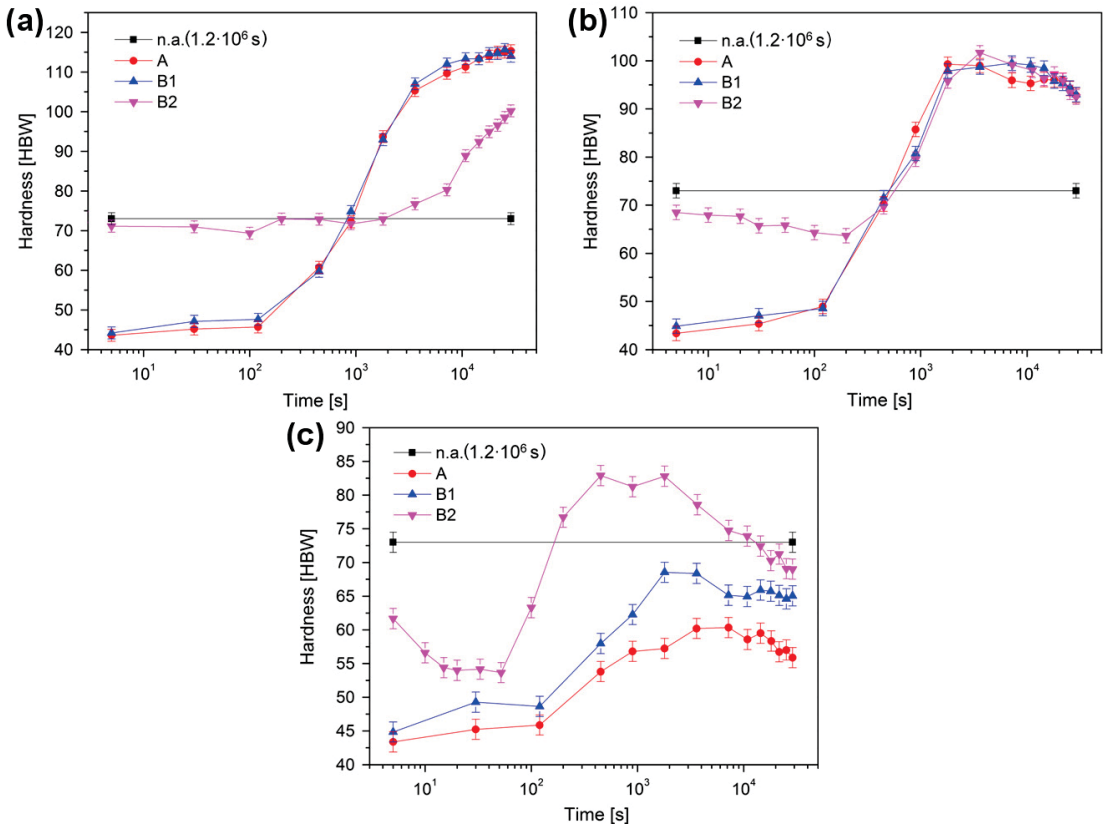

Figure 2.7: Hardness curves for three different AA procedures A, B1 and B2 at (a) 170 °C, (b) 210 °C and (c) 250 °C [24]

slightly higher hardnesses. In contrast the highest hardness and fastest aging kinetics were found for B2, the long-term NPA samples, after an even more distinct reversion [24].

Further investigations and calculations of this phenomena resulted in the following discussion: In general diffusion processes affect nucleation and growth of precipitates besides the solute supersaturation. The metastable solvus line for the same precipitate should be constant for various heat treatment procedures. Note that metastable solvus lines will be treated later in section 2.1.3. Hence Pogatscher et al. concluded that the kinetics of B2 must be controlled by another thermally activated mechanism, which is supposed to depend on the faster dissolution of co-clusters at higher AA temperatures. After this reversion the kinetics of B2 gets uncharacteristically faster the higher the AA temperature. Resistivity measurements also confirmed that co-clusters are faster dissolving at higher AA temperatures due to a continued isochronal resistivity decrease after 30 min (1.8 ks) of AA. These measurements let deduce that under those conditions co-clusters are still predominant below 180 °C of AA, when the hardness curve still follows figure 2.7(a) [24].

The resulting theory describing these phenomena is based on a model of Zurob and Seyedrezai [13,25] which says that at the end of NA all quenched-in vacancies are bound in clusters.

By the way this model will be treated in more detail in section 2.4.2.2. Pogatscher et al. assumed that vacancy-solute clustering during NA can temporarily stabilize vacancies at high AA temperatures, co-clusters are therefore associated to be "vacancy prisons". In this way vacancies could not assist diffusion at temperatures usually used for AA of B2. The faster dissolution of co-clusters at higher AA temperatures activates the vacancies by a thermally activated release. Consequently, the at the beginning of AA low initial quenched-in vacancy concentration rises and further diffusion controlled precipitate nucleation and growth can be influenced [24].

As a purpose of this work it is thought that interactions between MA elements and vacancies might change the precipitation process of Al-Mg-Si alloys showing the negative effect of NA on AA in such way, that instead or in addition of Mg-Si co-clusters also other thermally less stable vacancy-solute clusters could form. During subsequent AA these new clusters might dissolute faster, also already at lower AA temperatures and like this enhance the precipitation kinetics of NPA samples during AA. Summing up it is believed that a suppression of the co-cluster formation during NA by MA elements could affect the influence of NPA on AA.

2.2 Vacancies

Lattice vacancies are zero-dimensional defects or point defects which signify atoms missing at regular lattice sites [2,26]. The formation of these thermal vacancies in an equilibrium concentration represents a gain in free energy for the crystal although an energy of formation E_{VF} must be spend per vacancy [26]. Due to numerous possible ways of distributing vacancies over the lattice sites the entropy of a defect-containing crystal is larger than that of a perfect crystal [26,27].

2.2.1 Types of Vacancies

Besides monovacancies, divacancies are also present in equilibrium. Because the formation of a divacancy saves two 'broken bonds' less energy (E_{DF}) is required than for the formation of two single vacancies E_{VF} with $E_{DF} = 2E_{VF} - E_{DA}$. In pure Al, E_{VF} is about 0.65 eV (or 62.7 kJ/mol), the energy of divacancy association (E_{DA}) is 0.25 eV, so E_{DF} equals 1.05 eV [26, 28]. In general the formation of vacancies in closed-packed metals requires the smallest amount of energy in comparison to other lattice defects. Multiple vacancies like triple or quadruple vacancies etcetera are practically never present in equilibrium [26,27].

2.2.2 Vacancy Concentration: Equilibrium and Non-Equilibrium Conditions

The following simplified equivalent formulas, equation 2.1 [26] and 2.2 [21], which are normally given in literature to describe the equilibrium concentration of vacancies $c_V(T)$, ignores vacancy-vacancy interactions because their equilibrium concentration is assumed to be small. Further it sets the increase in enthalpy of the solid (ΔH) directly proportional to the number of vacancies added, i.e. $\Delta H \simeq \Delta H_V X_V$. X_V means the mole fraction of vacancies and ΔH_V signifies the increase in enthalpy per mole of vacancies added. More precisely each vacancy causes an increase of $\Delta H_{VF} = \Delta H_V / N_A$, with N_A being Avogadro's number. [21]

$$c_V(T) = \exp\left(\frac{S_{VF}}{k}\right) \cdot \exp\left(\frac{-E_{VF}}{kT}\right) \tag{2.1}$$

$$c_V(T) = \exp\left(\frac{\Delta S_V}{R}\right) \cdot \exp\left(\frac{-\Delta H_V}{RT}\right) \tag{2.2}$$

To understand these formulas, some background information may be provided now. The formation of vacancies is associated with the change in Helmholtz free energy F_{VF} given by $F_{VF} = E_{VF} - TS_{VF}$. The terms signify the energy (E_{VF}) and entropy (S_{VF}) of formation. The formation process itself is conceived as the removal of an atom from the interior to the surface [29]. S_{VF} can now also be called the entropy of vacancy formation [26] while ΔS_V signifies the thermal entropy per mole of vacancies added [21], see next paragraph. E_{VF} means the energy of vacancy formation while ΔH_V was already defined above. Instead of the terms of equation 2.1 you can also write entropy (ΔS_{VF}) and enthalpy (ΔH_{VF}) of formation; note that all terms used in equation 2.1 refer to a single vacancy [27].

In general there are two contributions to the total entropy change ΔS on adding vacancies. On the one hand there is a small change in the thermal or vibrational entropy part ($S_{VF_{vib}}$ in equation 2.1 or $\Delta S_{V_{vib}}$ in equation 2.2) [21,29]. This entropy is called like that because the vacancy formation changes the lattice vibrations in its vicinity, which means atoms close to the vacancy have a different vibrational frequency from those far from it [26,29]. The reason is a relaxation of neighboring atoms into the vacancy. This reduces the vacancy volume and loosens the binding between the nearer neighboring atoms [30]. The largest contribution is, though, due to the increase in configurational entropy ($S_{VF_{cfg}}$ or $\Delta S_{V_{cfg}}$) [21]. This part is usually thought to be an ideal mixing entropy, at least for pure metals; it is more complicated for alloys. Note that during the derivation of equations 2.1 and 2.2 the configurational part disappears and only the vibrational part stays in the equation. For low pressures the energy of formation E_{VF} can

also be assumed to be approximated by the enthalpy of formation ΔH_{VF} (though not always safely) [29]. This assumption is based on the fact, that for isobar processes an enthalpy ΔH and an internal energy ΔE only differ in a product out of the pressure p and the volume change ΔV with: $\Delta H = \Delta E + p\Delta V$. If during a chemical reaction the volume change from a reactant to the product is negligible, like at reactions which only comprise solids and fluids, it follows for not too high pressures: $\Delta H \simeq \Delta E$. Further due to $dH = dQ + V dp$, at constant pressure, the change in enthalpy dH equals the absorbed or emitted thermal energy of the system dQ. As a consequence E_{VF} can be seen as the energy needed to create a vacancy which was provided by dQ.

The first term on the right hand side of both equations (2.1, 2.2) is in general a constant of ∼3, independent of T and usually ignored [29], whereas the second term increases rapidly with rising T. In practice c_V reaches a value of about 10^{-4} to 10^{-3} at the melting point of solid metals, which is 660.32 °C for pure Al [21]. In pure Al c_V drops about 8 orders of magnitude with declining temperature [2], more exactly from $3.5{\cdot}10^{-4}$ at 570 °C to $7.4{\cdot}10^{-12}$ at 25 °C. There are four orders of magnitude difference between RT and AA temperatures while the difference within the AA temperature range from 150 to 250 °C varies ∼1.5 orders of magnitude. These values are gained by inserting 0.702 eV for E_{VF} in pure Al [31] and 1.69·k for S_{VF} in pure Al [31] in equation 2.1. In pure materials this temperature dependence of c_V usually follows an Arrhenius relationship of $\log c_V$ plotted against *1/T* [32], see figure 2.8(a).

Conventionally vacancy concentrations in metals are measured by quenching, dilatometry or (differential) thermal expansion, and positron annihilation [26,29].

Two of these methods were used to obtain the Arrhenius plots of figure 2.8(a), i.e. thermal expansion (dashed line) and positron annihilation (full line). The comparison shows an increasing deviation at higher temperatures. This is because positron annihilation, which is most sensitive in the medium temperature range ($T \sim 0.6T_m$), is unaffected by divacancies while thermal expansion, which measures at high temperatures, is not. Therefore from the difference in curvature the divacancy concentration c_D near the melting point can be derived as $c_D(T_m)/c_V(T_m) \sim 0.28$ with decreasing c_D/c_V for decreasing temperatures where c_D gets $\ll c_V$ [26]. Calculation of c_D are handled in a similar way as equations 2.1 and 2.2 [27,29,30].

2.2.2.1 Change of the Vacancy Concentration Due to Quenching

During quenching a metal from a high temperature, excess vacancies are retained. With time those quenched-in vacancies in excess of the equilibrium concentration might anneal out [21]. The tendency to lower the total free energy of a system drives the vacancies to move to sinks, which are in general jogs at dislocations, incoherent interfaces, grain boundaries or free surfaces,

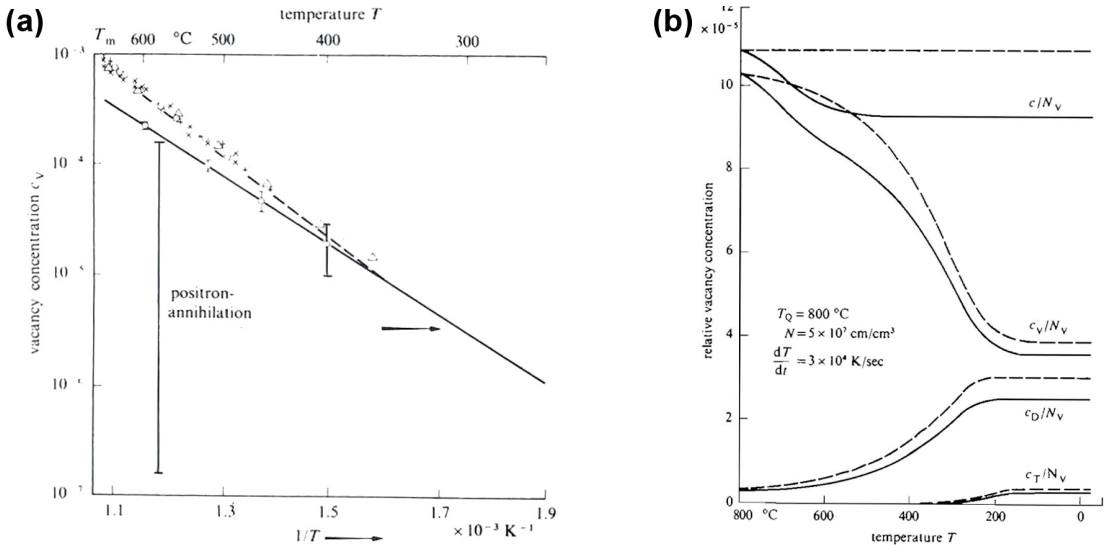

Figure 2.8: (a) Temperature-dependence of c_V in Al [26,28], (b) Calculated changes of single (c_V), double (c_D) and triple (c_T) vacancy concentrations during quenching Au from 800 ℃ [26]

where the vacancies are annihilated [33]. Additionally there will be a tendency of vacancies to form "vacancy clusters", which can collapse to dislocation loops [21].

At low quenching temperatures T_Q a certain electrical resistance ρ_{el} is measured, but at higher T_Q the electrical resistance rises with increasing T_Q. The additional electrical resistance $\Delta\rho_{el}$ which is measured after the quench from these higher T_Q, e.g. for gold, indicates a contribution of divacancies. These divacancies are present at T_Q or form from single vacancies during the quench, even at quenching rates of several $10^4\ K/s$. The result is a strongly decreasing ratio c_V/c_D during the quench which is shown in figure 2.8(b). [26]

Divacancies can also be produced on annealing. In the FCC lattice, these can migrate faster than single vacancies. Furthermore during the recovery process vacancies can associate with solute atoms to form complexes of characteristic mobility [26]. While the activation energy for Al self-diffusion is about 1.28 eV, it is ∼0.62 eV for monovacancies and between 0.35-0.40 eV for divacancies [2]. In general aggregates of vacancies such as divacancies or trivacancies can also contribute to diffusion [29].

An important effect of quenched-in vacancies is to remarkably increase the rate at which atoms can diffuse at the aging temperatures. Furthermore they can also relieve misfit strain energies. As a consequence the process of nucleation and growth can be speeded up [21]. In Al the self-diffusion at equilibrium vacancy concentrations only starts at about 160 ℃, while in presence of excess vacancies diffusion is already observed at -50 ℃ [2].

A critical vacancy supersaturation must be exceeded to start nucleation. Therefore as close to grain boundaries quenched-in vacancies are inevitably lost due to their high diffusivity, precipitate-free zones (PFZ) are formed. In these zones the vacancy concentration will be

around the equilibrium value for the aging temperature while away from the boundary it will be much higher. At low temperatures, where the driving force for precipitation is high, the critical vacancy supersaturation needs to be lower and thus narrower PFZs are formed [21]. Another possible reason might be a reduced mobility of after quenching initially remaining vacancies at lower temperatures. Thus fewer vacancies anneal out before the precipitation starts.

2.2.2.2 Influence of Solute Atoms

In solid solutions, the equilibrium c_V at a certain temperature depends on the nature of the interaction between vacancies and solute atoms and complexes. Picu et at. [32] and others [29] describe the "complex model" originally proposed by Dorn and Mitchell (1966, [34]) and further developed by Faupel and Hehenkamp (1986 [35], 1987 [36]). The "complex model" can be seen as a transition between the model discribed later in section 2.3.2.1 for 1-2 % solute concentration and the concentrated alloy models. It is the basis for the description of the diffusion behavior of alloys with elevated solute concentrations (up to 5 at.%) as also discussed later in section 2.3.3.3. The "complex model" assumes that if impurities (B) have a positive excess charge vacancy-impurity complexes of one vacancy and i impurity atoms are probable to form [29]. Equation 2.3 decribes the fraction of sites occupied by vacancies in a solid solution of B atoms in a matrix A lattice [32]. As this equation is only valid for binary systems, no direct calculations can be derived for Al-Mg-Si alloys. Nevertheless it clearly demonstrates the effect solute atoms have on c_V and diffusion.

$$\begin{aligned} c_V &= \sum_{i=1}^{z} \exp\left(-\frac{F_{VF_i}}{kT}\right) = \sum_{i=1}^{z} \exp\left(-\frac{E_{VF_i} - TS_{VF_{cfg}} - TS_{VF_{vib}}}{kT}\right) \\ &= \sum_{i=1}^{z} \begin{pmatrix} z \\ i \end{pmatrix} c_A^{z-i} c_B^i \exp\left(-\frac{E_{VF_i}}{kT}\right) \end{aligned} \tag{2.3}$$

So c_V is the sum of all complexes containing one vacancy coordinated with i solute B atoms and $z-i$ A atoms. F_{VF_i} means the free energy of the vacancy formation in a complex of type i. As the configurational entropy $S_{VF_{cfg}}$ and the thermal entropy $S_{VF_{vib}}$ can be neglected, only the associated energy of formation E_{VF_i} depending on the number of coordinated i B atoms remains in the equation [32].

The problem of this original derivation is that the vacancy formation energy is assumed to only depend upon the number of solute atoms in the first nearest neighbor position and not on the precise configuration or on solutes located at larger distances from the vacancy. Recently Picu et

at. [32] reasoned that these original assumptions of the model are e.g. not strictly valid for the binary Al-Mg alloy based on following arguments: An independence on the configuration would imply that higher order solute-solute energetic interactions are neglected. The neglect of the interaction with a solute located at larger distances would be only possible if the solute size effect (elastic) is much larger than the electronic component of the vacancy formation energy [32]. These effects will be treated in more detail in section 2.3.3. Therefore Bérces and Kovács (1983, [37]) modified Dorn and Mitchell's formula to take possible configurations into account. Faupel and Hehenkamp introduced "average" effective jump frequencies per matrix A atom $\langle\omega^A_{eff}\rangle_i$ and per solute B atom $\langle\omega^B_{eff}\rangle_i$ in the ith complex. The term ω is called the defect jump frequency of a vacancy for low defect concentrations or also "exchange" frequency, as it denotes the exchange between a vacant site and a neighboring atom. $\langle\omega^B_{eff}\rangle_i$ now especially includes correlation effects [29] which treat the possibility that an atom that has just exchanged places with a vacancy might jump back. Note that correlation effects and jump frequencies will be treated more closely in sections 2.3.1 and 2.3.2. A result of these calculations and corresponding measurements is the existence of a nonlinear increase in the vacancy concentration on alloying, which nonlinearly varies the solute diffusivity [32] and enhances the self-diffusion on alloying. These effects were found in binary FCC systems (AgSb, AgSn) containing impurities with an excess positive charge [29].

Picu et al. [32] observed that in equilibrium Al-Mg alloys containing 5 % Mg, solute clusters may stabilize a higher vacancy concentration than the surrounding area because in the presence of solute clusters, the locally developed compressive strain due to the size misfit of Al and Mg atoms leads to a drastic increase in the vacancy concentration within such clusters. The mean vacancy concentration depends therefore on the solute-vacancy binding energy, the solute distribution and the mean solute concentration. The last point was shown to have a weak influence in Al-Mg [32]. Binder [38] also states that the vacancy concentration in equilibrium may be diverse in A-rich and B-rich domains.

In a quenched Al-Mg alloy the annealing out of excess vacancies is hampered already at very low solute contents. Especially effective is Mg due to it's large atomic radii difference to Al ($r_{Mg}/r_{Al} = 1.12$ [39], see section 2.4.1). Panseri et al. (1958, [40]) concluded that already at 0.2 wt.% Mg the annealing process of quenched-in vacancies at RT is nearly suppressed because of Mg-vacancy complexes with a high binding energy. These Mg-vacancy complexes are relatively stable and would only dissolve at temperatures above 100 °C [2] which is consistent with the above mentioned influence of solute atoms on the vacancy concentration.

2.3 Interactions of Vacancies with their Environment

2.3.1 Vacancy Controlled Diffusion – Vacancy Mechanism

The vacancy mechanism is the most important diffusion mechanism and the preferred mechanism for metals and alloys for both matrix and substitutional solutes [29]. It is predominant for lattice atoms in close-packed metals [26], like Al which is FCC.

The thermal vibrations of an atom about its equilibrium position possess a frequency ν which can be approximated by the Debye frequency $\sim 10^{13}$/sec. They are normally not enough to transfer it to a neighboring vacant site. As illustrated in figure 2.9 for this transfer the jumping atom passes the so-called saddle point only by expenditure of (free) distortional enthalpy F_{VM}. This is provided by thermal fluctuations of the kinetic energy which was picked up near the atom's equilibrium position where the kinetic energy takes maximum values [26,27]. These fluctuations are described by the jump frequency of the vacancy ω, i.e. the number of jumps per second [29], as follows (see also section 2.2.2.2):

$$\omega = \nu \exp\left(-\frac{F_{VM}}{kT}\right) \tag{2.4}$$

with $F_{VM} = E_{VM} - TS_{VM}$. E_{VM} and S_{VM} denote the migration energy and migration entropy of the vacancy. S_{VM} stems from the change in lattice vibrations during the transfer. The activation energy for self-diffusion E_{VD} can now be defined as $E_{VD} = E_{VF} + E_{VM}$ [26]. Accordingly the activation enthalpy is defined as $H_{VD} = H_{VF} + H_M$ with H_M as the enthalpy of migration [29].

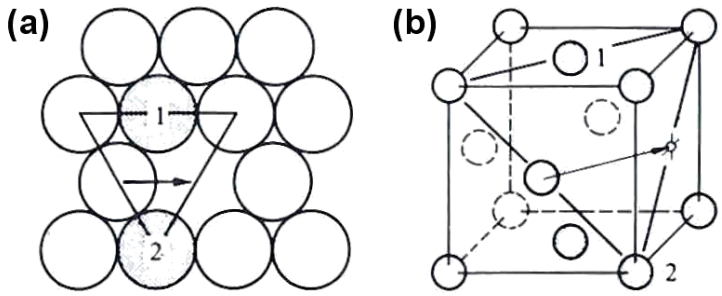

Figure 2.9: (a) Atom passing the saddle point between two atoms to reach a neighboring vacancy (b) the same as in (a) pictured in a spatial fcc lattice [26]

Vacancy migration has been treated by analytical methods (1968, [41]) as well as computer simulation (1983, [42]). The above briefly described model by Flynn yields remarkably good predictions of activation enthalpies for vacancy migration compared to experimental data for quite a number of metals [27].

ω has now to be distinguished from Γ, the actual jump frequency of an atom. First, for an atom to jump from one site to another, the necessary defect – here the vacancy – has to be available. The probability of a given atom to be next to a vacancy is nc_V where n is the coordination number, c_V as the fractional vacancy concentration is the probability of a vacancy arriving at the neighboring site. So concerning Γ the atom has to wait for a vacancy while for ω a vacancy never has to "wait" for an atom. Adding ω from equation 2.4 the equation for Γ is now [29]:

$$\Gamma = nc_V\omega \tag{2.5}$$

The diffusion coefficient of an atom for a three-dimensional random walk can now be written as [26]:

$$D = \frac{1}{6}a^2\Gamma = D_0 \exp\left(-\frac{E_{VD}}{kT}\right) \tag{2.6}$$

For an one-dimensional random Brownian motion a factor $\frac{1}{2}$ would be written, but as in three dimensions only $\frac{1}{3}$ of all jumps contribute to $\bar{x^2}$, i.e. the mean square displacement ($\bar{x^2} = 2Dt$), the numerical factor in equation 2.6 is $\frac{1}{6}$. a denotes the lattice parameter. D_0 is the so-called pre-exponential factor which also incorporates the dependency of D on the entropies S_{VM} and S_{VF}. In the case of metal alloys attractive or repulsive interactions of the solute with the vacancy are always possible. These can have a profound influence on the diffusion coefficient of the solute plus to a lesser extend the solvent by way of correlation effects [29]. This will be discussed in much more detail in the following sections.

2.3.2 Correlation Effects

Correlation effects are easier explained with first describing the isotope correlation factor before specifying the situation with regard to solute-vacancy correlations.

In general an atom which possesses the for a jump required free activation enthalpy F_{VM} cannot use it unless a vacancy is nearby [30]. Further a complete random walk of the tracer atom, e.g. an isotope A* diffusing in A, would mean that each direction is unrelated to the previous one [26]. Accordingly equation 2.6 does not fulfill the requirement that after an atom jump into a vacancy the following atom transposition is possible in all jump directions which the lattice symmetry allows. So if the tracer and a vacancy have just exchanged places – e.g. between positions 6 and 7 in figure 2.10 –, the tracer is still neighboring the vacancy but placed on the opposite side. This fact gives the tracer atom a higher chance to perform a reverse jump to 6 than to further migrate along the concentration gradient [26,30].

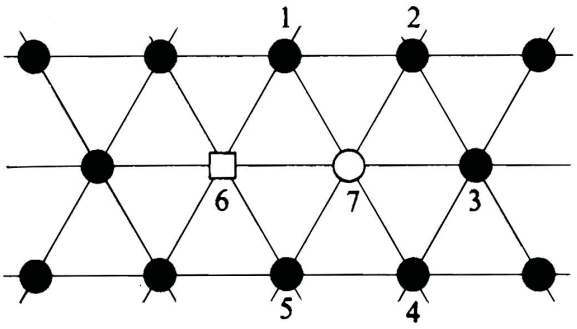

Figure 2.10: Close packed plane (111) in the fcc lattice with a vacancy (□) and an isotope (○) to estimate the correlation factor [26]

Summing up, this means that because atoms mostly require the assistance of defects (e.g. vacancies) to move around, there is commonly an unavoidable memory or correlation effect between jump directions [29]. The vacancy (which is now placed at position 7), however, has the same interaction with A* and A, so the probability of a second change between 6 and 7 is precisely $1/n$ of the vacancy jump rate ω (for n nearest neighbors) [26]. By this way the vacancy itself moves in complete random walk whereas the tracer has a reduced probability of continuing in the direction of the first jump, since it would require another vacancy to further migrate this way. Furthermore weaker correlations in the tracer jumps are possible as long the vacancy stays in the vicinity of the tracer. This is because after further jumps of the vacancy with the other neighboring atoms, it can return to its original place near the tracer which raises the reverse jump probability [29,30].

The correlation factor f can now be defined as: $f = D_{A^*}/D_A$ with D_{A^*} being the diffusion coefficient of the tracer and D_A that for self-diffusion [26]. As a consequence of a reverse jump two jumps of an atom in the x-direction have been lost. After m jumps $m \cdot 2/n$ jumps have been lost. The effective jump number results with $m \cdot (1 - 2/n)$. A more accurate calculation leads to an estimation of the tracer correlation factor f for a FCC lattice with $n = 12$ of ∼0.78 [26].

In dilute alloys the tracer can now be considered as the impurity, like a solute atom B in A. It is also necessary to consider the impurity concentration to be sufficiently dilute that there is no composition-dependent diffusion coefficient. So the impurity is thought to diffuse in pure matrix [29]. In this situation correlation becomes a crucial process since the vacancy can interact differently with B than with A. It can, for instance, be attached firmly to B, because B is an extra large atom or one with a higher valency; these interactions are more thoroughly dealt with in the following sections. As a consequence reverse jumps would be the rule and $f \ll 1$ [26]. This situation can also be described with the help of the jump frequencies of the vacancy with the impurity ω_2 and with the matrix atom ω_0, both are pictured in figure 2.12. In the present situation the impurity correlation factor f_2 in the FCC lattice is a function of ω_2/ω_0 [29].

Equation 2.7 shows the resultant dependence of the impurity diffusion coefficient D_B from f_2, now as a function of Γ_B/Γ_A [26].

$$D_B = D_A f_2 \frac{\Gamma_B}{\Gamma_A} \tag{2.7}$$

As depicted in figure 2.11 starting from the tracer correlation factor of $f = 0.78146$ with $\omega_2 = \omega_0$, which means the "impurity" is now the tracer, there are two possible following curvatures. If $\omega_2 < \omega_0$ the impurity motion becomes decorrelated, after an exchange the vacancy does not tend to remain near the impurity, reverse jumps aren't the rule anymore. With decreasing ω_2, f_2 approaches 1.0, which signifies a complete random walk. It also means that the impurity diffusion coefficient D_B can be raised. The reverse situation in which $\omega_2 > \omega_0$ the vacancy and the impurity tend to exchange places in a special configuration. Due to many effectively canceled impurity jumps f_2 approaches zero (0.0). This reduced impurity correlation factor also reduces the the impurity diffusion coefficient D_B [29].

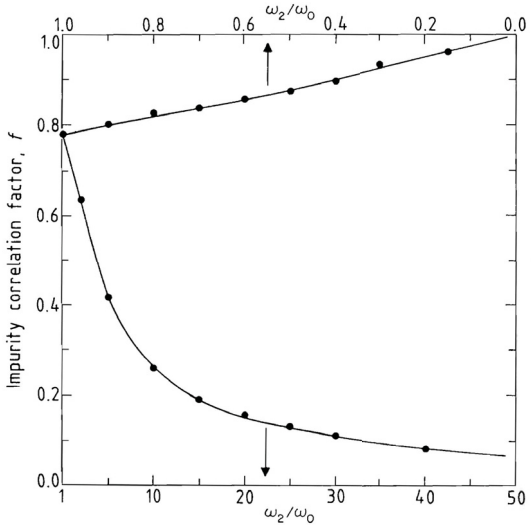

Figure 2.11: Impurity correlation factor in an fcc lattice as a function of ω_2/ω_0 [29]

Γ has already been defined in equation 2.5 as being dependent on the vacancy concentration c_V and the jump frequency of the vacancy ω. In general both factors cannot be taken as being constant which means that D_B is not only influenced by the value of f_2. As has already been treated in section 2.2.2 c_V may rise for example due to quenching or additional solute atoms, but other solute atoms can also decrease c_V (see end of section 2.3.2.1). On the other hand the term ω of Γ_B in equation 2.7 may equal the solute-vacancy exchange frequency ω_2 while Γ_A should depend on ω_0. That ω_2 strongly depends on the kind of the solute atom will be treated more closely in section 2.4.2.1 and can be seen for example from table 2.3.

Another fact is that the defect jump frequencies ω_i are temperature dependent [43]. As the

correlation factor f_2 is a function of these ω_i (also treated later together with equation 2.12) it is temperature-dependent as well. Generally, if $f_2 < f_0$, with f_0 being the correlation factor of the matrix atoms, plus if no divacancies are involved in the diffusion process, f_2 rises with temperature [30]. This should be kept in mind when calculated values of ω_i and f_2 for various alloying elements in Al (Si, Mg and Cu) are presented in section 2.4.2.1, see figure 2.15.

Summing up all these influences on D_B can lead to similar diffusion coefficients for various solute atoms although the interaction of a vacancy with the various solute atoms may be completely different. One example are the in section 2.4.2.1 mentioned diffusion coefficients of Mg D_{Mg} and Cu D_{Cu}.

As a result it can be understood why the kinetics for the combined diffusion of solute-vacancy complexes is complicated [26]. This will seem still more true when the next section, section 2.3.2.1, is read.

2.3.2.1 Five Frequency Model

Generally, the presence of the impurity atom in the matrix also influences the matrix jump frequencies near the impurity so that they differ from ω_0. For the FCC lattice the usual model to describe this phenomenon is the so-called five-frequency model which is shown in figure 2.12 [29]. This model assumes the difference between the first and second neighbor distances in the FCC lattice to be large enough to ignore solute-vacancy interactions beyond the nearest-neighbor (NN) distance of the vacancy. There are three possible dissociative jumps which separate a vacancy from a neighboring solute atom, the corresponding dissociative jump frequency is called ω_3. ω_4 signifies the frequency of the reverse jump, i.e. associative jump. ω_2 stands for the solute-vacancy exchange and ω_1 describes the vacancy jump around the solute atom, which avoids the break of the solute-vacancy complex. ω_0 denotes a jump not affected by the solute atom, the vacancy can be seen as a free one [44]. Note that figure 2.12 respectively only labels one example.

Out of the following two equations (2.8, compare to equations 2.5 and 2.6) for the self-diffusion coefficient of the pure metal D_A and the diffusion coefficient of the impurity in a pure matrix D_{B^*}, which is measured with the help of a radioactive isotope [30]:

$$D_A = \frac{n}{6}a^2 \cdot \omega_0 \exp\left(-\frac{E_{VF}^A}{kT}\right) f_0;\ D_{B^*} = \frac{n}{6}a^2 \cdot \omega_2 \exp\left(-\frac{E_{VF}^B}{kT}\right) f_B \tag{2.8}$$

the relationship of the two diffusion coefficients at indefinite dilution ($D_{A,B^*}(0)$) follows due to equation 2.9. Note that f_B in equation 2.8 is the correlation factor of atom B, it stands for the same as f_2 defined for the five frequency model; from now on only the term f_2 is used [30].:

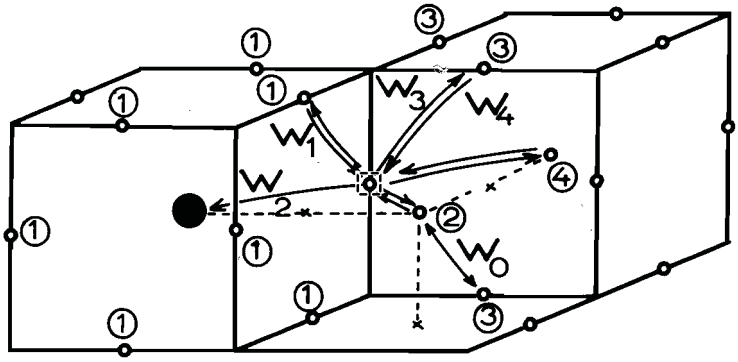

Figure 2.12: Standard five-frequency model for solute diffusion in the fcc lattice by a vacancy mechanism. After a vacancy jump a solute atom (•) may change its neighborhood from a vacancy (□) to an Al atom (○) or vice versa. [44]

$$\frac{D_{B^*}(0)}{D_A(0)} = \frac{\omega_2}{\omega_0} \exp\left(-\frac{E_{VF}^B - E_{VF}^A}{kT}\right) \frac{f_2}{f_0} \tag{2.9}$$

E_{VF}^A signifies the E_{VF} in pure matrix and E_{VF}^B the one at an impurity. The difference $E_{VF}^B - E_{VF}^A$ denotes the solute-vacancy binding energy E_B. Due to the thermodynamic equilibrium the mentioned "associative" and "dissociative" jumps of the vacancy are directly related to the impurity-vacancy binding energy E_B at the first nearest neighbor separation, see equation 2.10 [29,30,44]:

$$\frac{\omega_4}{\omega_3} = \exp\left(-\frac{E_B}{kT}\right) \tag{2.10}$$

In the definition of equation 2.10 E_B is negative for an attractive binding. Note that the determination of E_B and according literature values for Al alloys will be discussed in section 2.3.2.2 and 2.4.2.1. Inserting equation 2.10 in equation 2.9 leads to the following equation 2.11 [30]:

$$\frac{D_{B^*}(0)}{D_A(0)} = \frac{\omega_2}{\omega_0}\frac{\omega_4}{\omega_3}\frac{f_2}{f_0} = \frac{\omega_2}{\omega_1}\frac{\omega_1}{\omega_3}\frac{\omega_4}{\omega_0}\frac{f_2}{f_0} \tag{2.11}$$

In general the physical quantities which are compared to experimental diffusion data in dilute alloys are all functions of only three independent ratios of these five jump frequencies, namely ω_2/ω_1 (small value if a vacancy favors to jump around the impurity instead of exchanging places with it), ω_3/ω_1 (small value if a vacancy stays near the impurity) and ω_4/ω_0 (large value if a vacancy likes to jump in the vicinity of the impurity instead of away by preferring to exchange places with a matrix atom) [44]. It is possible to determine these ratios with the measurable quantities D_{B^*}/D_A out of equation 2.11, f_2 out of equation 2.12 and the enhancement factor b_1 out of equation 2.14 [30]. Manning (1964, [45]) has shown that the impurity correlation

factor f_2 is a function of the jump frequencies and is given essentially for the five-frequency model by equation 2.12:

$$f_2 = \frac{2\omega_1 + 7F\omega_3}{2\omega_2 + 2\omega_1 + 7F\omega_3} \tag{2.12}$$

F means the fraction of dissociating vacancies that are permanently lost from a site and not compensated by to the impurity returning vacancies [29,30]. F can also be defined as the probability of the vacancy returning to its position after a dissociative ω_3 jump [43]. Manning [45] also considered extensions for the case of vacancy-impurity interactions with second NNs. Regarding F he even considered probabilities of the vacancy returning from second, third and fourth nearest neighboring positions to its original one.

Some background formulas to perform measurements of alloying effects in binary dilute A-B alloys are presented in equations 2.13 and 2.14. Solute concentrations of about 1–2 % are thought to be dilute enough that the diffusion of solute atoms can be considered in terms of isolated atoms or groupings of atoms such as pairs. The results determined are compared with the same quantities measured in pure A in order to find out the difference [29,44].

$$D_{B^*}(C_B) = D_{B^*}(0)(1 + B_1 C_B + B_2 C_B^2 + ...) \tag{2.13}$$

$$D_{A^*}(C_B) = D_{A^*}(0)(1 + b_1 C_B + b_2 C_B^2 + ...) \tag{2.14}$$

The solute enhancement factor B_1 has been calculated for the FCC lattice and extends the five-frequency model [29]. While B_1 takes into account the fact that with a rising B-concentration two atoms will be neighboring a vacancy, for B_2 it would be three atoms [30]. B_1 now includes three new frequencies of the vacancy in the vicinity of two solute atoms: ω_{23} for a solute jump which associates a new solute pair, ω_{24} for a solute jump that dissociates a solute pair, ω_{21} means the reorientation of an existing one [29]. B_1 also depends upon the binding energy between two solute atoms [44]. For the solvent enhancement factor b_1 in equation 2.14 the number of solvent frequencies close to a solute which differ from ω_0, the solvent exchange frequency far from the solute, need to be counted [29]. b_1 describes the effect of an altered vacancy concentration near a solute by reason of the solute-vacancy binding energy. This factor also shows that the main effect of a solute is to increase the total equilibrium vacancy concentration (if b_1 is positive) or decrease it (b_1 negative). This in turn affects the solvent and solute diffusivity in a similar way [44]. A more detailed treatment can be found in [29,30,44].

At higher solute concentrations than 1–2 % the theory becomes still more complicated. Here

cluster formation takes place, i.e. the majority of vacancies is neighbored by more than two solute atoms. Elevated solute concentrations of up to 5 at.% are treated by the "complex model" which has been discussed earlier in section 2.2.2.2.

2.3.2.2 Solute-Vacancy Binding Energy

Already Doyoma in the year 1978 [46] stated that the estimation of the solute-vacancy binding energy E_B would be one of the most important metallurgical problems. Mondolfo (1976, [47]) reviewed all references of solute-vacancy binding energies in Al up to about 1973 and eventually quoted more than 100 different values for a large number of solute atoms [48].

In general, despite a long history of attempts to measure E_B, this value is still extremely difficult to measure accurately. The most noteworthy case of contradictionary experimental values seems to be the Mg-vacancy E_B with more than 20 values mentioned in literature till now. Mg-vacancy binding energies have been reported in a range from an extremely strong binding of ~ -0.4 eV to a very weak, but negative binding of $+0.01$ eV [48].

Determination

Techniques for the determination of E_B can be roughly classified in two categories: on the one hand techniques relying on equilibrium experiments, on the other hand those based on quenching experiments [48]. As far as the theoretical background is concerned, during the treatment of the five-frequency model it has already been mentioned that the only relevant quantity for the determination of the binding energy E_B of an solute-vacancy complex is the ratio ω_4/ω_3. This ratio cannot be inferred from the knowledge of ω_2/ω_1, ω_3/ω_1 and ω_4/ω_0 [44].

Dirkes and Heumann (1982, [49]) worked out a simple procedure to simulate the vacancy trajectory around a solute and proposed to extract E_B from this trajectory. Knowing ω_2/ω_1, ω_3/ω_1 and ω_4/ω_0 truly helps to determine, at each step of a Monte Carlo simulation, the direction of the most likely next jump. But these authors used a false definition of the vacancy concentration on a first neighbor site of the solute. The right definition should include the knowledge of the mean residence time of the vacancy on each site; in other words the inverse of the total escape frequency from this site. Bocquet therefore proposed one more independent frequency ratio, namely ω_1/ω_0 which shall be involved in the fraction of the total time which has been spent on a first-neighbor site of the solute [44].

In addition, diffusion experiments by themselves are not enough to determine E_B. They always have to be related to experiments of another kind: for example a direct determination of the total vacancy concentration in a dilute alloy [44]. According to [48], the technique of combined

length and lattice parameter measurements pioneered by Balluffi (see Balluffi and Ho, 1973 [50] plus section 2.3.3.2) today is generally acknowledged to provide the most reliable way to receive vacancy concentrations.

E_B values based on quenching experiments are always said to be doubtful in [51] because if they are determined from the residual electrical resistivity they cannot follow the microstuctural changes occurring in alloys during quenching operations [51].

To stay with the nomenclature in the literature, in later sections also the term δH_B is used. It signifies the solute-vacancy binding enthalpy which is similarly defined as E_B, i.e. as the difference between the vacancy formation enthalpies at the solute B-atom and the matrix A-atom: $\delta H_B = H_{VF}^B - H_{VF}^A$. The reader may also be remembered of section 2.2.2 where it was discussed that the energy of formation (E_{VF}) can be approximated by the enthalpy of formation (H_{VF}). Nevertheless this assumption was said to not always be safely.

2.3.3 Electronic Effects

Viewing metal-based alloys, Al is in principle the high-valent metal matrix "par excellence". As a consequence its alloying behavior with "simple" metals is in general dominated by the high electron density it provides besides the usual size factor and electrochemical effects [52]. What this means will be discussed in the following sections.

2.3.3.1 Electron Theory of Alloys

As the energy of an atom in a given environment depends almost completely on the atoms immediately next to it, the following first approximation is reasonable: when embedding an atom into a matrix metal, the atom goes into a site containing a homogeneous electron gas provided by the valency electrons of the surrounding atoms. For all "good" metals, like e.g. Al (the definition follows later in this section), every substitutional alloy atom, regardless if it is more electropositive of -negative than Al, embeds electropositively. This means the alloy atom gives one or more of its valency electrons to the electron gas. Here the most elemental picture of spherical ions immersed in a gas of free electrons is used. In alloys where the bonding is predominantly of *sp* type, the positive ions are "bonded" not directly to one another, but to the electron gas. Alloys of "simple" metals are alloys whose atoms interact through their valency s, p electrons, with no or negligible d electron contributions. Plus for these alloys the free or nearly free electron (NFE) models provide a good picture of the electronic state [52].

The earlier mentioned average electron density n_0 of the Al matrix, which dominates the alloying behavior, is high with $\bar{n_0}$=0.027. The electron density means the number of electrons per unit

volume of the electron gas. The volume is measured in atomic units (a.u.), where 1 a.u.=a_0^3 and 1 a_0=0.529 Å=0.0529 nm. In Al even in a vacancy $n_0 \sim 0.01$ is expected at an average. By simplifying the general theory, the so-called local density approximation (LDA), now says that *"all the embedded atom "knows" about its matrix is the local electron density, n_0, provided by its matrix in the embedding site"* [52].

An important effect is the so-called screening that on the one hand contributes to the electrostatic interaction between a solute atom and a vacancy, see section 2.3.3.2, and on the other hand also to the definition of the atomic radius (for more details see [52]). Screening signifies that beyond a certain distance from a charge the electrical field of the charge is insignificant. It is typically measured by the screening length, r_{sc}, and can be said to be extremely effective in a metal. A charge in a medium like Al is screened out well within atomic sizes, i.e. r_{sc}=0.6 a.u.. This concept of r_{sc} stems from the early Thomas-Fermi version of the screening theory, which describes the electrostatic potential V due to a point charge Q varying with distance r as [52]:

$$V = \frac{Q}{r} \exp\left(-\frac{r}{r_{sc}}\right) \tag{2.15}$$

Later theories introduced a different variation of V with r. Particularly they say that V doesn't simply fade away exponentially at large r, but develops so-called Friedel oscillations, i.e. a sequence of spherical shells of alternate excess and insufficient screening charge. Nonetheless the main effect is a sharp fall of the screened potential with increasing distance which is reasonably represented by the screening length r_{sc} [52]. In section 2.3.3.2 a theory is presented for the calculation of the solute-vacancy binding enthalpy δH_B on the basis of the screening potential V. But better results for δH_B, especially for Al-systems, are obtained by taking these Friedel oscillations into consideration as the electronic structure of the conduction electrons is not adequately included by the screening potential method. Corresponding potential approaches used are the pseudopotential method as well as the oscillatory potential method, also discussed by Doyoma (1978, [46]) [30,46]. The pseudopotential in principle describes the behavior of a conduction electron as it enters an atom. A resulting property of metals possessing a pseudopotential, which are so-called "good" metals such as Na, Mg and Al, is that the positive ions at low temperatures are weak scatterers of conduction electrons. At first sight this is surprising, since an ion exhibits toward an incoming electron an electrostatic potential that goes toward minus infinity as the nucleus is approached, which should certainly give intense scattering, see broken line in figure 2.13. This can be explained with the Pauli principle: When the conduction electron enters the atom its wave function takes on an atomic-like state, however then it meets the core electrons of this atom. But as all states of lowest energy are already occupied by the core electrons of the atom the electron has, according to the Pauli principle exclusion from

these states, to behave like as if in an atomic state of higher energy. During the approach of the atom's center now, its potential energy falls, while its kinetic energy accordingly rises because of the sharp bending of its wave function oscillating in this high-energy atomic-like state. Surprisingly in "good" metals the two energies practically cancel. Therefore one can see the kinetic energy as a kind of repulsive "potential" energy practically canceling the electrostatic potential of the ion. The small remaining energy left over from this cancellation is the *pseudopotential*. This simplest picture gives a remarkably good first approximation. The *Ashcroft empty-core pseudopotential* now says that within a critical radius r_c the Pauli repulsion of the core electrons is assumed to reduce the pseudopotential to zero, so that inside r_c the electron behaves as if in a complete empty core, compare figure 2.13. Outside the electron feels the full electrical charge $+Ze$ of the ion (Z: valency, e: electron charge) as a potential $-Ze^2/r$ at a distance r from the center [52].

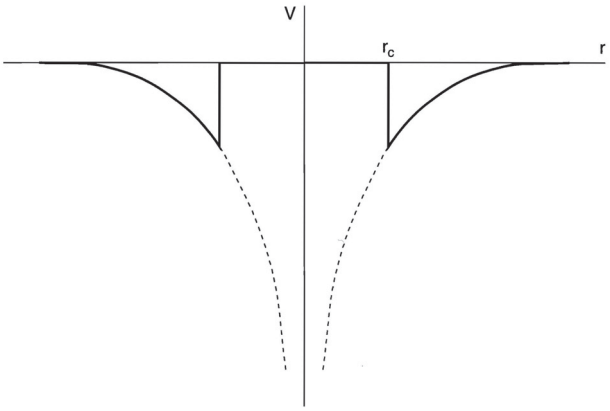

Figure 2.13: Change from full electrostatic potential (broken line) to empty-core pseudopotential (full line) of a conduction electron at distance r from the ionic center [52]

2.3.3.2 Solute-Vacancy-Interactions

The in section 2.2.2 mentioned vacancy concentration measurement method of thermal expansion, i.e. a combined length and lattice parameter measurement, is based on the fact that the formation of a vacancy increases the volume of a crystal by V_{VF}. A rigid lattice now would mean that V_{VF} was equal the atomic volume Ω. But as the atoms surrounding the vacancy relax inward, the volume increase remains smaller than Ω [26].

In pure Al the volume of formation of a vacancy is found to be $V_{VF} = 0.65{\cdot}\Omega$. This means the lattice parameter relaxes inward near a vacancy in Al, on average by $\sim$12 %. The relaxation of neighboring atomic cores around a vacancy can be gained by usage of the electron theory from the screening effect. Just to remind you: this effect describes that an infinite wide spectrum of Fourier waves would be required to screen a point charge. Hence the screening is incomplete and

long-range potential and charge inhomogeneities, so-called Friedel oscillations remain. These oscillations lead to an interaction energy between two atoms, which is determined by the Fermi energy E_F, i.e. by the electron concentration (for more details see [26],6.3.3). The relaxation of neighboring atomic cores around a vacancy is therefore due to the negative charge on the vacancy that extends beyond its nearest neighbors in a univalent metal – i.e. a metal with one valence electron – so that they relax inward. The next nearest neighbors on the other hand relax outward due to Friedel oscillations. In multivalent metals – i.e. metals with several valence electrons – these relaxations can be in the opposite direction. Two vacancies can interact in a similar way [26].

Thermodynamically for the solute-vacancy binding enthalpy of a solute B in matrix A is valid: $\delta H_B = H_{VF}^B - H_{VF}^A$. For the case of a solute-vacancy attraction the vacancy formation enthalpy at the B atom H_{VF}^B is smaller than H_{VF}^A, δH_B gets negative. As announced in section 2.3.3.1 a calculation of the solute-vacancy binding enthalpy δH_B on the basis of the Thomas-Fermi screening potential V will be provided now. If we limit ourselves to the electrostatic interactions between solute and vacancy δH_B gets [30]:

$$\delta H_B = -Z_0|e|V(r) \tag{2.16}$$

With Z_0 being the valency of the matrix atoms, i.e. $+3$ for Al, $-Z_0|e|$ denotes the corresponding deficit of the electric charge of a vacancy. Here $V(r)$ can be written as [30]:

$$V(r) = \frac{Z|e|}{r}\alpha \exp(-qr) \tag{2.17}$$

$Z|e|$ signifies the excess charge of the solute possessing the valency Z_2 with $Z|e| = (Z_2 - Z_0)|e|$. α is a function of Z, q denotes the screening constant which derives from the electron density at the Fermi level. δH_B now is to calculate for $r = d$, the smallest atomic distance, i.e. the jumping distance. Equations 2.16 and 2.17 result in [30]:

$$\delta H_B = \frac{-Z_0 Z}{d} e^2 \alpha \exp(-qd) \tag{2.18}$$

Note that this screening potential method has been described for illustrative purposes only because it is unsatisfactory for the following reasons: The impurity atoms are just characterized by the valency-difference of the impurity and matrix atoms, i.e. vacancy-impurity interaction energies vanish for impurity atoms with the same valence as the matrix atoms. Another reason is that the oscillatory behavior of the potential has not been taken into account, this has already been discussed in section 2.3.3.1 and reviewed by March and Rousseau (1972, [53]) [46].

Although the pseudopotential and the oscillatory potential methods would lead to better results for Al-systems, no volume differences between the pure metal A and the solute B are taken into account. But according to Neumann (1983, [54]) they must not be ignored [30]. The corresponding size effect is treated in section 2.3.3.4. Note that the computed solute-vacancy interaction values of section 2.4.2.1 obtained by [48,55] and [43] seem to take account of all these influences mentioned just earlier [55]. and [43] even combine their computations with the theory treated in sections 2.3.1 and 2.3.2.

Due to the different atomic size and an (screened) extra charge, the attractive interaction between solute atoms and vacancies can be up to 0.3 eV. The energy of vacancy formation E_{VF} would be reduced by this amount next to a solute atom, i.e. c_V would be increased [26].

2.3.3.3 Solute-Solute-Interactions

Provided that the solution in the matrix is sufficiently dilute, atomic solution can certainly be a thermodynamically stable alternative state for bulk condensed matter, even for a large binding energy of the condensed matter. The question in this instance is whether the sparsely dissolved solute atoms attract or repel. The standard theory of non-ideal, dilute solutions appropriately covers the small effects which appear here. As repelling atoms rarely meet in a dilute solution, the effect is small on the one hand, on the other hand when they attract strongly this leads the atoms to join up and form a separate condensed phase, like that excluding them from solution in the matrix, which again gives a small effect. But more interesting behavior becomes possible as soon as the interacting solutes are of different elements. When the solutes are concentrated many types of solute-solute interactions become possible. This is also valid for atoms interacting covalently [52].

Note that the alloy used in this work all in all contains about 2 at.% of solute atoms, compare table 4.1. The impurity correlation factors discussed in section 2.3.2.1 are presumably appropriate for impurity concentrations of up to about 1 at.%. At higher concentrations the impurities cannot be considered independent anymore, i.e. correlation events themselves aren't independent. This represents a special difficulty as there is no easy way of e.g. extending the five-frequency model into the concentrated regime without quickly increasing the number of jump frequencies to an unworkable number [29].

This results further in the fact that the diffusion behavior of concentrated single-phased alloy solid solutions with substitutional impurity atoms distinguishes in many ways from that of infinitely dilute solid solutions. Therefore it is convenient to sub-divide concentrated alloys into such containing up to 5 at.% of solute (elevated concentration) and such that comprise the whole solubility range and therefore also systems with full miscibility (highly concentrated

alloys). The basis for the description of the diffusion behavior of alloys with elevated concentrations is the complex model, which has already been superficially treated in section 2.2.2.2 [30]. Further the reader may be remembered of the model for 1-2 % solute concentration described in the second half of section 2.3.2.1.

Another effect influencing the solute-vacancy interactions are solute-solute interactions in form of hybridization. Interpretations of computed solute-vacancy interaction values based on this effect will be discussed in section 2.4.1. It is also an explanation for a solubility phenomenon of solute atoms in Al, see section 2.4.1.2. Hybridization means that when two atoms come within about 2 a.u. (definition see section 2.3.3.1) of each other, one can no longer regard them as having two separate, atomic, wave functions. The reason is that an electron of one atom feels the electric field from the other and so, to some extend, then belongs to the wave function round the other nucleus, more precisely there is just a single wave function centered about both nuclei. According to the molecular orbital theory an overlap of two atomic orbitals results in two molecular orbitals, a binding and an antibinding one. Important now is that the one-center functions may have same or opposite signs, i.e. either an attractive *bonding* state is formed (same signs) or a repulsive *antibonding* state. Figure 2.14(a) shows how in the bonding case the original energy level of the combining states ($\varepsilon_1 = \varepsilon_2$) is reduced by $-V_1$ while in the antibonding one shorter wavelengths of higher energy ($+V_1$) result. For different kinds of atoms, figure 2.14(b), the combining states are at different energy levels, this means that the energy level of the lower state, ε_1, is still more lowered while the higher energy state, ε_2, is equally raised. The preferential filling of the bonding states now results for incompletely filled valency shells in a predominating bonding energy against the overlap repulsion at the equilibrium spacing. However, for full shells, like in approaching inert gases or in ionic compounds, then the complete filling of the antibonding levels nullifies the gain from the bonding levels [52].

In transition metals (TM) an overlap of the broad *sp* conduction band and the *d* band, pictured in figure 2.14(c), leads to hybridization between the two bands. But the *d-sp* resonance appears to be strong only in the range of 2 to 6 eV below the Fermi energy E_f. In late TMs like Cu, Ag and Au and noble metals the d shells lie at lower energies, i.e. a few eV below E_f and so hybridize less strongly with the empty states above. The reason is that at the E_f itself the sp band has mostly recovered its simple free electron form, almost as if the d resonance were not present. Therefore Cu, Ag and Au behave like monovalent metals in alloys with solutes of Zn, Al, and Sn. Nevertheless the role of the d band cannot entirely be ignored, see section 2.4.1.2. The large solubility of Ag in an Al matrix for example is explained by the influence of hybridization while its neighboring element Cd only exhibits a very low solubility because no hybridization occurs for Cd in Al [52].

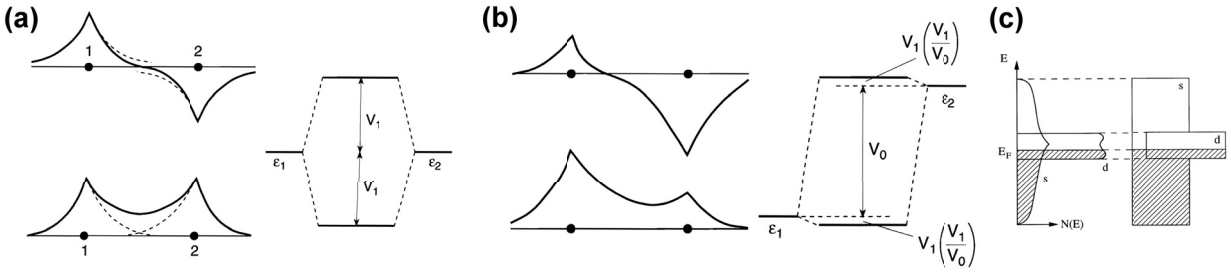

Figure 2.14: (a) Hybridization of the same kind of atoms and (b) different kind, corresponding two-center wave functions pictured left, respectively [52]; (c) overlapping of *s* and *d* bands in TMs

2.3.3.4 Size Effect

Placing now large impurity atoms in an Al matrix results in a significant strain on the surrounding Al atoms. A vacancy beside this large impurity atom allows the impurity to relax toward the vacancy and thus away from the other neighboring Al atoms. Hence, the vacancy in a NN position to a large impurity helps to relieve the strain, resulting in a reduced energy of the impurity-vacancy pair, equivalent to an attractive (negative) binding energy [48].

In general, for embedded atoms the principle of constant atomic volume in alloys is not exact. There is for example a dependence on the electron density of the environment of an embedded atom. But as a result of opposing contributions, the atomic radius stays as an approximately constant feature in many alloys. This is also supported by theoretical calculations which show that both the electric charge and the local density of states (LDOS) of an atom are commonly nearly the same in the alloy as in the elemental metal. If it is not possible for the alloy atom to have the same size as in its own bulk metal, due to incompability with the size of the matrix atoms, there is an extra energy because of the strain of atomic misfit. The localized picture and misfit model are justified though by the general requirement for electrical neutrality in a metal which implies that every atom retains virtually all its valency electrons within its own atomic cell [52].

2.4 Vacancies and (Micro)Alloying Elements in Aluminum

In general three common features have been identified which seem to be common for most trace element effects in Al alloys. First they have only sparing solid solubility in the alloys. Secondly there is the indirect, but strong evidence that trace elements interact with, and change the distribution of vacancies which were retained during quenching. Thirdly such interactions may have a profound influence on nucleation processes [56].

The aim of the following sections is to provide a basic understanding about the backgrounds of

interactions of vacancies with solute atoms and accordingly with MA elements. These informations are later on used to try to predict and interpret the practical results of the measurements performed in this work.

2.4.1 Relevant Properties of Solute Atoms in Aluminum

2.4.1.1 Size and Valency

Table 2.1 lists literature values for the atomic sizes and the valency of alloying elements in an Al matrix (FCC), additionally it includes the atomic structures of the pure elements. Note that only the in this work relevant alloying elements are considered.

For pure metals the trends in atomic sizes, i.e. the ionic radius, follow the periodic table as follows: First, the radius rises down the columns due to the extra Pauli repulsion of increasing numbers of filled shells in the core, this pushes the valency electrons more outward each step downward. Second, from left to right along the periods the radius declines because of the increasingly strong nuclear attraction [52].

There are also atoms of variable size, like tin (Sn). Above 13 °C Sn undergoes a transition from gray Sn (diamond structure) to white Sn (tetragonal and metallic). The gray variant has an atomic radius of 141 pm while the white one is 158 pm large [52].

2.4.1.2 Solubility

For an increasing size factor, i.e. an increasing atomic size difference, an phase diagram with only limited solid solubility is eventually favored, e.g. an eutectic one. But such a diagram could also result from a difference in crystal structures of pure A and B, even for same sizes of these atoms [52].

As already mentioned in section 2.3.3.1, in Al even in a vacancy the electron density $n_0 \sim 0.01$ is expected at an average. This is relevant when embedding substitutional atoms as due to such a large n_0 in a vacancy of the Al matrix the number of core electrons in the embedded atom becomes important because the Pauli repulsion results in a high and unfavorable embedding energy leading to insolubility. Thus it was found that, when other factors are favorable, Al is a pretty good solvent for metals of low atomic number, e.g. Li, Mg, Zn, Ag, but not for those of high number, e.g. Cd, In, Sn, Te, Au. The boundary happens to come between Ag and Cd. Such a different behavior as solutes in Al may seem extraordinary as they are neighboring elements in the periodic table. Here however, the d states play a significant role. In Ag the d band lies reasonably high in the conduction band and therefore interacts favorably by hybridizing with

Table 2.1: For an Al-matrix: solute atomic radius (r_S), solute-Al ratio of atomic radius, the relative partial molar volume of the solute and solute-valencies (Z). As a comparison: $r_{Al} = 143.2$ pm (see periodic table), $Z_{Al} = 3$, Al=fcc. Further: [PT]=out of periodic table, est.=estimated values. Additionally listed: pure metal crystal structures

Solute S	$\frac{r_S}{r_{Al}}$	$r_S - r_{Al}$	r_S	$\frac{V_S}{V_{Al}}$	Z	Structure
		[pm]	[pm]			
Mg	1.12	+16.9	159.7[a]		2	hex
Si	0.978	-5.4	139.2[a]		4	diamond
Cu	0.898	-15.3	128.4[a]	0.84	1	fcc
Li	1.09	+12			1	bcc
Ca	1.38			1.46		fcc
Sr				1.75		fcc
Ba			217.4[PT]			bcc
Ag	1.01	+1.3		1.03	1	fcc
Cd	1.09			1.2		hex
In	1.16			1.29	3	tetrag.
Ge	1.03			1.08	4	diamond
Sn	1.18	+19.4	158[b]	1.34	4	tetrag.
Pb	1.22	+27.5		1.51	4	fcc
Sb		+22.8		1.37	5	rhomboed.
Bi	1.29	+34.7		1.57	5	rhomboed.
Fe	0.893	-16.9			2, 3	bcc
Mn	0.903	-16.1		0.78	2, 4, 7	cubic
Cr	0.984	-15.3		0.80	2, 3, 6	bcc
Ni	0.870	-18.5			2	fcc
Zn	0.972	-9.0		0.98	2	hex
Ti	1.02	+3.8		0.97	4	hex
B		-44.9				hex
Be	0.788				2	hex
Ga	1.06	-2.5			3	orthoh.
Na	1.33	+46.7			1	bcc
V	0.944	-9.1			2-5	bcc
Zr	1.12	+16.8			4	hex
Ref.	[39]	[2,57]	[43][a], [52][b]	[55],fig.3	[39]	[PT]
NOTE	[1971]	[1984]		est.,[2009]		

the sp conduction states of Al. In Cd on the other hand the d states lie at much lower energies and behave as core states rather than valency ones [52]. So for Cd no hybridization happens.

Al generally combines well with TMs which have not much primary solubility and mainly forms intermetallic phases. As the partly-filled d shells are narrow bands with an energy near the Fermi level these metals are able to hybridize strongly with the sp electrons of the Al conduction band. Further, in the early TMs which possess low-filled d bands, there exist empty d orbitals of bonding symmetry and no occupied antibonding ones, what this means see section 2.3.3.3. Therefore conditions are preferable for good cohesion with a high-valency metal such as Al [52].

2.4.2 Investigated Interactions in Aluminum Alloys

2.4.2.1 Binding Energy-Calculations and Five Frequency Model-Values

In the year 2007 Wolverton [48] proposed a new method with which solute-vacancy binding energies E_B can be obtained, i.e. first-principles atomistic calculations. This method uses the plane wave pseudopotential method which is implemented in the Vienna ab initio Simulation Package (VASP). For exchange correlation, the LDA as well as the generalized gradient approximation (GGA) are used. Further it is important that all calculations are fully relaxed, i.e. no rigid lattice is assumed. Later in 2009 Simonovic and Sluiter [55] also used ab initio VASP calculations to obtain solute-vacancy binding enthalpies δH_B as well as the solute migration enthalpies H_M^B and Al migration enthalpies $H_M^{Al(1)}$ and $H_M^{Al(3)}$ on the basis of the five-frequency rate model. These values served to receive solute diffusion activation energies Q. Not much later Mantina et al. [43] used the first principles approach with VASP to calculate the diffusion pre-factor (D_0) as well as Q values for Mg, Si and Cu in fcc Al. From density-functional theory (DFT) they gained all necessary microscopic parameters for D_0 and Q: the correlation factor f_2 through a five frequency model, all defect jump frequencies ω_i plus the enthalpies of vacancy formation H_{VF} and solute-vacancy binding δH_B.

The results of all three papers including the provided interpretations are presented subsequently. Again only the in this work relevant alloying elements are listed. Table 2.2 lists all values in kJ/mol, i.e. if necessary values originally given in eV were converted to this unit and rounded. We also stay with the convention from earlier in this work where a negative binding energy or enthalpy was defined as an attractive solute-vacancy binding. If not said otherwise, only values obtained with the LDA method are listed, exceptions may be marked with (g) for GGA. Values with a $^{(M)}$ take a so-called spin polarization effect into account (for further explanation see [55]).

Similar to equation 2.4 the vacancy jump frequency can also be written as [43]:

$$\omega = \nu^* \exp\left(-\frac{H_M}{kT}\right) = \nu^* \exp\left(-\frac{H_M}{RT}\right) \tag{2.19}$$

H_M describes the change in enthalpy of the system between two states of the diffusing atom, i.e. the stable initial minimum-energy lattice position and the energy of the activated transition state at the saddle point along the diffusion path, compare figure 2.9. ν^* is the effective frequency described as the quotient of the products of the vibrational frequencies of those same two configurations normally being in the order of magnitude of 10 THz=10^{13} Hz [43,55].

With exclusion of the 3d TMs (Sc-Zn), already Wolverton [48] observed the following trends

Table 2.2: Solute-vacancy binding energies E_B and enthalpies δH_B, solute migration enthalpies H_M^B, Al migration enthalpies $H_M^{Al(1)}$ and $H_M^{Al(3)}$ plus diffusion activation energies Q, all in units of kJ/mol. D_0 in 10^{-6} m^2/s. Al-data concerns only pure Al. Solutes marked with an asterisk (*) signify that their diffusion in Al is dominated by Al-vacancy interchanges (according to [55]). References are: Wolverton [48], Simonovic and Sluiter [55], Mantina et al. [43] and Erdelyi et al. [58]

Solute	E_B	δH_B	δH_B	H_M^B	H_M^B	$H_M^{Al(1)}$	$H_M^{Al(3)}$	Q	Q	D_0
Al		0 (-72)	0 (-68.5)	49	56.0	49	49	121		
Mg*	1.9	-1	6.8	38	40.5	61	46	117	122.5[a]	11.9[a]
Si*	-7.7[g]	-5	-10.6	44	53.1	46	54	113	111.0[a]	3.66[a]
Cu*	∼-1.9	+0	-2.9	42	55.0	35	52	114	120.6[a]	4.37[a]
Li*		6		35		53	47	124		
Ca*		-21		10		92	52	104		
Sr*	-69.5	-71		<10		123	91	92		
Ba	-137.0									
Ag*	-6.8	-9		36		50	57	113		
Cd*	-13.5	-15		24		64	57	114	124.3[b]	104[b]
In*	-19.3	-21		24		70	58	109	122.7[b]	116[b]
Ge*	-12.5[g]	-11		33		55	58	116		
Sn*	-24.1	-25		25		68	59	106	118.6[b]	84[b]
Pb*	-39.6	-39		11		78	67	100		
Sb*	-29.0	-30		24		72	63	105		
Bi*	-42.5	-42		15		79	69	99		
Fe	∼0	2		131				205		
Mn	7.7	9		147				228		
$Mn^{(M)}$		6		90				168		
Cr	24.1	18		152				241		
$Cr^{(M)}$		13		115				200		
Ni	-2.9	-4		77				144		
Zn*	-2.9	-4		26		50	56	118		
Ti	33.8	25		111				208		
B										
Be										
Ga*	-6.8	-7		30		52	55	117		
Na										
V	31.8	24		141				238		
$V^{(M)}$		24		127				223		
Zr	27.0	19		91		52	26	182		
Ref.	[48]	[55]	[43]	[55]	[43]	[55]	[55]	[55]	[43][a], [58][b]	
NOTE	GGA[g]	630 K	400 K	630 K	400 K	630 K	630 K	630 K	400 K[a]	400 K[a]

by comparing isoelectronic sets of solutes, meaning solutes in the same column of the periodic table, as well as solutes in the same row of the periodic table: the larger the atom, the stronger the solute-vacancy binding. But they also didn't know how to explain some obvious exceptions to this size-effect like Si and Mg. Si is smaller than Al as a dilute impurity, but still has an attractive binding energy. Mg on the other hand is notable as a large impurity with no solute-vacancy binding energy. Hence they concluded that solute size is not the only factor controlling the binding.

Table 2.3: Calculated five jump frequencies ω_i [Hz] and correlation factor f_2 for impurity diffusion together with jump frequency ratios entering equation 2.11. All results are valid for T=400 K using H_M^B from table 2 and ν^* from table 3 in reference [43]

Solute	ω_0	ω_1	ω_2	ω_3	ω_4	$\mathbf{f_2}$	$\frac{\omega_4}{\omega_0}$	$\frac{\omega_1}{\omega_3}$	$\frac{\omega_2}{\omega_1}$
Mg	$8.31{\cdot}10^5$	$0.581{\cdot}10^5$	$918{\cdot}10^5$	$66{\cdot}10^5$	$10.9{\cdot}10^5$	0.16	1.3	0.01	1580
Si	$8.31{\cdot}10^5$	$33.5{\cdot}10^5$	$18.6{\cdot}10^5$	$1.24{\cdot}10^5$	$17.6{\cdot}10^5$	0.66	2.1	27.2	0.56
Cu	$8.31{\cdot}10^5$	$2390{\cdot}10^5$	$7.17{\cdot}10^5$	$6.72{\cdot}10^5$	$18.7{\cdot}10^5$	0.99	2.2	354.98	0.003

Simonovic and Sluiter [55] also observed regions with strong vacancy binding: e.g. large earth alkaline atoms such as Ca and Sr and heavy metals such as Bi and Pb. Because of its size, 1.75 times larger than Al, Sr has a very large solution energy of about 102 kJ/mol. Also therefore the Sr atom forms a complex with a vacancy with Sr displaced toward the vacancy. Thus, with Sr already almost at the midpoint, the vacancy H_M^B is very low. However Sr diffusion is not necessarily very fast as it is limited by Al-vacancy interchanges in the immediate vicinity of the solute that differ strongly from the interchanges in pure Al, this can be seen from $H_M^{Al(1)}$ and $H_M^{Al(3)}$ in table 2.2. Note that the last two values can be used to estimate ω_1 and ω_3 according to equation 2.19 while H_M^B is correlated with ω_2. Other large atoms, such as Ca, Pb and Bi, also were found to behave similar to Sr. Further a positive correlation between δH_B and partial molar volume V_S/V_{Al} was observed for Cu-Ge, Pd-Sb, Pt-Bi and La-Lu. Wolverton [48] presumed that Pb and Bi don't yield the same effect in Al-Cu as Sn [59,60] due to their lack of solubility in Al. Note that Sn-added Al-Cu alloys are discussed in section 2.5.1.1.

TMs, however, were found to behave completely different by [48] and [55]. According to Simonovic and Sluiter [55] TMs generally appear to repel vacancies regardless of their atomic volume. In the sequence V-Co the vacancy repulsion even gets stronger as the atomic size increases. The strongest repulsion occurs in column 5a in the periodic table (e.g. V), these are TMs with about the same partial molar volume as Al. The smallest elements, Co and Fe, do not significantly interact with vacancies at all. So TM solutes do not interact through a strain caused by volume changes but repel vacancies due to the strong Al-TM bond. Placing a vacancy next to the TM causes an unfavorable energy change due to the traded weaker Al-Al bond. Thus the strong Al:sp-TM:d hybridization might cause higher migration barriers than for elements that do not hybridize, with increasing barriers for stronger hybridization. The strongest hybridization occurs for about half-filled d bands, i.e. around column 6a (e.g. Cr), while it is negligible for nearly filled or filled d bands [55]. Compare values listed in table 2.2.

Normal "free-electron" metals, as for example Li, Mg, Zn, Cu, Ag and even Si in a high coordinated metallic environment, that possess atomic sizes similar to Al, all should have weak vacancy binding only as well as migration barriers fairly close to that of Al itself, as would be expected from the nondirectional metallic bonding [55]. Note that all these comparisons with

Al have to be seen in relation to other possible solute atoms which can be alloyed in Al.

The diffusion activation energies Q also correlate well with partial molar volume, like the in table 2.2 listed δH_B values do. The TMs follow again a completely different trend with Q values larger than that for Al self-diffusion [55]. Simonovic and Sluiter [55] also remarked that in concentrated Al-TM alloys Q values for TM impurities may vary strongly with the impurity concentration as the bonds are not strongest in the middle of the TM series anymore.

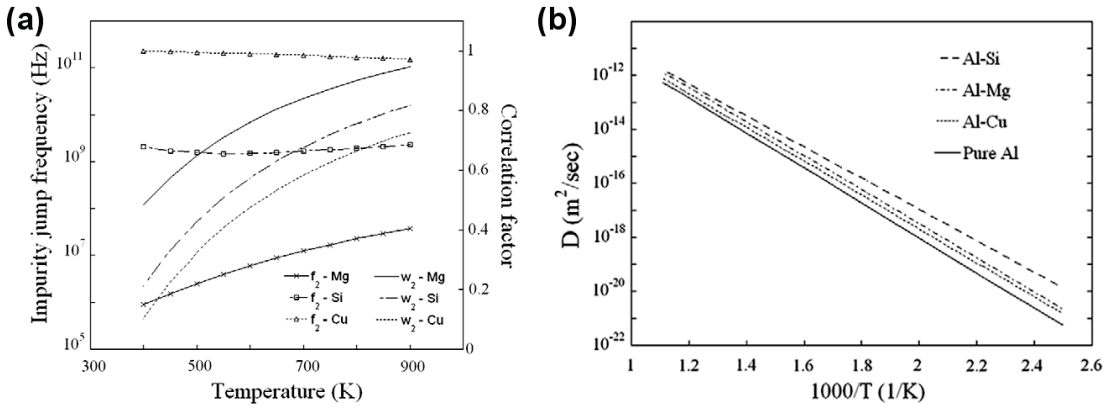

Figure 2.15: (a) Exchange frequency ω_2, correlation factor f_2 and (b) calculated diffusion coefficients D of impurities Mg, Si and Cu in Al as a function of temperature. D is also compared to Al self-diffusion. [43]

Mantina et al. [43], like others, generally found that values obtained with LDA show better agreement with experimental data than those from GGA. Figure 2.15 illustrates the temperature dependence of various values listed in table 2.3. The data shows that Cu possesses the lowest jump frequency ω_2 in Al due to the low ν^* (10.9 THz) and high H_M^B (55.0 kJ/mol). Likewise Mg's highest ω_2 arises from the high ν^* (18.6 THz) and low H_M^B (40.5 kJ/mol). What this means for the impurity diffusion correlation factor f_2 can be derived from equation 2.20 after Le Claire (1970, [61]), compare equation 2.12:

$$f_2 = \frac{1 + 3.5(\omega_3/\omega_1)F(\omega_4/\omega_0)}{1 + (\omega_2/\omega_1) + 3.5(\omega_3/\omega_1)F(\omega_4/\omega_0)} \tag{2.20}$$

The larger ω_2 and the lower ω_1 and ω_3, the lower f_2, indicating a highly correlated motion of the solute atom. The data of table 2.3 reflect this behavior. Figure 2.15(a) shows that the Cu and Si diffusion correlation factors stay nearly constant with rising temperature while for Mg f_2 increases, at the same time decreasing Q of Mg. For an additional interpretation of this behavior remember section 2.3.3.2, also bear in mind that f_0 of an FCC matrix (like Al) is 0.78, see section 2.3.2. There exists a positive correlation between D_0 and Q: $D_{0-Mg} > D_{0-Cu} > D_{0-Si}$ and $Q_{Mg} > Q_{Cu} > Q_{Si}$. Figure 2.15(b) illustrates the calculated diffusion data resulting from the equation $D = D_0 \exp[-Q/(RT)]$ at 400 K: $D_{Si} > D_{Mg} > D_{Cu}$. According to Mantina et al. [43] trends in solute diffusivities have been described in terms of the solute atomic size and its

excess valence or its solubility in the matrix element or correlated to trends in activation energies or even migration barriers. The present authors however see that such simple descriptors don't even provide a qualitative explanation of the diffusion coefficients. Thus they conclude: *"For a quantitative understanding of the diffusion coefficients, or even a qualitative description of trends, we find that it is crucial not only to assess the migration barriers and activation energies, but also to understand in detail the underlying factors entering the diffusion pre-factor, including the contribution of the correlation factor."* [43]

2.4.2.2 Cluster Formation

Recently Zurob and Seyedrezai (2009, [13]) presented a model for the growth of clusters during the NA of Al alloys based on vacancy trapping. A key feature of their derivation is that the only driving force for cluster formation is the interaction between solute atoms B and vacancies □. There is no necessity for a chemical supersaturation of B atoms. Further no kind of solute-solute interactions have been considered.

The theoretical background of their model is based on the theory of the correlation effects. Standard treatments of this theory in diffusion would lead to the suggestion that a vacancy would spent more time around a solute atom because of repeated exchanges with the solute atom or with atoms that neighbor the solute atom. Such exchanges would result in a migration of the vacancy and the solute atom as a complex. But if the vacancy were to exchange sites with a solvent atom which does not neighbor the solute atom in question, a dissociation of the vacancy-solute pair would be the consequence and like that the vacancy would become free. As a proper treatment of correlation effects would be complex, particularly if multiple solute atoms are involved, Zurob and Seyedrezai simplify their approach by defining E_B as follows: the probability of the vacancy escaping from the solute atom, i.e. the probability of dissociation of the vacancy-solute complex [13].

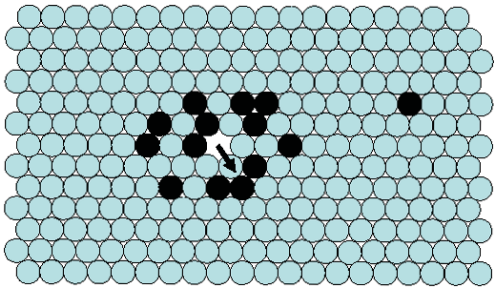

Figure 2.16: Illustration of a solute cluster: solvent in gray, solute atoms in black, several jumps are needed for a vacancy escape [13]

Thus the cluster formation process is pictured as follows: After a single quenched-in vacancy encountered a B atom, a B-□ complex forms if the solute-vacancy binding energy E_B is attractive.

The larger E_B, the longer the complex-lifetime. During its lifetime it migrates and encounters other B atoms of which some could join the complex. The more B atoms joined, the more stable is the complex and migration becomes more sluggish, i.e. the vacancy is trapped in a stationary cluster. For the subsequent cluster growth the vacancy has to escape the cluster, enter the matrix and bring other solute atoms, see figure 2.16. The probability of the vacancy escaping the cluster is proportional to the number of consecutive jumps needed and thus proportional to the number of solute atoms in the cluster. This escape is therefore seen as the rate-limiting step for cluster formation. Once escaped, the vacancy can form a new B-□ complex and evolve into a cluster. This would provide an explanation how it is possible that the number of clusters in the material is as much as 10 times that of vacancies. Alternatively the B-□ complex joins an existing cluster. This would happen since the effective binding energy of the vacancy to n solute atoms is larger than its binding energy to a single solute atom B. For further cluster growth another vacancy escape would be nessesary. The number of atoms in a cluster was derived to increase linearly with ln(t) during isothermal NA. For chemical supersaturation of B, upon heating these clusters may develop into precipitates or otherwise, diffuse out due to activated diffusion of B atoms [13].

Considered solute-solute interactions between B atoms and a second solute (C) now would lead to complex effects which depend on the magnitudes of the B-B, C-C, B-□, C-□ and B-C interactions. One possible consequence is co-cluster formation. In addition a strong attractive B-C interaction along with strong repulsive C-□ interaction may prevent clustering even if the B-□ interaction is attractive [13].

2.5 Possible Changes in Precipitation Behavior Due to Addition of Microalloying Elements to AA6061

2.5.1 Possible Change in Cluster Formation

Changes in precipitation reactions due to the presence of minor amounts or traces of certain elements, so-called MA effects, can arise for numerous reasons including [8]:

1. A preferential interaction with vacancies can reduce the rate of nucleation of GP zones [8]
2. Raise of the GP zone [8] solvus which alters the temperature ranges over which phases remain stable
3. Stimulated nucleation of an existing precipitate by reduction of the interfacial energy between precipitate and matrix

4. Promoted formation of a different precipitate
5. Provision of heterogeneous sites at which existing or new precipitates may nucleate. These sites can be clusters of atoms or small particles
6. Increase of supersaturation so as to stimulate the precipitation process

2.5.1.1 MA Elements Sn, In, Cd in Al-Cu

An early example of a MA effect was the role of small additions of Cd, In or Sn in changing the age-hardening response of binary Al-Cu alloys. These elements decrease RT (natural) aging since they react preferentially with vacancies and thereby retard GP zone formation (mechanism 1). However, both the rate and extend of hardening at elevated (AA) temperatures are enhanced as these MA elements promote precipitation of a finer and more uniform dispersion of the semi-coherent θ' phase (Al_2Cu) in preference to the coherent θ'' phase. It would have been first proposed that absorption of these elements at the θ'/matrix interfaces lowers the interfacial energy required for nucleation of θ' (mechanism 3). Further observations also indicated that θ' appears to be associated with small Sn clusters or particles of about 5 nm in diameter which suggests that heterogeneous nucleation occurred (mechanism 5) [8].

Čížek et al. [62] studied the annealing process in quenched binary Al-Sn alloys with 800 at.ppm Sn with PAS. They propose that due to the high binding energy of Sn to □, thermal vacancies can be bound to dissolved Sn atoms during the solution treatment. Therefore after quenching (to RT) a significant amount of Sn atoms can be coupled to vacancies, while the "free" vacancies quickly disappear after and/or during the quench. Measurements indicate a domination of vacancy-Sn pairs, while Sn-clusters associated with vacancies cannot be excluded. But concentrations of $□_2$-Sn and □-Sn_2 would clearly be significantly smaller than of □-Sn. If such Sn-clusters formed, they should be coupled with vacancies because of the high E_B plus the mobility of Sn-vacancy pairs in Al is notably higher than that of Sn atoms themselves. The mean diffusion length of Sn atoms in Al at RT is calculated to be about 0.2 nm in 24 hours. 24 hours refers to the typical time scale of a PALS measurement [62].

For Al-Cu-Sn alloys Silcock et al. [63] reported several examples of segregation during quenching or before examination, which is thought remarkable. They referred to a proposition that Sn distribution might not be uniform at solution treatment temperature [63]. This is thought consistent with the findings described just earlier for the Al-Sn alloys.

Hirosawa et al. [64] measured the change in electrical resistivity for Al-Cu-Sn alloys during aging at 278 K, see figure 2.17(a). The Sn-addition retards the initial increase of resistivity without rising the resistivity maximum. This stays in contrast to the later discussed Mg-added alloys.

According to Sato et al. [7] the Cu/Sn/vacancy complex clusters do not serve as effective nucleation sites for GP zones [7].

Bourgeois et at. [65] analyzed the interaction between vacancies, Cu and Sn in an Al-1.7at.%Cu-0.01at.%Sn alloy (i.e. 100 at.ppm Sn). They introduced a NA step before conventional AA. According to them NA normally restricts the diffusion of quenched-in vacancies and solute atoms to relative localized regions of $<$100 nm [65]. A key result of their study is that the earlier the effect of NA on an increased hardness during AA is to appear, the longer NA durations are required, see figure 2.17(c). Also due to other measurements they conclude that metastable groupings are formed during NA which cause a reversion plus promote formation of GP(I) zones and to a lesser extent θ" during subsequent AA without disadvantaging the still predominating θ'. An additional refinement in the θ' and θ" distribution explains the hardness increase. So the groupings seem to be transient in nature, even at RT with the most beneficial effect on AA after 72 hours, compare figure 2.17(b). After 72 hours of NA 3DAP atom maps revealed Sn atoms being mainly present as pairs or individually. These are believed to be attached to one or more vacancies. Also present are smaller Cu(-Sn) clusters of typically 5–10 atoms and rarely fifteen or more atoms. So a strong tendency for clustering of Cu and Sn atoms to their own kind is confirmed, but only weak co-clustering was observed. After 500 hours of NA co-segregation of Cu and Sn is more evident, clusters grew and contain more Sn atoms. Thus a too short NA stage seems insufficient for the Sn-vacancy complexes to form while a too long NA time leads to Sn and Sn-Cu clustering and thus a lack of mobility of larger clusters. At 160 ℃ most Sn-vacancy clusters are expected to stay bound due to their large E_B. Further it is believed that the assistance through NA provided by Sn in the formation of Cu GP(I) zones follows another mechanism [66] from that promoting the nucleation of θ' [65].

Recently Bourgois et al. [66] more closely examined the mechanisms by which Sn promotes the nucleation of θ'. Prior to them Silcock et al. [63] reported two possible mechanisms for the nucleation of θ' influenced by trace additions of Cd, In, or Sn: at and above 200 ℃ heterogeneous nucleation on small particles of the MA element and below 200 ℃ incorporation of the MA element into the interface of θ' nuclei. Bourgois et al. [66] found the following reasons for Sn in accommodating the misfit between Al and θ': so-called "magic thicknesses" of θ' are favored due to configurations of low volumetric strain, i.e. lowering of the interfacial energy, and/or low shear strain, but Sn does not accommodate residual volumetric misfit strain while it remains unknown if it could nevertheless accommodate the transformation strain associated with nucleation or thickening. Particularly at lower temperatures of 160 ℃ also θ' platelets free of Sn precipitates were found pointing to a process of Sn being active as solute rather than as precipitate.

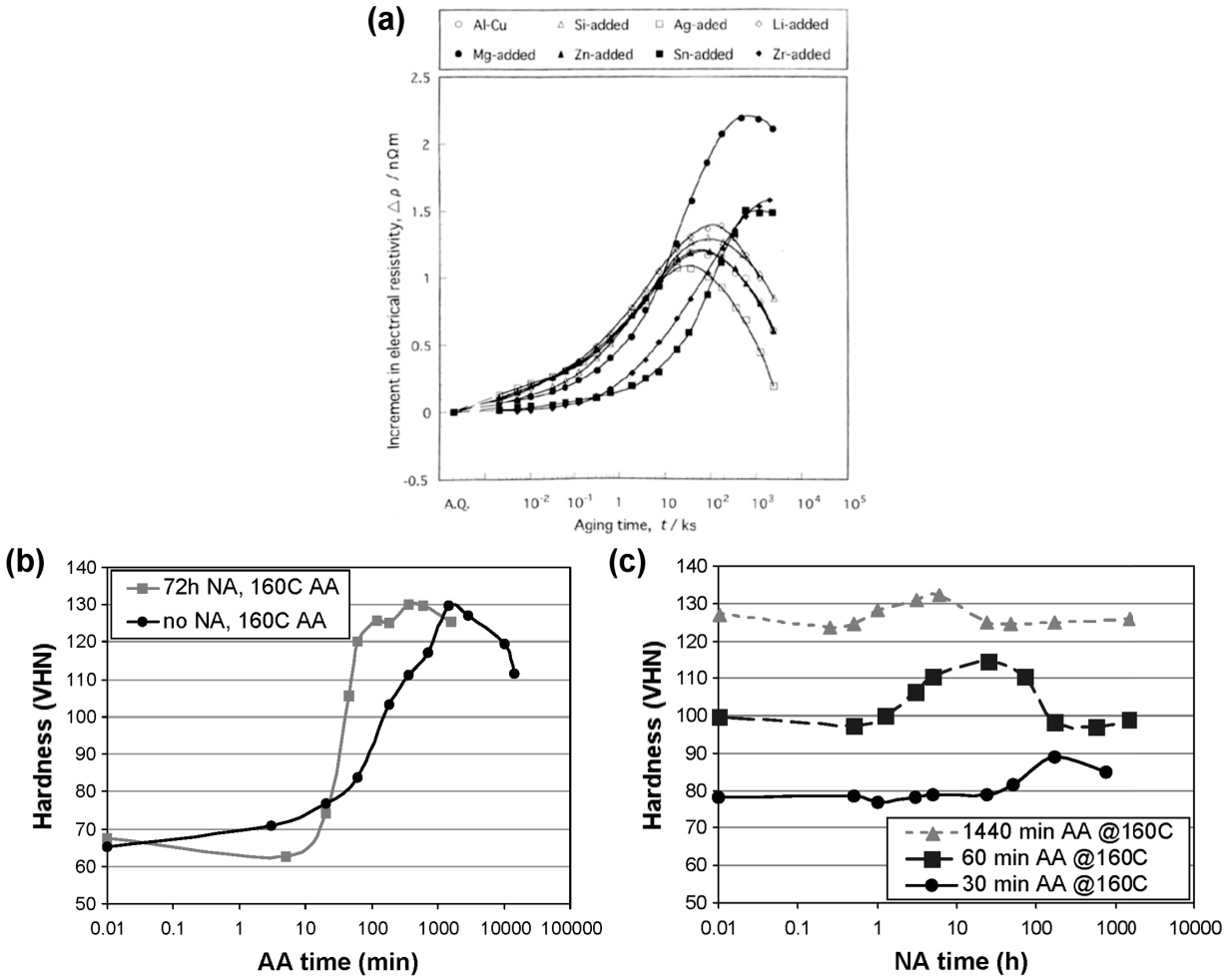

Figure 2.17: (a) Resistivity changes during aging at 278 K of Al-∼1.7at.% Cu with various MA elements [64]. Al-1.7at.% Cu-0.01at.% Sn alloy: (b) hardness curves with and without 72 hours NA before AA at 160 ℃ (c) effect of varying NA time on three different AA times. [65]

2.5.1.2 Cu and Ag in Al-Mg-Si

Sato et al. [7] performed hardness measurements on an Al-0.83%Mg-0.51%Si base alloy showing the negative effect of NPA on AA and a positive effect of preaging at 373 K comparing these aging treatments with direct AA, see figure 2.18(a). Further they studied alloys with additions of 0.27 % Cu or 0.38 % Ag, figure 2.18(b) and (c).

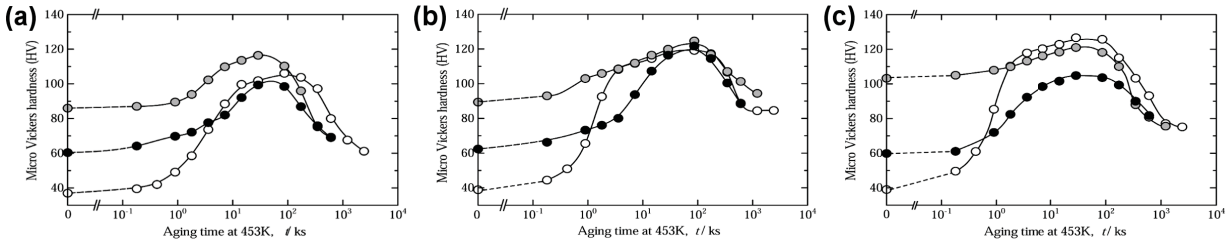

Figure 2.18: Al-0.83%Mg-0.51%Si alloy: hardness curves for AA at 453 K (a) base alloy, (b) 0.27 % Cu-added and (c) 0.38 % Ag-added. ○: no preaging, ●: preaged at 295 K for 24 hours, ●: preaged at 373 K for 24 hours [7]

As can be seen in figure 2.18(b), compared to direct AA Cu exhibits basically no negative and positive effects of preaging at RT and 373 K with regard to peak hardness. But compared to the base alloy, figure 2.18(a), the Cu-added alloy generally shows higher peak hardnesses for all three heat treatments [7]. Cu addition also noticable accelerates direct AA in comparison to the base alloy while for preaging at 295 K for 24 hours the hardening kinetics does not seem to change apart from the higher peak hardness. In general Cu influences the precipitation sequence of Al-Mg-Si alloys in the following way [67]:

Alloys with low Cu content:

α_{SSS} → GP zones (clusters) → β'' → β' + lath-shaped Q' → β (+Si)

Alloys with high Cu content (∼0.91 wt.%):

α_{SSS} → GP zones (clusters) → β'' → lath-shaped Q' → Q (+Si)

For direct AA the Ag-added alloy gives a slighly higher peak hardness than both other alloys. Regarding this last effect the preaging at RT and 373 K heat treatments represent pronounced adverse effects on AA. [7] Comparing the NPA conditions of the base and Ag-added alloys, Ag does not really change the peak hardness, but it accelerates the hardness increase at shorter times [7].

TEM investigations revealed that while for the base alloy NPA produces coarsened β'' precipitates, the Cu addition results in finer precipitates for all three heat treatments after AA at 453 K for 86.4 ks (24 hours). For single aging the Ag addition yields much finer and more densely distributed precipitates than the other alloys, but the two-step aging produces coarsened precipitates compared to direct AA. Precipitates in the Ag-sample directly artificial aged include Ag atoms besides Al, Si and Mg according to energy-dispersive X-ray spectroscopy (EDX) analysis [7].

2.5.1.3 Mg in Al-Cu and Al-Li-Cu

Figure 2.17(a) shows how during aging at 278 K after quenching Mg retards the initial resistivity increase of an Al-Cu alloy while in the subsequent (middle) stage it accelerates the increase which results in a greater resistivity maximum. Sato et al. [7] observed similar curves for various MA elements during aging at 273 K, RT and 323 K. They simulated the phase decomposition using a Monte Carlo simulation. Thus Mg addition clearly accelerates the nucleation of clusters and produces finer and more homogeneously distributed clusters of high density compared to the base alloy. Therefore the changed resistivity curve in the Mg-added Al-Cu alloys are due to the formation of finely distributed clusters which form retarded in the initial stage and show enhanced formation in the middle stage of aging. Also Mg-added Al-Li-Cu alloys show

an increased resistivity maximum and accelerated hardness increase. Monte Carlo simulation demonstrates a preferential trapping of vacancies by Mg atoms, although it has to be mentioned that such calculations always need uncertain input values such as an E_B. A reduced number of free vacancies is supposed to suppress Cu diffusion. In the following simulation stage, complex clusters containing Cu, Mg and vacancies, i.e. Cu/Mg/vacancy complex clusters, are formed. Hence it is interpreted that the Cu/Mg/vacancy clusters serve as effective nucleation sites for GP zones. This stays in contrast to the Cu/Sn/vacancy complex clusters of Al-Cu-Sn alloys which do not act as such sites for GP zones, see earlier in this section 2.5.1.1 [7].

2.5.1.4 Other Examples of MA Effects

Another example of a MA effect is the role of small Ag amounts in modifying precipitation and favoring greater hardening in Al alloys that contain Mg. Each system behaves in a different way. One example has already been mentioned in section 2.5.1.2. Another example are Al-Zn-Mg alloys in which Ag stimulates the existing aging process when aged at elevated temperatures. This effect is attributed to an increased temperature range over which GP zones are stable (mechanism 2, see earlier in this section). In Al-Mg binary alloys, Ag may cause precipitation in alloys in which it is normally absent (mechanism 6). In the Al-Cu-Mg system 0.1 at.%Ag promotes formation of three new and rather different precipitates depending on the Cu:Mg ratio. These are Ω (Cu:Mg ratio high, e.g. Al-4Cu-0.3Mg), X' (Cu:Mg medium, e.g. Al-2.5Cu-1.5Mg) and Z (Cu:Mg low, e.g. Al-1.5Cu-4.0Mg). After only 5 s of aging at 180 ℃ clusters form that lead to the nucleation of Ω (Al_2Cu) which grows along the $\{111\}_\alpha$ planes. Ω is relatively stable at elevated temperatures and promotes good creep resistance. Comparable little is known about properties promoted by X' or Z phases [8].

3 Materials Characterization

3.1 Optical Emission Spectrometry

For the compositional analysis of the measurement surfaces optical emission spectrometry (OES) (SPECTROMAXx from SPECTRO) was used to directly analyze all relevant elements simultaneously. For preparation the samples were milled off to obtain a smooth measurement surface. A standard (Al-MgSi 634) was used for calibration of the apparatus.

3.2 Inductively Coupled Plasma Mass Spectrometry

The amount of some MA elements used in this study could not be measured by OES (Ca, Ba, In and Ge). For these elements inductively coupled plasma (ICP) mass spectroscopy analyses were carried out. To apply a complementary method also the main study alloys, i.e. the content of the MA element, have been analyzed by ICP. A sample amount of about 50 mg was dissolved in concentrated HCl acid containing traces of HF and HNO_3. Afterward the solution was diluted with H_2O. The ICP measurement was performed with an external calibration, Yttrium and Rhenium were used as internal standards. On average an error of ± 8 % is estimated, except for the In-added alloy (± 28 %) and Ca-added alloy (± 15 %).

3.3 Hardness Measurement

Brinell hardness measurements of the type HBW 2.5/62.5/15 were performed using an EMCO-Test M4 unit. Sample dimensions were chosen large enough for at least four indents. To achieve statistically relevant hardness values at minimum three indents were averaged. Before the hardness measurements the samples were polished. After the AA heat treatment hardness tests were performed immediately after quenching to RT.

3.4 Atom Probe Tomography

For the atom probe tomography (APT) measurements needle-shaped specimens were prepared. Small rods with cross-section of 0.3×0.3 mm^2 were cut out of corresponding hardness test samples. A standard two-step method was used for the specimen preparation: after electropolishing the small rods with 10 % perchloric acid and 90 % methanol solution, 2 % perchloric acid in butoxyethanol was used as the second electrolyte. APT was performed on a LEAP^{TM} 4000 XHR atom probe at a temperature of 23.7 K. The atom probe was provided by the Electron Microscopy Center of the ETH Zurich (EMEZ). A pulse fraction of 20 %, a pulse rate of 200 kHz and an evaporation rate of 1 % were used. Furthermore the measurements were conducted under ultra-high vacuum ($<10^{-10}$ mbar). For the reconstruction procedure and analysis the software package IVAS 3.6.1^{TM} from Imago Scientific Instruments Corporation (Madison, WI, USA) was used. Always the same range-file was used, no peak-decomposition was applied.

4 Materials Selection, Fabrication Process and Heat Treatment

4.1 Choice of Alloy Compositions

On the basis of knowledge gained from the literature review in section 2 and the solubility data of various elements in pure Al and AA6061, see table 4.2, several MA elements were chosen to run pretests. These are: Li, Ca, Sr, Ba, Ag, Cd, In, Ge, Sn, Pb, Sb, Bi. It was decided to add the same concentration of each element, i.e. 500 at. ppm. Because of the results of the pretest measurements one trace element, Sn, was decided to be examined more closely in the main study.

4.1.1 Solubility of Used Microalloying Elements in Al-Mg-Si AA6061

Table 4.1 lists the alloy composition of the AA6061 reference bar at the measurement surface gained by OES.

Table 4.1: Elemental concentrations of the base alloy AA6061 in wt.% and at. ppm. Measured by OES.

Solute	Mg	Si	Cu	Fe	Mn	Cr	Ni	Zn	Ti	B
[wt.%]	0.80*	0.59*	0.221*	0.57*	0.109*	0.140*	0.0080*	0.056*	0.088*	0.0029
[at.ppm]	8933	5701	944	2770	538	731	37	232	499	73
Solute	Be	Bi	Ca	Cd	Ga	Na	Pb	Sn	V	Zr
[wt.%]	0.0005	0.0073	0.0019	0.0006	0.014	0.0014	0.0042	0.0053	0.0086	0.0003
[at.ppm]	15	9	13	1	54	17	6	12	46	1

Table 4.2 lists equilibrium solubility data of elements alloyed either in pure Al or the base alloy AA6061 used in this work. The data were obtained from FactSage calculations for the solution treatment temperature of 570 °C. The program version used was FactSage 6.2^{TM}. The applied databases are "FTlite – FACT light metal intermetallic compounds (2009)" and "FTlite – FACT light metal alloy solutions (2009)".

Table 4.2: Equilibrium solubility data of solutes in pure Al and in AA6061 calculated at 570 °C. For the FactSage 6.2^{TM} calculation all elements marked with an asterisk (*) from table 4.1 were used.

Solute		Li	Ca	Sr	Ba	Ag	Cd	In	Ge	Sn	Sb	Pb	Bi
Al	[at.ppm]	129600	0	0	0	195200	–	39	2068	209	0	0	1
AA6061	[at.ppm]	153800	0	2	21	119300	–	34	1299	79	0	0	1

4.1.2 Criteria for Used Microalloying Elements

This section only refers to the chosen MA elements. Most of these elements exhibit reasonably high calculated solute-vacancy binding energies E_B or enthalpies δH_B according to the data listed in table 2.2. All elements studied by Simonovic and Sluiter [55] (Li, Ca, Sr, Ag, Cd, In, Ge, Sn, Pb, Sb, Bi, see table 2.2) would show a diffusion behavior in Al dominated by Al-vacancy interchanges. Furthermore all used MA elements are larger than Al, many are even distincly larger (Ca, Sr, Ba, Cd, In, Sn, Pb, Sb, Bi), compare table 2.1. Some also exhibit an excess charge in Al host (Ge, Sn, Pb, Sb, Bi), also indicating an attractive interaction with vacancies.

The influence of Li addition on Al-Cu alloys is shown in figure 2.17. Although the E_B is calculated to even be repulsive by [55] the Al-Cu results arouse curiosity about the effect Li could have in AA6061.

Theories concerning the strong attractive interaction of Ca, Sr, Bi and Pb with vacancies have already been discussed in section 2.4.2.1. In spite of their theoretically calculated insolubility in Al, some pretests were carried out to varify this.

As discussed in section 2.5.1.2 and 2.5.1.4 Ag often seems to have an influence in changing the precipitation behavior and hardness evolution of Mg containing Al alloys which was the reason for testing it.

Viewing Ba, this element might be the largest element in an Al host considered in this work. Unfortunately no data for the real Ba size in Al was found. Ba neighbors Sr in the periodic table within the same column. So it can be presumed, that there might be some similarities in their behavior. Most interestingly Wolverton [48] calculated an extremely high E_B for Ba with -137.0 kJ/mol (table 2.2). Further the solubility calculations performed in this work let suggest that Ba is more soluble in AA6061 than in pure Al.

As Ge just lies between Si and Sn in the periodic table and Si for sure and Sn very probably influence the alloy behavior, it would be just reasonable for Ge to also show an effect. Its high solubility in both pure Al and AA6061 (table 4.2) may also play a role.

Cd, In and Sn already manifested their vacancy interactions in Al-Cu alloys including the appropriate theory, see section 2.5.1.1. So this study couldn't just leave them out.

4.2 Alloy Fabrication Process

The alloying process of the specimen material is based upon the addition of the in section 4.1 selected and characterized MA elements to the industrial alloy AA6061 (table 4.1).

Table 4.3 shows all casted alloys including the intended and achieved MA element concentrations (c_i and c_a) at the test region as well as the weighting of AA6061 m_{AA6061} and the MA elements m_{MA}. Further the resolving time t_{res} is listed. Note that consecutively only the results of c_a obtained by OES are used.

To take into account already contained amounts of the MA element in AA6061 the existing amount was subtracted from the sought composition and the result was used for calculating the weighting m_{MA}. To avoid loss of some tiny pieces the weighted mass was enwraped into a small piece of Al foil.

Table 4.3: Intended (c_i) and achieved (c_a) concentrations of MA elements added to the alloy AA6061 given in wt.% and at. ppm. Purity values lower than 100 % mean that an Al-MA element master alloy was used instead of the pure MA element. The term 'P' stand for pretest alloys and 'MSt' for main study alloys. Concentration analyses were performed either by OES[a], ICP[b] or both. c_a of Ca should be treated with caution (measurement problems).

MA el.	c_i	c_i	c_a	c_a	m_{AA6061}	Purity	m_{MA}	t_{res}	Series
	at.ppm$_i$	wt.%$_i$	at.ppm$_a$	wt.%$_a$	[g]	[%]	[g]	[s]	
Li	500	0.0128	191[a]	0.0049[a]	1402.18	100	0.229	–	P
Ca	500	0.0730	402[b]	0.0594[b]	1404.79	6	17.092	5	P
Sr	500	0.1616	353[a]	0.114[a]	1396.27	10	22.564	5	P
Ba	500	0.2061	404[b]	0.2047[b]	1406.47	8	44.392	5	P
Ag	500	0.1985	564[a]	0.224[a]	1399.95	100	2.780	45	P
Cd	500	0.2061	411[a]	0.17[a]	1401.31	100	2.888	15	P
In	500	0.2111	519[b]	0.2193[b]	351.18	100	0.741	15	P
Ge	500	0.1337	269[b]	0.0719[b]	1403.49	100	1.876	30	P
Sn	500	0.2184	453[a]	0.198[a]	1401.37	100	2.961	15	P
Sb	500	0.2238	51[a]	0.023[a]	1398.26	100	3.130	15	P
Pb	500	0.3742	159[a]	0.121[a]	1403.05	100	5.250	15	P
Bi	500	0.3775	459[a]	0.352[a]	1405.58	100	5.306	15	P
Sn	500	0.2184	431[a], 503[b]	0.188[a], 0.2194[b]	1398.66	100	2.980	15	MSt
Sn	250	0.1093	195[a], 260[b]	0.085[a], 0.1136[b]	1388.60	100	1.444	15	MSt
Sn	100	0.0437	69[a], 95[b]	0.030[a], 0.0146[b]	1402.36	100	0.539	15	MSt
Sn	50	0.02186	37[a], 41[b]	0.016[a], 0.0177[b]	1398.25	100	0.537	15	MSt

Figure 4.1(a) shows the casting assembly. To prohibit a contamination of the alloy during the melting process a special coating was applied to the ceramic crucible, the casting mold and the spattle used for alloying. First the weighted AA6061 bars were melted to obtain an alloying temperature of about 720 ℃. During the entire alloying process argon was blown on the melt surface.

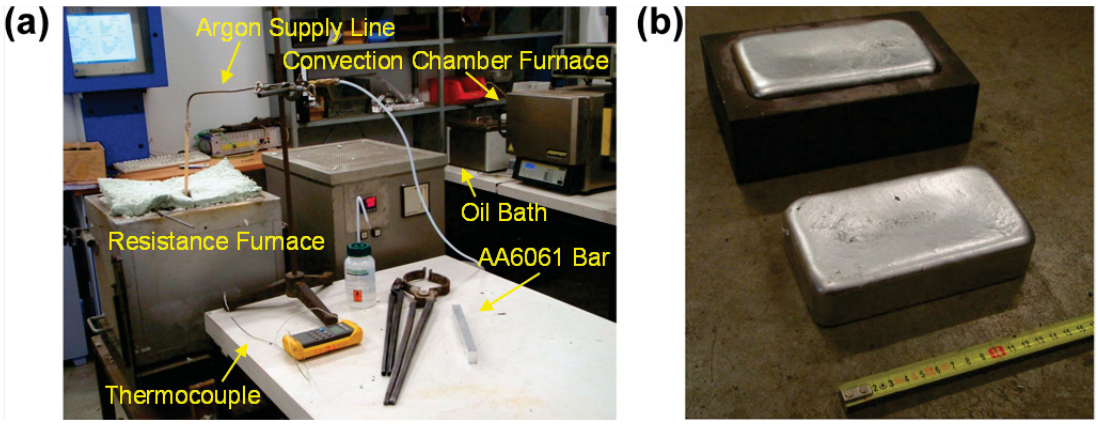

Figure 4.1: Casting assembly (a) resistance furnace, argon supply line, convection chamber furnace, temperature measuring device, bar of AA6061, oil bath (b) casted bar besides the casting mold

As pure Li quickly oxidizes in ambient environment and generally has to be handled carefully, the Li weight was chosen with 0.229 g instead of the calculated mass of ∼0.179 g necessary for 500 at. ppm. To prohibit a floating of the MA element during alloying a carbon rod with a hole at the end was used as a diving bell. During the resolution time it is believed that a part of the Li mass has been lost due to oxidation which might have caused the low achieved Li concentration c_a of 191 at. ppm.

Alloying was carried out by first skimming the melt surface with the warmed spattle and then throwing the Al foil package into the melt. If necessary, mainly for lighter elements, the package needed to be submersed with the spattle and the alloy to be stirred. During the in table 4.3 listed resolving time of the MA element the alloy temperature was controlled to ideally obtain a casting temperature between 715 and 720 °C. After the subsequent argon stirring (3 till 4 minutes) the alloy was skimmed again. At last the cast was carried out by pouring the melt into the 250 °C warm casting mold, see figure 4.1(b). The dimensions of the cooled casted bar for all alloys, with exception of the In-added and In-reference alloys, were $157 \times 88 \times 33$ mm^3, see figure 4.2(a). The In-added and In-reference bars, for which another, smaller casting mold was used, had the following dimensions: $98 \times 78 \times 10$ mm^3, figure 4.2(b).

4.3 Sample Preparation

To compensate segregations the casted bars were subjected to a homogenization process in a convection chamber furnace (Nabertherm N15/65 SHA, figure 4.3(b)) for 24 hours. Starting at RT the temperature increase to 500 °C lasted two hours. After 8 hours at 500 °C the furnace heated to 570 °C in two hours where the bars were homogenized for 12 hours.

For the pretests the homogenized bars were milled off on the bottom side (2 mm) and using this

surface as reference a plate of 4 mm thickness was produced, see figure 4.2(a). A hardness test in T6 condition on the upper side of the plate, i.e. the measurement surface lying 6 mm from the original bar bottom, showed homogeneous behavior along the broadside and long side of the plate. Figure 4.2 shows how the samples were cut out of these plates. A sample dimension of $17 \times 8 \times 4$ mm^3 was chosen for all pretest alloys except the In-added and In-reference alloys ($15 \times 8 \times 4$ mm^3). The middle part of the plates were used for a compositional analysis by OES.

Due to the smaller In-added and In-reference bars, figure 4.2(b), only 1 mm was milled off the bottom side. An OES analysis showed a satisfactory composition. Therefore, contrary to the other pretest alloys, this analyzed bottom side was used as measurement surface.

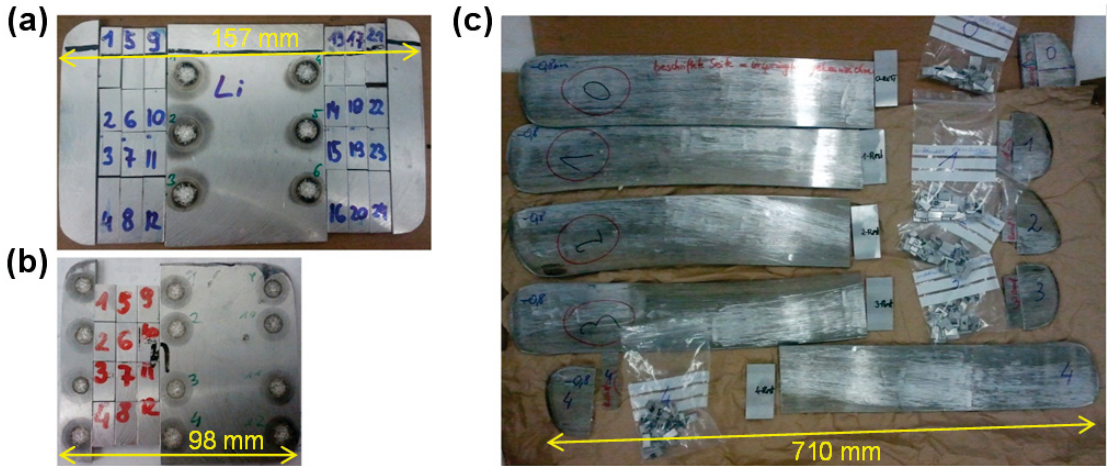

Figure 4.2: (a) Example of a milled pretest plate including the prepared samples and the area analyzed by OES (b) smaller pretest plate of the In-added and In-reference alloys (c) rolled main study sheets and cutted sample areas

For the main study additionally a rolling process was performed resulting in the sheets of figure 4.2(c). Prior to that a rough estimation of the achieved composition was performed by analyzing the milled bottom side of the bars by OES. The bars were also milled off on the upper side and a bit on the side surfaces to get 20 millimeter high plates. The subsequent rolling process involved the reduction stages: 20 mm – 18.8 mm – 15.65 mm – 11.6 mm – 7.7 mm – 4.2 mm. Before the first roll pass the plates were heated for 1.5 hours at 550 °C, in between two passes the samples were reheated at 550 °C for 15 minutes. 0.8 mm were milled off from the bottom side of the rolled plates and samples of $17 \times 10 \times 3.4$ mm^3 were produced. Figure 4.2(c) shows the areas of the rolled plates where the samples are located. All samples were instantly engraved on the back side for labelling.

Table 4.4 lists the compositions of all fabricated alloys as measured by OES or ICP. The full composition of the pretest reference alloy AA6061 has already been listed in table 4.1.

Table 4.4: Composition of fabricated alloys. Al is in balance. Elements marked with an asterisk (*) were measured with an ICP analysis instead of an OES. The term 'P' stands for pretest alloys, 'MSt' for main study alloys.

AA6061	Si	Fe	Cu	Mn	Mg	Cr	Zn	Ti	MA el.	**Series**
	[wt.%]	[wt.%]	[wt.%]	[wt.%]	[wt.%]	[wt.%]	[wt.%]	[wt.%]	[wt.%]	
+Li	0.64	0.467	0.226	0.111	0.83	0.146	0.061	0.079	0.0049	P
+Ca	0.62	0.58	0.224	0.107	0.78	0.141	0.056	0.084	0.0594*	P
+Sr	0.63	0.57	0.219	0.109	0.79	0.137	0.057	0.077	0.114	P
+Ba	0.62	0.57	0.216	0.107	0.76	0.136	0.056	0.082	0.2047*	P
+Ag	0.63	0.469	0.228	0.111	0.82	0.148	0.060	0.076	0.224	P
+Cd	0.61	0.57	0.222	0.109	0.79	0.142	0.057	0.088	0.170	P
+Ge	0.63	0.58	0.228	0.110	0.78	0.141	0.057	0.084	0.0719*	P
+Sn	0.61	0.58	0.222	0.110	0.79	0.141	0.057	0.082	0.198	P
+Pb	0.61	0.58	0.221	0.110	0.80	0.139	0.058	0.082	0.121	P
+Sb	0.63	0.51	0.226	0.110	0.83	0.148	0.060	0.079	0.023	P
+Bi	0.63	0.59	0.228	0.111	0.81	0.139	0.058	0.089	0.352	P
In-Ref	0.66	0.555	0.234	0.112	0.85	0.150	0.062	0.079		P
+In	0.67	0.55	0.238	0.110	0.84	0.145	0.060	0.076	0.2193*	P
Sn-Ref	0.62	0.485	0.220	0.111	0.81	0.146	0.059	0.081	0.0025, 0.00123*	MSt
+Sn	0.63	0.59	0.232	0.111	0.82	0.147	0.059	0.079	0.188, 0.2194*	MSt
+Sn	0.60	0.484	0.222	0.109	0.80	0.149	0.058	0.086	0.085, 0.1136*	MSt
+Sn	0.58	0.482	0.213	0.110	0.79	0.147	0.057	0.088	0.030, 0.0146*	MSt
+Sn	0.64	0.56	0.225	0.112	0.82	0.145	0.060	0.075	0.016, 0.0177*	MSt

4.4 Heat Treatment

Each sample was solution heat treated in a convection chamber furnace (Nabertherm N15/65 SHA, figure 4.3(b)) at 570 °C for 20 minutes and then quenched into water at RT. For 170 °C and longer AA times AA was performed in an oil bath with a maximum working temperature of 200 °C (LAUDA ECO E 25), see figure 4.3(a). All shorter AA times of up to 15 minutes were carried out in a low melting alloy as high-performance heat transfer medium ($Bi_{57}Sn_{43}$) that was put into another oil bath which is able to operate at temperatures up to 300 °C (LAUDA Proline P 26, figure 4.3(b)). AA treatments of longer than 15 minutes at 210 and 250 °C were also performed in this oil bath, but without the low melting alloy.

During NA and the NPA period between solution heat treatment and AA the samples were kept in a peltier-cooled incubator IPP from Memmert at 25 °C.

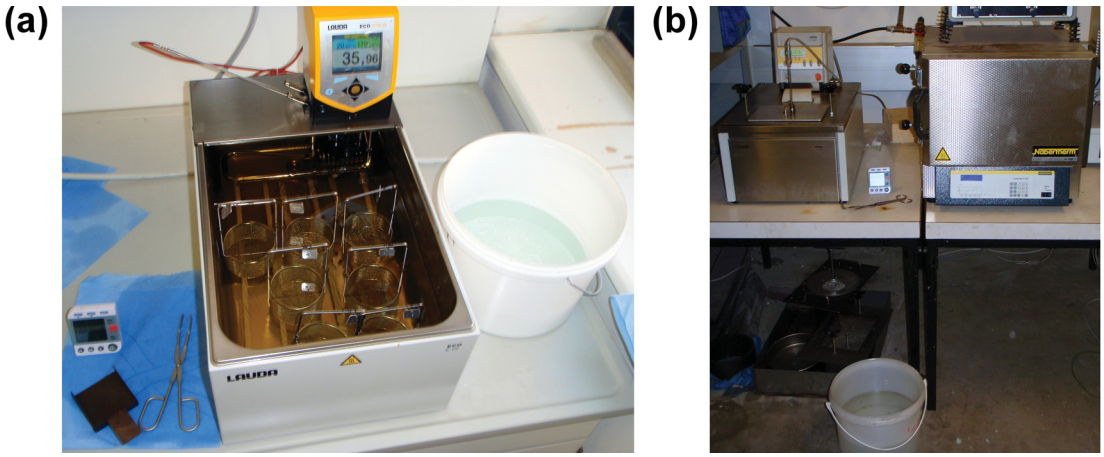

Figure 4.3: (a) Oil bath for AA for longer times at 170 °C, (b) oil bath for AA temperatures above 200 °C and convection chamber furnace. For shorter AA times at 170, 210 and 250 °C a low melting alloy was inserted in the oil bath.

5 Results

5.1 Pretests

Figure 5.1(a) shows the hardness development during storage at RT, i.e. 25 ℃, after quenching.

For the reference alloy without a MA element a hardness of ∼46 HBW is measured directly after quenching. Only a slight hardness increase can be seen after 4.8 ks (80 minutes) of NA. This is followed by a nearly continuous logarithmic hardness rise until the maximum value of ∼73 HBW, measured after 1.2×10^6 s (14 days), is reached. While many studied alloys follow comparable hardening kinetics as the reference alloy, some show distinct differences.

Most remarkably the Sn-added alloy containing 453 at. ppm Sn stays at about the same hardness of ∼46 HBW, as already measured directly after the quench, for nearly two weeks. Afterward a slight hardness increase seems to start which results in ∼49 HBW after 2.6×10^6 s (30 days).

A similar behavior is measured for In addition, as pictured in figure 5.1(b). The hardness increase seems to start at around 1.2×10^6 s of NA. This is followed by a fast rise in hardness which yields ∼67 HBW after 2.6×10^6 s of NA. Afterward the hardening kinetics seems to slow down.

Further also the Cd-added alloy containing 411 at. ppm Cd exhibits a delayed hardness increase. Starting at a slightly higher hardness after quenching compared to the reference, it shows a increase in hardness after about 28.8 ks (8 hours) of NA and reaches a maximum value of ∼70 HBW after 2.6×10^6 s of NA.

The elements Ca, Sr, Ba and Ge seem to follow a similar hardening curve after slight differences at the beginning of the RT storage. Note that for the sake of brevity also the name of the MA element alone is used instead of "MA element-added alloy". They show a lower hardness than the reference but no strongly reduced kinetics. From 28.8 ks till 1.2×10^6 s of NA the difference to the reference is ∼4–6 HBW with a maximum hardness of ∼66–68 HBW after 14 days. It cannot be said for sure if these differences can be taken as significant.

The MA elements Pb and Bi just exhibit a slight deviation from the reference after 1.2×10^6 s of NA. Here Pb reaches a maximum of ∼69 HBW and Bi of ∼71 HBW.

Sb can be said to not really influence NA compared to the reference.

Li seems to have a small promoting influence on the hardness evolution at the beginning of NA, but the effect is below the significance level. Like Li, Ag is also showing a small positive effect on the hardness development.

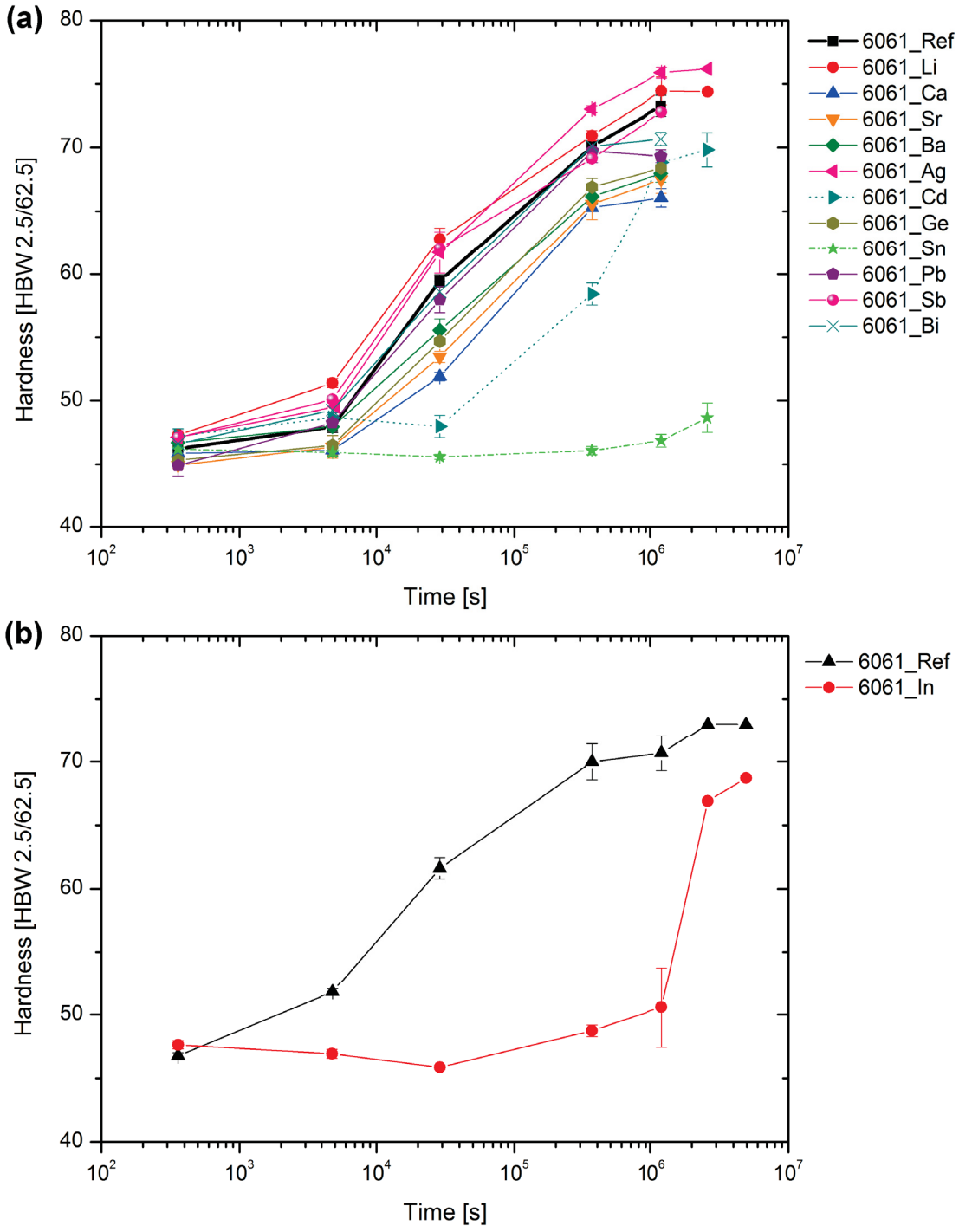

Figure 5.1: Hardness evolution during NA of microalloyed AA6061 alloys at 25 °C (a) Reference, Li, Ca, Sr, Ba, Ag, Cd, Ge, Sn, Pb, Sb, Bi; (b) Reference of In, In

As the hardness of Cd starts to rise after ∼28.8 ks of NPA, it was thought reasonable to run some AA tests after this NA time. The results obtained for AA at 170 °C are displayed in figure

5.2. Like during NA, again Cd, In and Sn show the most pronounced hardness deviations from the reference.

The Sn-added alloy starts from the low NA value of ∼46 HBW. After the technologically relevant AA time of 1.8 ks (30 minutes) it reaches ∼62 HBW, i.e. ∼10 HBW lower than the reference. In the following the reference and Sn-added alloy accelerate their hardening kinetics which for both yields a continuous logarithmic hardening until 43.2 ks (12 hours) of AA. The faster hardening kinetics of the Sn-added alloy results in about the same hardness as the reference alloy after 10.8 ks (3 hours), i.e. ∼91-92 HBW. This hardness increase further yields ∼111 HBW after 43.2 ks of AA where it exceeds the reference by ∼5 HBW.

The behavior of the In-added alloy in figure 5.2(b) is comparable to the Sn-added alloy described just earlier. Following the 1.8 ks value of ∼62 HBW, i.e. ∼7 HBW below the reference, the hardness after 10.8 ks (∼99 HBW) exceeds the reference by ∼16 HBW. After 43.2 ks of AA the kinetics seems to have slowed down yielding ∼110 HBW compared to the reference with ∼98 HBW.

Compared to all other alloys from the pretest series, Cd shows by far the fastest hardening kinetics in figure 5.2(a). In contrast to Sn and In, the Cd-added alloy already exceeds the reference after 1.8 ks of AA by ∼4 HBW. This difference increases during longer AA time. The largest deviation of ∼15 HBW is perceived after 10.8 ks with Cd exhibiting ∼106 HBW. Like observed for the In-added alloy, the kinetics of Cd seems to slow down afterward resulting in a peak hardness of ∼117 HBW after 43.2 ks of AA which is ∼11 HBW above the reference.

The only other element showing slightly different hardening kinetics than the reference seems to be Ge. Ge starts from ∼55 HBW, reaches the reference value of ∼72 HBW after 1.8 ks of AA and then exceeds the reference values, though not much with ∼109 HBW after 43.2 ks.

Like during NA, Ca, Sr, Ba and Pb exhibit similar hardening kinetics as the reference, but range at lower hardnesses.

Li as well as Bi seem to totally follow the reference trajectory. Until 10.8 ks Ag and Sb resemble Li and Bi. At 43.2 ks they seem to reach a higher maximum value of ∼109–110 HBW but this effect remains below the significance level.

As can be seen from figure 5.3 after 1.2×10^6 s (14 days) of NPA a heat treatment at 170 °C exhibits a notably changed hardness evolution of all studies alloys.

Sn and In now exhibit the most deviating hardening kinetics compared to the reference while all other alloys, with exception of Ag and partly Cd, more or less follow the kinetics of the reference.

The Sn-added alloy starts from the lowest value of ∼47 HBW after 1.2×10^6 s of NPA. Like after

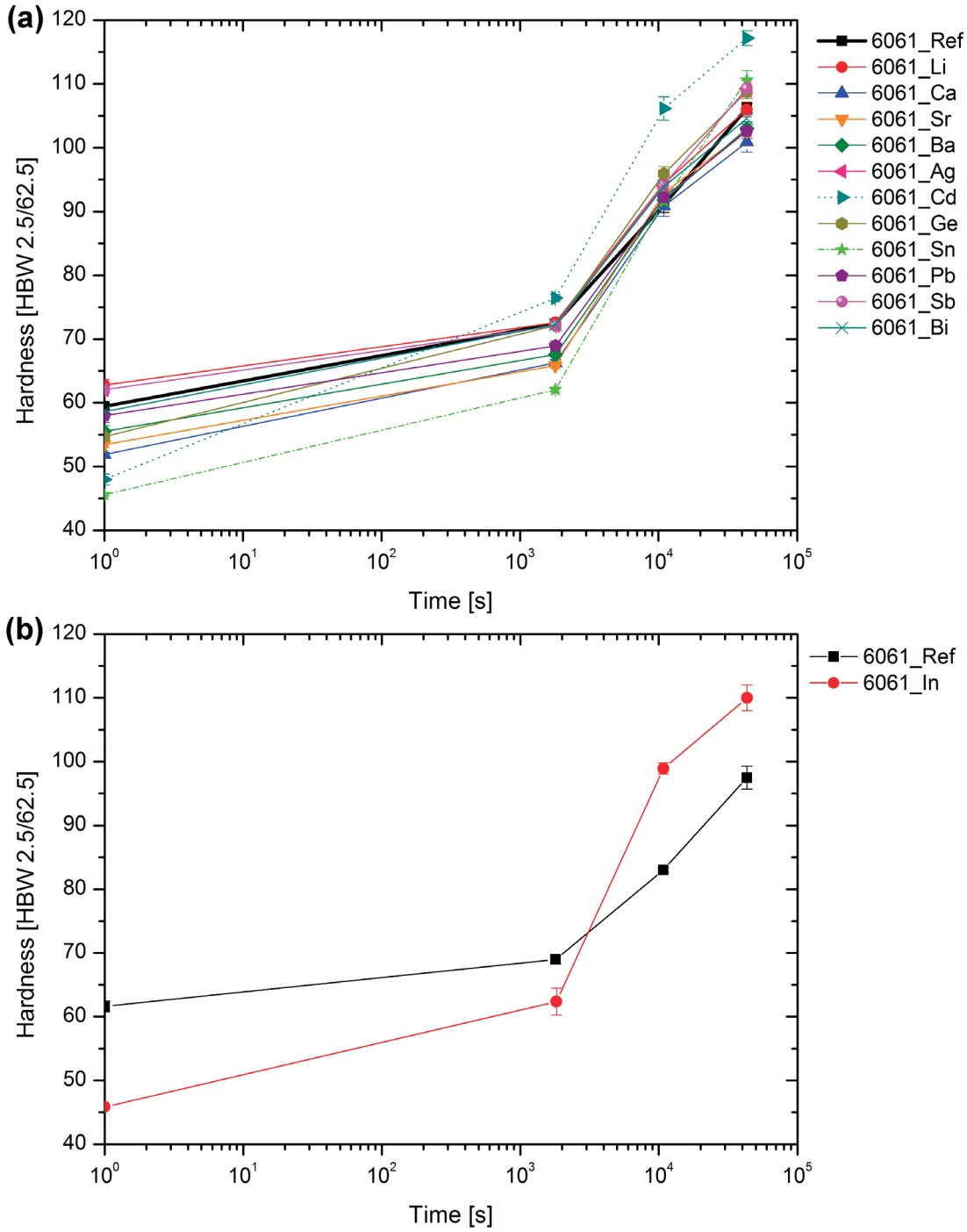

Figure 5.2: Hardness curves of microalloyed AA6061 alloys with 28.8 ks of intermediate storage at 25 °C during AA at 170 °C (a) Reference, Li, Ca, Sr, Ba, Ag, Cd, Ge, Sn, Pb, Sb, Bi; (b) Reference of In, In

28.8 ks of NPA its hardness after 1.8 ks of AA remains under the reference. Here the reference has ∼74 HBW while the Sn-added alloy shows ∼60 HBW. At 10.8 ks of AA the maximum positive divergence to the reference occurs with ∼98 HBW to ∼84 HBW. The hardening kinetics seems to slow down until after 43.2 ks of AA Sn reaches ∼112 HBW which is still ∼10 HBW higher than the reference.

The kinetics of the In-added alloy (figure 5.3(b)) seems to resemble the behavior of the Sn-added alloy after 1.2×10^6 s of NPA in principle. Although the AA kinetics of the Sn-added alloy rises with longer NPA time, the AA kinetics of the In-added alloy seems to slightly slow down compared to the reference. As has already been mentioned before, In seems to start hardening at about after 1.2×10^6 s of NPA, i.e. having ∼51 HBW. This might play a role for the subsequent AA. Starting from this value, the hardness after 1.8 ks of AA yields ∼63 HBW while the reference still shows its initial value of ∼71 HBW. During the following accelerated hardness increase In shows about 6 HBW higher hardnesses than the reference with ∼88 HBW after 10.8 ks and a maximum hardness of ∼108 HBW after 43.2 ks of AA.

The behavior of Cd during AA completely changes after 1.2×10^6 s of NPA compared to 28.8 ks of NPA. As the Cd-alloy seems to be nearly fully natural aged after 1.2×10^6 s, i.e. exhibiting a hardness of ∼69 HBW, its hardness after 1.8 ks of AA already only slightly exceeds the reference anymore. In the following Cd remains harder than the reference with a rising difference which reaches ∼110 HBW after 43.2 ks of AA, being ∼8 HBW harder than the reference.

The Ag-added alloy shows a nearly constant hardness of ∼76 HBW for the first half an hour of AA (1.8 ks) at 170 °C as also does the reference with ∼74 HBW. But following this Ag hardens significantly faster than the reference with ∼98 HBW after 10.8 ks and ∼110 HBW after 43.2 ks of AA.

The hardness difference of the reference to Ca, Sr and Ba remains nearly constant at the same value as reached after 1.2×10^6 s of NA with always being ∼4–7 HBW lower than the reference.

Li and Sb seem to harden insignificantly faster than the reference, while Pb faintly remains on a lower hardness level and for Bi and Ge no real deviation from the reference can be revealed.

To get an impression, if the hardness development during AA at 170 °C changes notably after longer NPA times than 1.2×10^6 s, for Sn and Cd also a test measurement after 2.6×10^6 s (30 days) of NPA was performed. Figure 5.4 shows no change for the Sn-added alloy, i.e. ∼98 HBW after 10.8 ks of AA. The Cd-added alloy reveals a slighly lower hardness of ∼87 HBW after 10.8 ks of AA compared to ∼89 HBW after 1.2×10^6 s of NPA and 10.8 ks of AA.

5.2 Main Study

5.2.1 Hardness measurement

Figure 5.5 shows the evolution of the hardness during NA of the rolled main study samples. The curve of the rolled reference mostly resembles the one of the pretest reference, compare

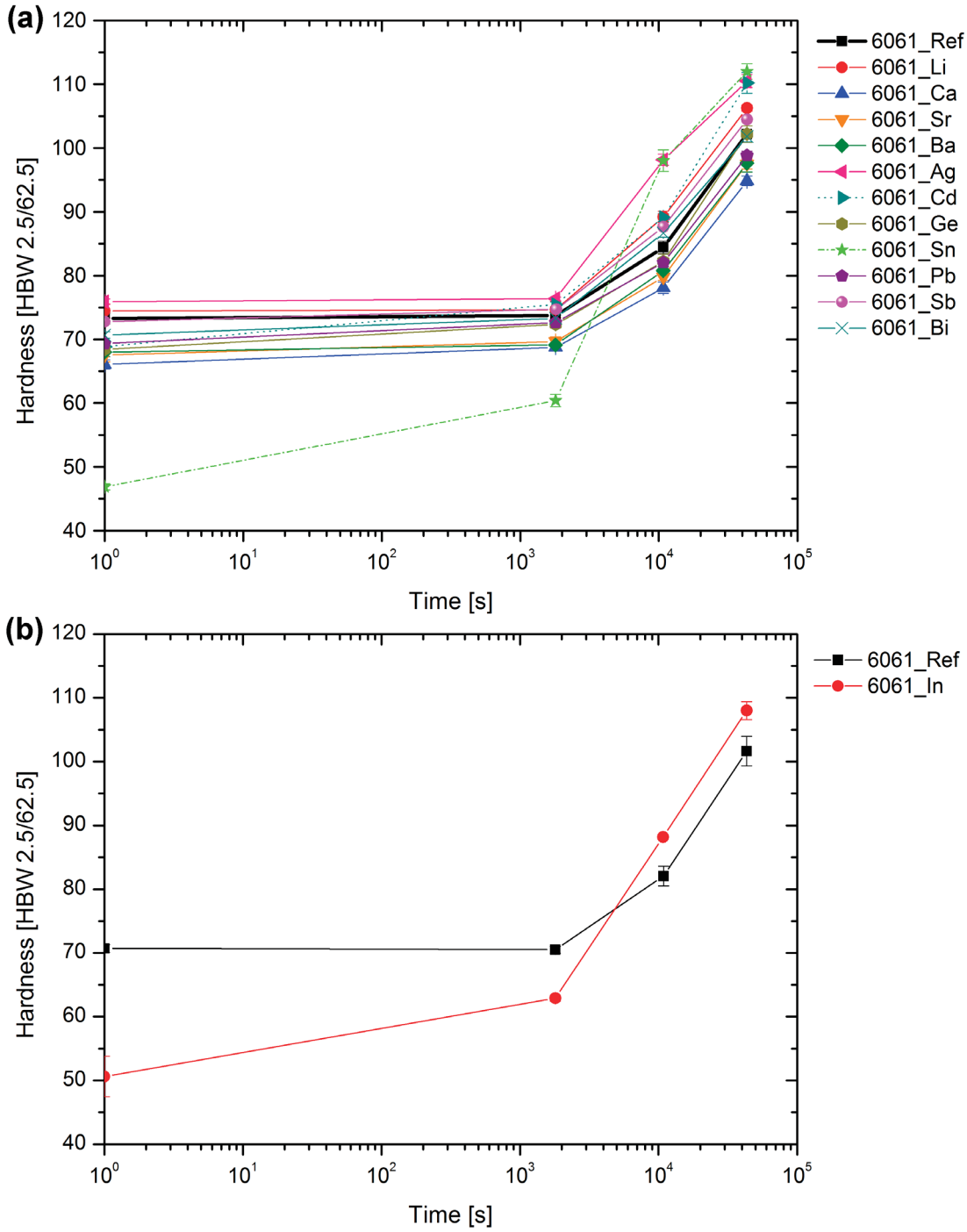

Figure 5.3: Hardness curves of microalloyed AA6061 alloys with 1.2×10^6 s intermediate storage at 25 °C during AA at 170 °C (a) Reference, Li, Ca, Sr, Ba, Ag, Cd, Ge, Sn, Pb, Sb, Bi; (b) Reference of In, In

to figure 5.1(a). Also the trajectory of the rolled Sn-added alloy containing ∼431 at. ppm Sn is more or less the same as the one of the pretest sample with a comparable amount of Sn.

It has to be noted that the small Sn amounts studied caused no problems during the rolling process. As large amounts of Sn often lead to cracks during rolling this for sure can be important for possible future applications.

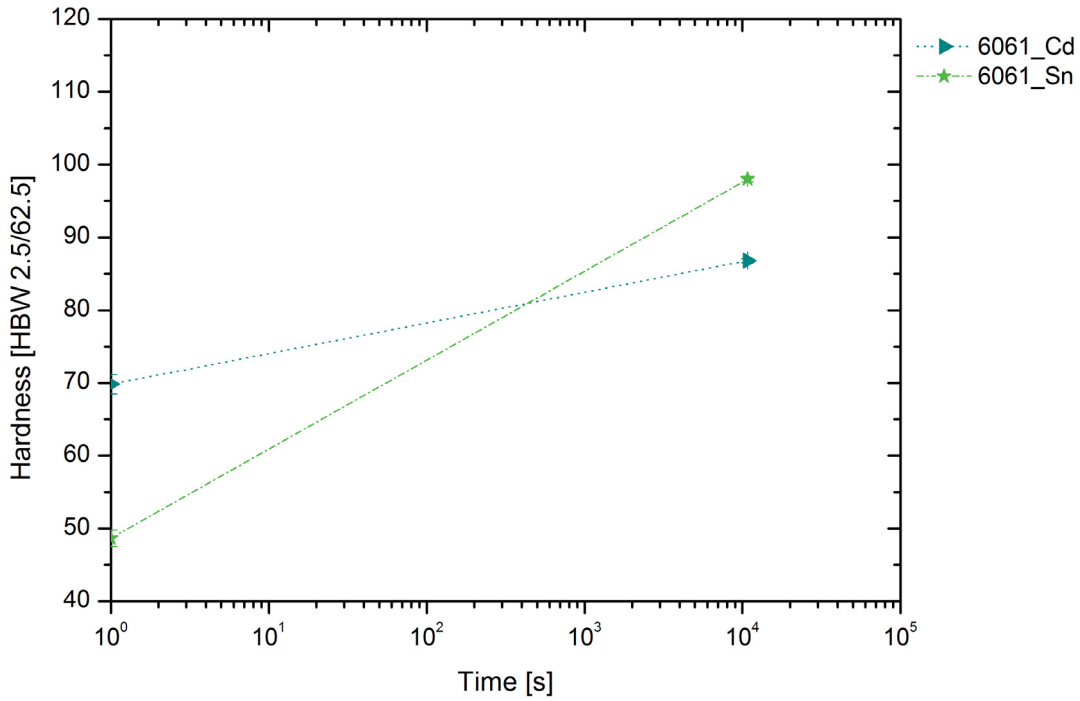

Figure 5.4: Hardness curves of microalloyed AA6061 alloys with 2.6×10^6 s of intermediate storage at 25 °C during AA at 170 °C; Cd, Sn

In the as-quenched state the Sn-added alloys seem too vary in their hardness from the reference alloy which is ∼46 HBW hard, but the effect remains below the significance level. During the first NA period all Sn containing alloys more or less stay at their as-quenched hardness value.

Of all Sn-added alloys the one with the smallest Sn content of ∼37 at. ppm shows by far fastest NA kinetics after remaining nearly 100.8 ks (28 hours) at the as-quenched hardness. Within the next days the hardness quickly rises to a value of ∼67 HBW after 3.45×10^5 s (4 days). Then the hardening seems to slow down resulting in ∼72 HBW after 1.2×10^6 s of NA which is also comparable with the reference value after the same NA time. Like the reference, the hardness of the ∼37 at. ppm Sn alloy does not change much anymore after longer NA times.

The ∼69 at. ppm Sn alloy is the second one starting its hardness increase. Between 3.45×10^5 s and 1.2×10^6 s of NA it hardens from ∼46 HBW to ∼50 HBW. During the subsequent 25 days a rapid logarithmic hardening occurs until ∼67 HBW after 3.4×10^6 s (39 days) are reached. In the following the hardness increase already seems to slow down, i.e. after 5.2×10^6 s (60 days) it reaches ∼68 HBW compared to a reference value of ∼73 HBW.

Both, the ∼195 at. ppm and ∼431 at. ppm Sn alloys also seem to start their hardening between 3.45×10^5 s and 1.2×10^6 s of NA, but at lower rate. After 2.6×10^6 s of NA both show the same hardness of ∼49 HBW. This is followed by a splitting of the NA kinetics which means that the alloy containing ∼431 at. ppm Sn hardens slighly faster with ∼62 HBW after a NA

period of 5.2×10^6 s. At the same time the ∼195 at. ppm Sn alloy only reaches ∼57 HBW.

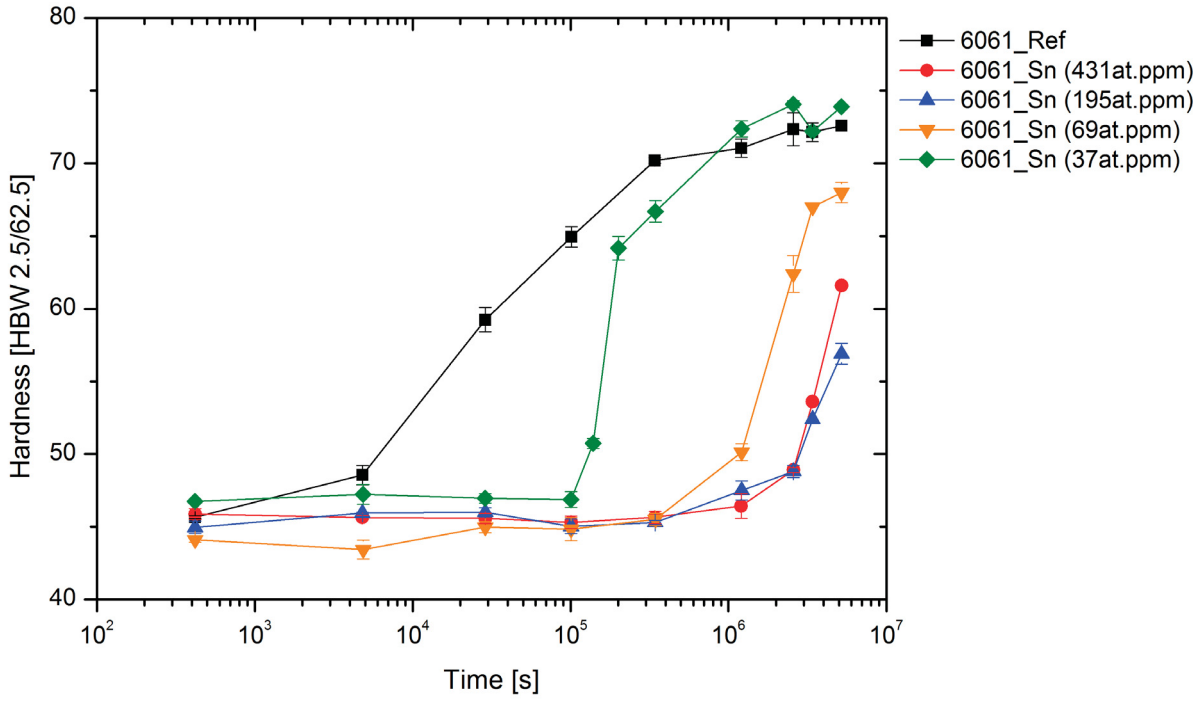

Figure 5.5: Hardness evolution during NA of Sn-added AA6061 alloys at 25 °C

As before for the pretest alloys, also the main study alloys were AA at 170 °C after 28.8 ks (8 hours) of NPA, see figure 5.6. Here the starting value of all Sn-added alloys is still about their as-quenched hardness.

In comparison to the other naturally pre-aged Sn alloys the ∼37 at. ppm Sn alloy starts from the highest NA value of ∼47 HBW. Compared to all other alloys, it shows by far the fastest hardening kinetics. During AA it already exceeds the reference alloy by ∼13 HBW after 1.8 ks of AA at 170 °C, i.e. ∼84 HBW compared to ∼71 HBW. This trend carries on during the subsequent AA. After AA for 10.8 ks the alloy shows a hardness of ∼110 HBW and after 43.2 ks ∼118 HBW were found (the largest hardnesses value found in this work), while the reference shows values of ∼91 HBW and ∼104 HBW. In general the kinetics seems to slow down after 10.8 ks.

The other Sn-added alloys containing ∼431, ∼195 and ∼69 at. ppm Sn exhibit nearly similar AA kinetics. Their hardness increase during the first half an hour (1.8 ks) of AA results in $\sim 60 \pm 1$ HBW which still lies under the reference. But until 10.8 ks of AA all three alloys exceed the reference. The ∼431 at. ppm alloy here splits from the other two with a hardness of ∼94 HBW, i.e. about 6 HWB lower than the others. While the kinetics of the ∼195 and ∼69 at. ppm Sn alloys seems to slow down after 10.8 ks the ∼431 at. ppm Sn alloy continuous with a steady logarithmic hardening. After 43.2 ks of AA the three alloys again exhibit nearly

the same hardness of ∼111–112 HBW.

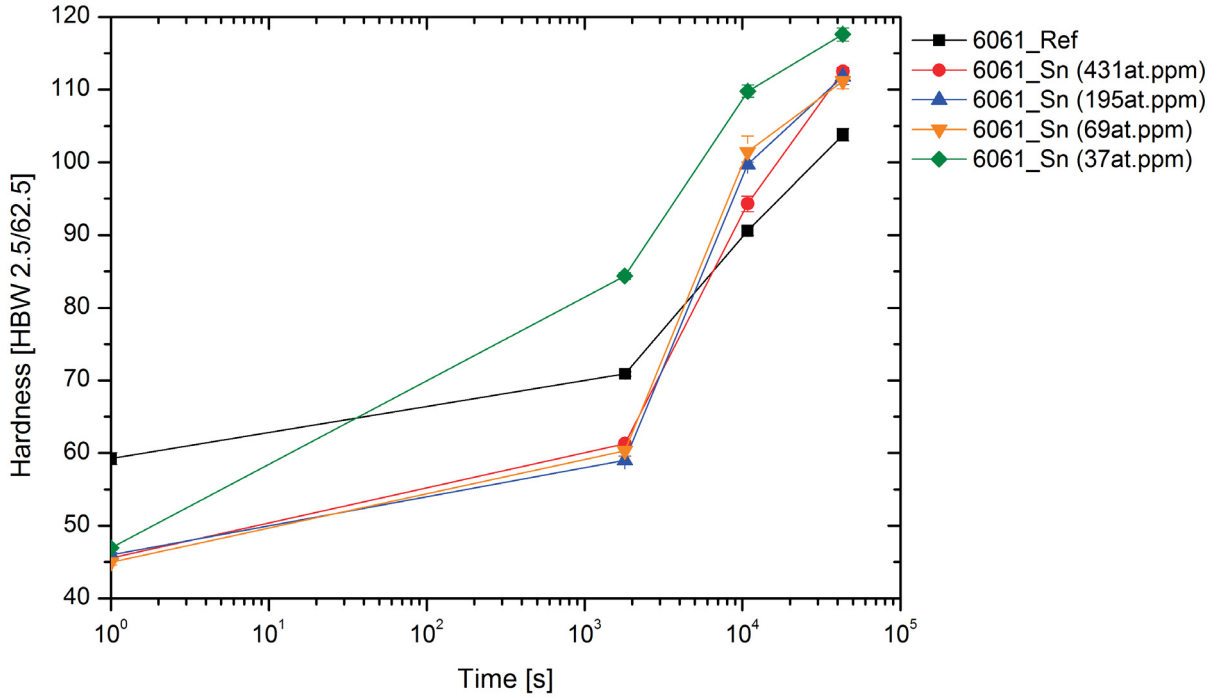

Figure 5.6: Hardness evolution of Sn-added AA6061 alloys with 28.8 ks of intermediate storage at 25 °C during AA at 170 °C

Figure 5.7 shows how four days (3.45×10^5 s) before AA at 170 °C completely changes the behavior of the ∼37 at. ppm Sn alloy, i.e. its kinetics is more similar to the one of the reference. Its initial hardness of ∼67 HBW lies ∼3 HBW below the reference, after 1.8 ks of AA the two alloys equal in their hardness (∼73 HBW). Thereafter ∼37 at. ppm Sn slightly exceeds the reference by ∼3–4 HBW after 10.8 and 43.2 ks of AA yielding ∼92 HBW after 10.8 ks and resulting in a maximum of ∼105 HBW after 43.2 ks of AA.

The other alloys containing ∼431, ∼195 and ∼69 at. ppm Sn show nearly similar kinetics. After approximately the same starting point at ∼46 HBW, the hardness after 1.8 ks of AA is ∼61–62 HBW. A slight splitting occurs after 10.8 ks of AA, where all three alloys are noticably harder than the reference, i.e. by ∼8–13 HBW. Hereafter the hardest one, ∼431 at. ppm Sn, exhibits a small slowdown of its AA kinetics. The final value of all three alloys after 43.2 ks of AA still is ∼9–11 HBW higher than the reference which shows ∼102 HBW.

After 1.2×10^6 s (14 days) storage at RT the reference alloy AA6061 reaches a hardness of ∼71 HBW. During prolonged NA this value doesn't change much anymore, see figure 5.5. As 1.2×10^6 s of NPA also is an industrially realistic time delay until AA at 170 °C is carried out, this heat treatment history has been investigated in more detail. The results are displayed in figure 5.8. The curvature of the reference alloy is comparable to the one of heat treatment B2

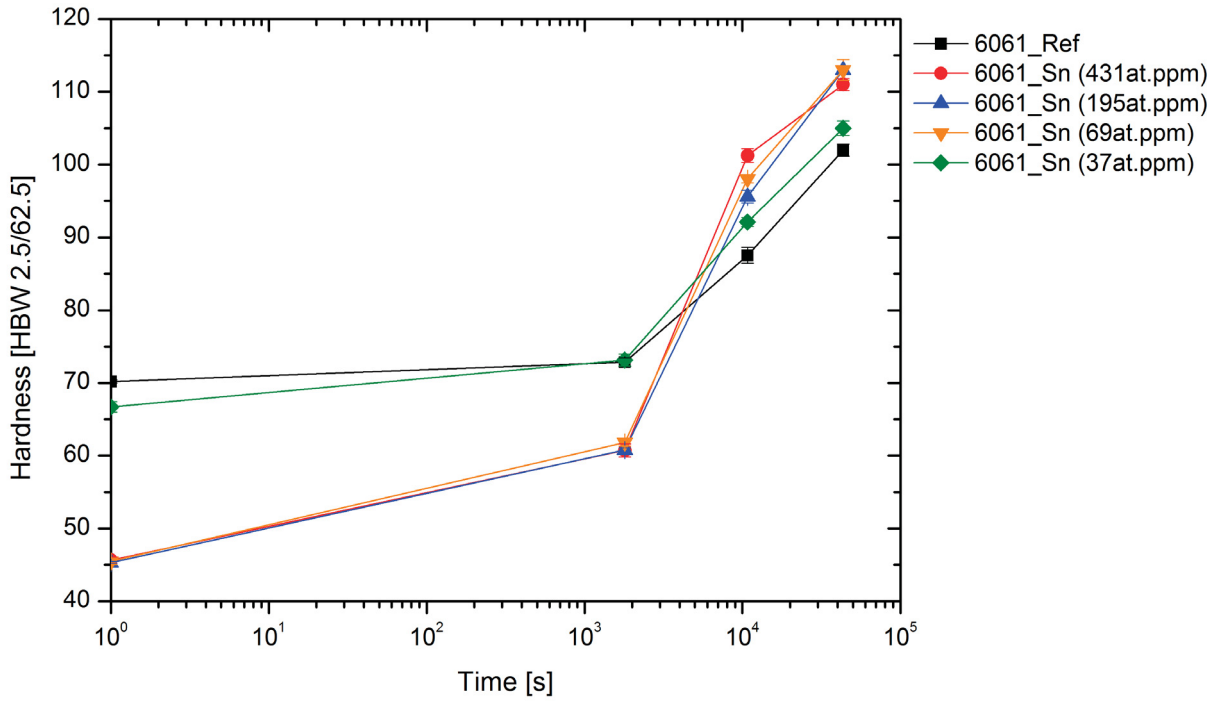

Figure 5.7: Hardness evolution of Sn-added AA6061 alloys with 3.45×10^5 s of intermediate storage at 25 °C during AA at 170 °C

shown in figure 2.7(a). Additionally the reference alloy reveals the beginning of overaging after 4.6×10^5 s (∼5 days) of AA at 170 °C.

At the NPA time of 1.2×10^6 s the alloy with ∼37 at. ppm Sn has already reached about the same hardness as the reference. During AA at 170 °C no difference to the reference alloy can be perceived. Following the same value of ∼73 HBW after 1.8 ks of AA, the ∼37 at. ppm Sn alloy always seems to just slightly exceed the reference curve by not more than ∼5 HBW. There might be an insignigicant sign of a beginning overaging after 4.6×10^5 s of AA, as the hardness drops by about 1 HBW.

The Sn-added alloy containing ∼69 at. ppm Sn exhibits a clearly distinguishable difference in its AA kinetics from the other two alloys with ∼431 and ∼195 at. ppm Sn which still exhibit similar hardening curves. It starts at a larger hardness after NPA (∼50 HBW) and continuous this trend until about the middle of its steep hardness increase at 4.8 ks of AA where similar to the ∼195 at. ppm Sn alloy ∼83 HBW are measured. Thereafter it shows lower hardness values than the other two alloys.

After AA for 43.2 ks the hardness values are ∼105 HBW for the reference and the ∼37 at. ppm Sn alloy, ∼108 HBW for the ∼69 at. ppm Sn alloy, and ∼112–113 HBW for the ∼195 and ∼431 at. ppm Sn alloys, respectively.

For finding out if the AA behavior of the main study alloys changes much after 2.6×10^6 s

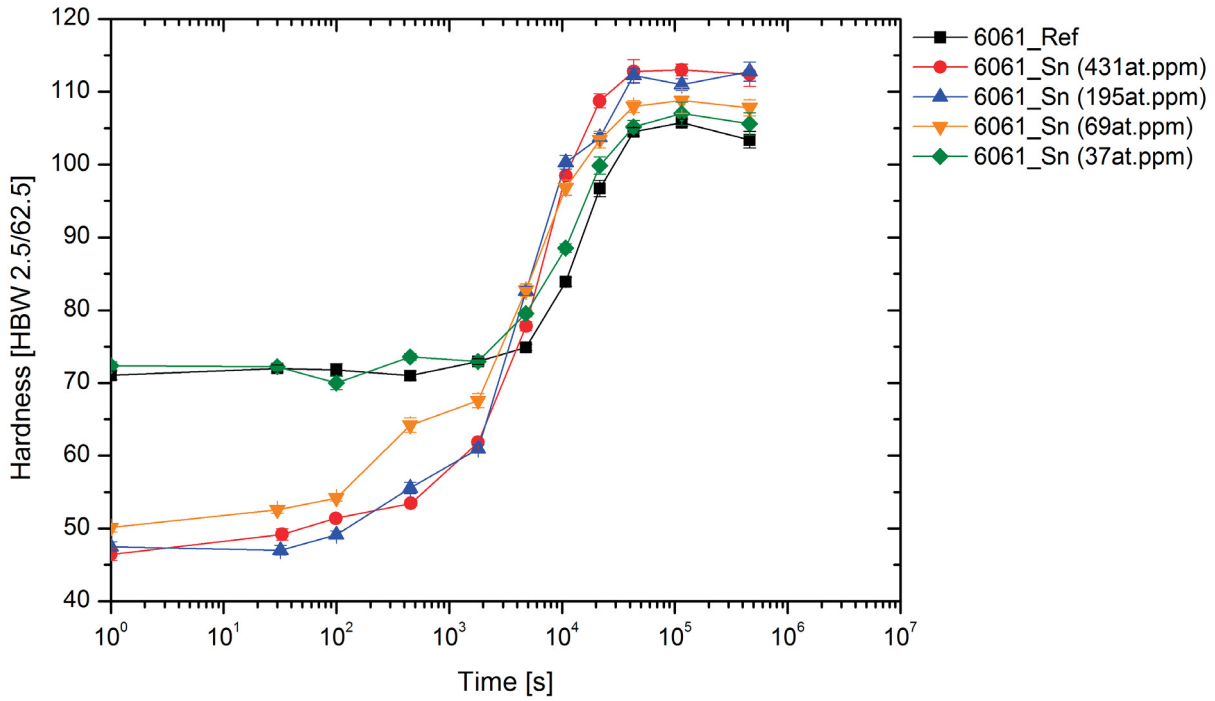

Figure 5.8: Hardness evolution of Sn-added AA6061 alloys with 1.2×10^6 s of intermediate storage at 25 °C during AA at 170 °C

(30 days) of intermediate storage at RT, AA for 1.8 ks and 10.8 ks was carried out at 170 °C. The results are pictured in figure 5.9.

For the ∼37 at. ppm Sn alloy compared to the reference, the result is nearly the same as for 1.2×10^6 s of NPA. Only both starting values are ∼1–2 HBW higher.

It can be said that the kinetics of the ∼69 at. ppm Sn alloy seems to slow down. During NA this alloy at this time is in the middle of a steep logarithmic hardness increase, compare figure 5.5. So the initial value of ∼62 HBW slowly increases to ∼69 HBW after 1.8 ks of AA which is ∼1 HBW higher than the value found after 1.2×10^6 s of NPA and ∼4 HBW beneath the reference. The 10.8 ks value though only reaches ∼87 HBW while the 1.2×10^6 s NPA sample is already ∼10 HBW harder.

For the ∼431 and ∼195 at. ppm Sn alloys both the starting value of ∼49 HBW and the 1.8 ks hardness of ∼66 HBW are the same. Hereafter their kinetics seems to split resulting in ∼93 HBW for the ∼195 at. ppm Sn alloy and ∼98 HBW for the ∼431 at. ppm Sn alloy at 10.8 ks of AA. This contrasts their similar behavior after 1.2×10^6 s of NPA, but might not be significant.

Interesting results were obtained now for AA at higher temperatures than 170 °C, i.e. 210 °C and 250 °C. As before for the 170 °C AA treatment NPA of 1.2×10^6 s has been investigated in more detail because of the industrial importance. Another reason is the full comparability with

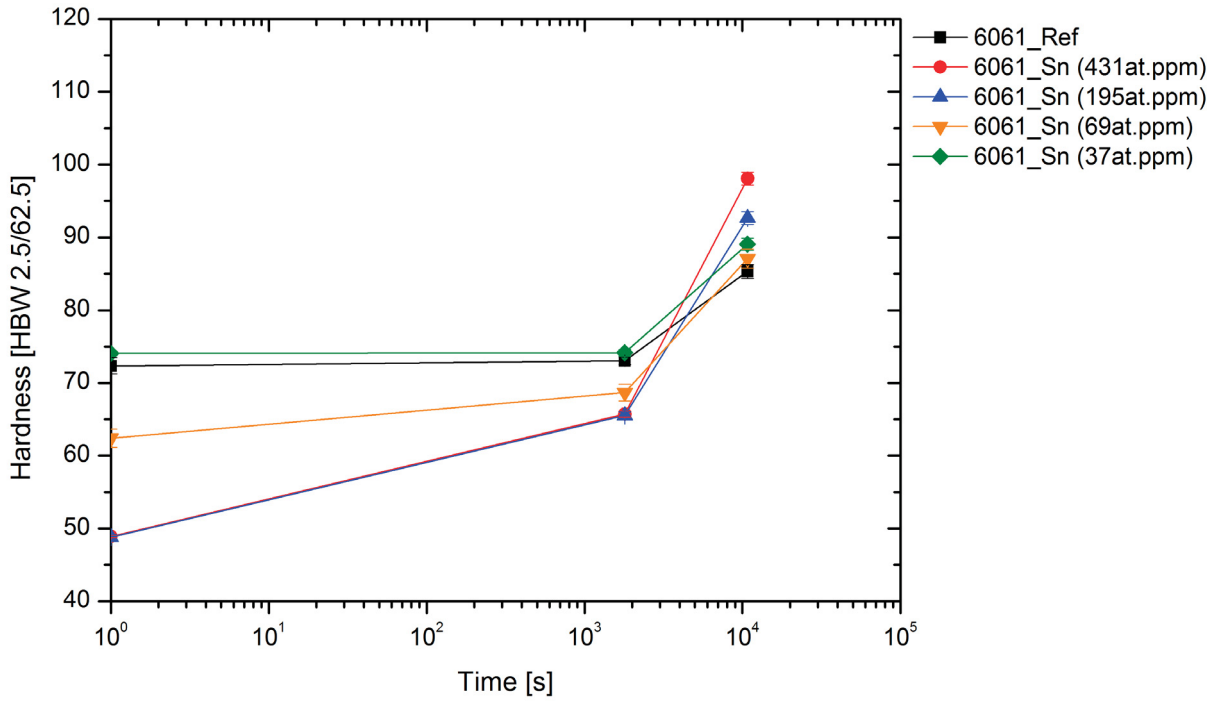

Figure 5.9: Hardness evolution of Sn-added AA6061 alloys with 2.6×10^6 s of intermediate storage at 25 °C during AA at 170 °C

the results obtained from Pogatscher et al. [24] as pictured in figure 2.7(b) and (c).

Similar to its behavior after 1.2×10^6 s of NPA and subsequent AA at 170 °C, the alloy containing ∼37 at. ppm Sn shows a comparable hardness development as the reference during AA at 210 °C, see figure 5.10. At this AA temperature a reversion takes place which has its minimum for both alloys at about 65 HBW after 50 s.

The other three alloys with ∼431, ∼195 and ∼69 at. ppm Sn harden starting from their individual initial values obtained after 1.2×10^6 s of NA. The ∼69 at. ppm Sn alloy first starts as the harder alloy and then shows a slowed down hardness increase which results in a change to the lowest hardness between 50 and 450 s of AA at 210 °C.

After 450 s of AA all alloys show a hardness within ±2-4 HBW of the reference value which is ∼68 HBW. Thereafter all alloys seem to take on a similar hardening kinetics as the reference, i.e. a quick logarithmic hardening. After 900 s (15 minutes) of AA the reference exhibits the lowest hardness of ∼79 HBW while the ∼431 at. ppm Sn alloy is the hardest with ∼90 HBW. Interestingly the ∼37 at. ppm Sn alloy is the second hardest with ∼87 HBW. The ∼69 at. ppm Sn alloy totally follows the reference trajectory.

Continued AA leads to a slowdown of hardening after 1.8 ks where the reference and the alloy containing ∼69 at. ppm Sn both show the lowest hardness of ∼96 HBW, the ∼431 and ∼195 at. ppm Sn alloys are both 7–8 HBW harder.

Maximum hardness is reached after 4.8 ks (80 minutes) of AA. Generally all peak hardnesses are lower than before during AA at 170 °C. The ∼431 and ∼195 at. ppm Sn alloys respectively show a hardness of ∼107 HBW. The ∼37 at. ppm Sn alloy exhibits a hardness of ∼103 HBW while the remaining two alloys are ∼4 HBW softer.

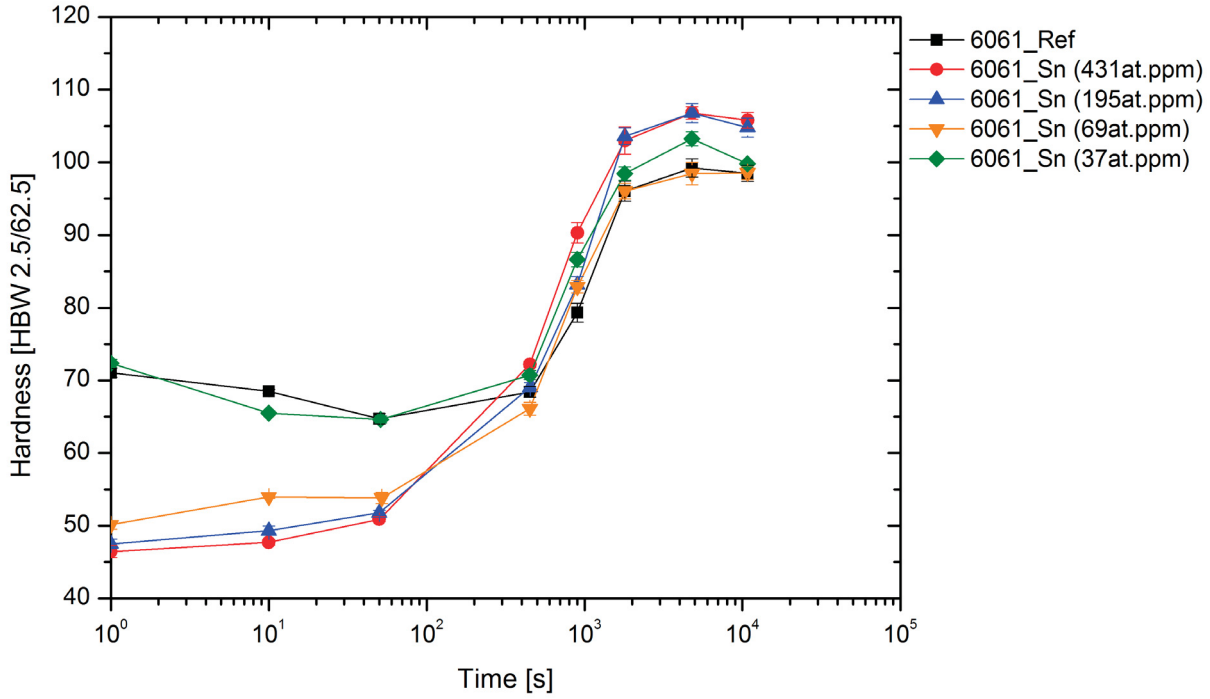

Figure 5.10: Hardness evolution of Sn-added AA6061 alloys with 1.2×10^6 s of intermediate storage at 25 °C during AA at 210 °C

The hardness relationships between the alloys after 1.2×10^6 s of intermediate storage at RT and AA at 250 °C compare well to the results obtained for AA at 210 °C (figure 5.11). Again the reference and the ∼37 at. ppm Sn alloy exhibit a significant reversion with the same curvature. The minimum of ∼54 HBW also occurs at 50 s of AA. A subsequent short steep hardness increase yields the same hardness of ∼77 HBW after 240 s of AA. For both alloys already after 450 s (7.5 minutes) of AA a slowdown in their hardening kinetics is perceived. The maximum for both alloys occurs after 900 s of AA being ∼86 HBW for the Sn-added alloy and ∼85 HBW for the reference.

The alloy containing ∼431 at. ppm Sn as well as the ∼195 at. ppm Sn alloy again follow completely the same hardening path. For AA at 250 °C the ∼69 at. ppm Sn alloy already changes from harder than the ∼431 and ∼195 at. ppm Sn alloys to softer after 10 s of AA where all three alloys show ∼51 HBW. The largest difference of about 10 HBW occurs after 50 s with ∼56 HBW for the ∼69 at. ppm Sn alloy. All three alloys end their fast increase in hardness after 240 s and show their maximum hardness after 450 s of AA which corresponds to the fastest reached maximum measured in this work. The maxima are ∼98 HBW and ∼97 HBW for the

∼431 and ∼195 at. ppm Sn alloy respectively. The ∼69 at. ppm Sn alloy has its maximum at ∼95 HBW. Following their maximum all five alloys clearly exhibit a noticable overaging.

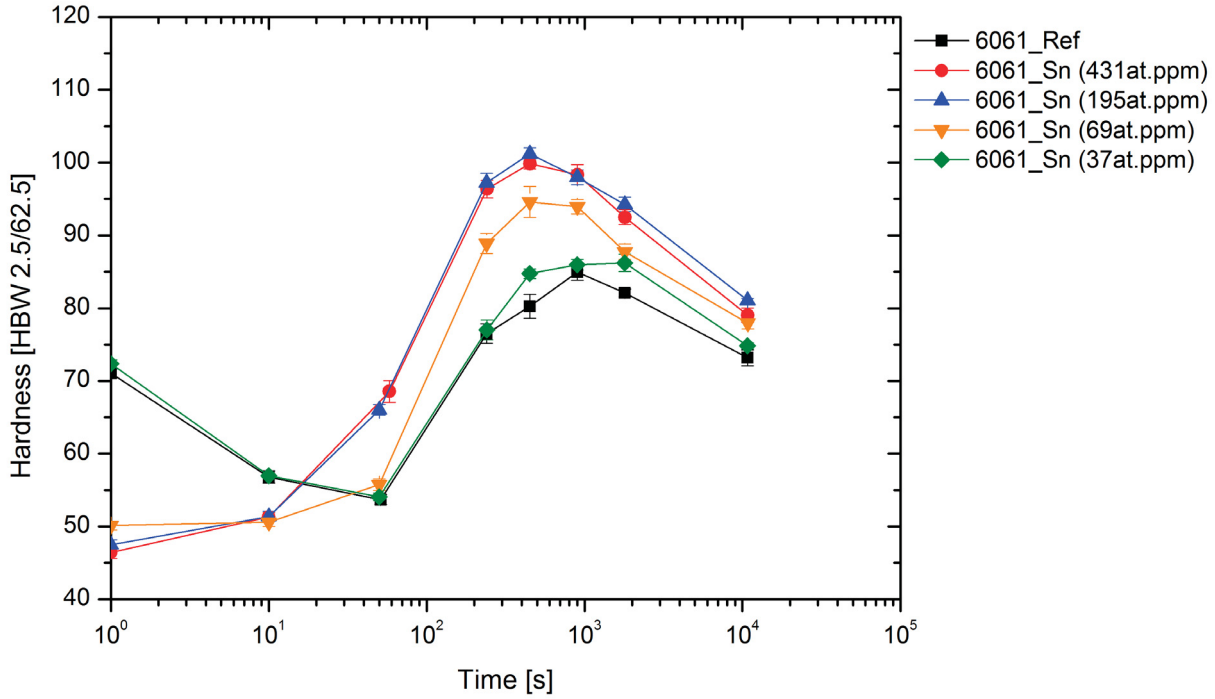

Figure 5.11: Hardness evolution of Sn-added AA6061 alloys with 1.2×10^6 s of intermediate storage at 25 °C during AA at 250 °C

Summing up the results of the main study, the Sn-added alloys mostly seem to follow a kind of trend relative to the amounts added. During NA (figure 5.5) the alloy containing ∼37 at. ppm Sn remains at its as-quenched hardness level, i.e. ∼47 HBW, until about 100.8 ks of NA before it starts a fast increase in hardness. The alloy with ∼69 at. ppm Sn starts its increase in hardness as the second one between 3.45×10^5 s and 1.2×10^6 s (14 days). In the same time period, but at a much slower rate, also the alloys containing ∼195 and ∼431 at. ppm Sn start hardening.

While the ∼37 at. ppm Sn alloy reveals the by far fastest hardening kinetics during AA at 170 °C after 28.8 ks of intermediate storage at RT (figure 5.6), it shows a reduced hardening compared to the reference during AA after four days of NPA (figure 5.7). Note that it already shows significant hardening during NPA (figure 5.5). With still higher starting values after 1.2×10^6 s and 2.6×10^6 s of NPA this observation is also valid for AA at 170 °C (figures 5.8 and 5.9), 210 °C (figure 5.10) and 250 °C (figure 5.11). During following AA the 37 at. ppm Sn-added alloy always seems to just slightly exceed the reference anymore. A obvious difference between AA at 170 °C and the higher AA temperatures of 210 and 250 °C is the occurrence of a reversion which is most distinctive for 250 °C.

The aging behavior of the three alloys with higher amount of Sn at 170 °C after 3.45×10^5 s storage at RT (figure 5.7) more or less resembles the one after NPA for 28.8 ks (figure 5.6).

For the ∼69 at. ppm Sn alloy AA at 170 °C after 1.2×10^6 s and 2.6×10^6 s of NPA (figures 5.8 and 5.9) reveals a higher initial hardness compared to the alloys with higher amount of Sn. During the hardness increase in AA, this relationship switches to the lowest hardness of the three alloys. This change also occurs for AA at 210 and 250 °C after 1.2×10^6 s of NPA (figures 5.10 and 5.11), but it seems to be earlier, i.e. already before the hardening starts. The ∼195 and ∼431 at. ppm Sn alloys show a comparable hardening trajectory and highest maxima for all AA treatments after 1.2×10^6 s and 2.6×10^6 s of NPA. In general the 69, 195 and 431 at. ppm Sn alloys do not show a reversion during any heat treatment.

Finally the results of the main study are compared to the pretest results for the In-added alloy. These results seem to be comparable to the ones obtained for the ∼69 at. ppm Sn alloy. Its increase in hardness also seems to start between NA for 3.45×10^5 s and 1.2×10^6 s (figure 5.1(b)). For rising NPA times also a slowdown in the hardening kinetics compared to the reference alloy is perceived (figures 5.2(b), 5.3(b)).

The behavior of the Cd-added pretest alloy seems to be similarly as the one of the ∼37 at. ppm Sn alloy. Hardening during NA occurs between 28.8 ks and 3.5×10^5 s (figure 5.1(a)) and yields after 28.8 ks of NPA (figure 5.2(a)) the fastest hardness increase of all alloys during AA at 170 °C. Longer NPA also reduces the potential for AA comparable to the 37 at. ppm Sn alloy (figure 5.2(a), 5.3(a), 5.4).

5.2.2 Atom Probe Tomography

Two specimens with Sn addition of ∼195 at. ppm in AA6061 were investigated: a NA-sample (1.2×10^6 s) and a NPA-specimen (1.2×10^6 s) which was subsequently artificially aged at 170 °C for 43.2 ks.

5.2.2.1 Sn-Solubility

The result of table 5.1 is an estimation of the solute Sn concentration in ∼195 at. ppm Sn-added AA6061. The mean value of four datasets lets suggest a Sn solubility of ∼94 at. ppm±15 at the solution treatment temperature of 570 °C. The values have to be seen as preliminary results, because several effects such as a pole-segregation or the influence of a different range file could not be avoided. Much more effort is necessary to deduce exact values of the concentration of trace elements from APT.

Table 5.1: Concentrations of elements (c) in four different APT-measurements of ~195 at. ppm Sn-added AA6061 given in at.% in two samples with 43.2 ks of AA at 170 °C and 1.2×10^6 s of NPA (c_{AA}) and two samples with 1.2×10^6 s of NA (c_{NA}). Further listed: mean value ($mean$), standard deviation (σ) and relative error [%] ($error$) of the concentration data.

Element	c_{AA}	c_{AA}	c_{NA}	c_{NA}	mean	σ	error
	[at.%]	[at.%]	[at.%]	[at.%]	[at.%]		[%]
Al	98.7237	98.7944	98.3744	98.3754	98.5670	0.2237	0.23
Mg	0.7707	0.7031	0.9209	0.8492	0.8110	0.0945	11.65
Si	0.3300	0.3012	0.5101	0.5380	0.4198	0.1214	28.93
Cu	0.0610	0.0706	0.0788	0.0880	0.0.746	0.0115	15.44
Sn	0.0102	0.0071	0.0097	0.0104	0.0094	0.0015	16.57
Mn	0.0235	0.0150	0.0233	0.0191	0.0202	0.0040	19.92
Cr	0.0379	0.0536	0.0343	0.0615	0.0468	0.0129	27.47
Zn	0.0352	0.0268	0.0393	0.0285	0.0324	0.0058	17.99
Ti	0.0026	0.0211	0.0027	0.0240	0.126	0.0115	91.76
Ga	0.0043	0.0036	0.0042	0.0036	0.0039	0.0004	10.13
V	0.0009	0.0035	0.0023	0.0023	0.0022	0.0011	47.24

5.2.2.2 Natural Aging

To better understand how trace amounts of Sn in AA6061 are able to temporarily suppress the increase in hardness during NA, APT analyses were performed for the main study alloy containing ~195 at. ppm Sn (figure 5.12). The results are compared to a AA6061 alloy, which was long-term naturally aged and measured by APT at Leoben within a previous study [24] (figure 5.13).

Figure 5.12 shows nearest neighbor (NN)-distribution plots of the elements Mg (a) and Si (b) for 1.2×10^6 s (14 days) naturally aged samples containing ~195 at. ppm Sn. After this NA period the alloy still exhibits nearly its as-quenched hardness (figure 5.5), which was the reason for examining this sample.

The plots 5.12(a) and 5.12(b) reveal a rather homogeneous distribution of Mg and Si, i.e. the graphs of a theoretically calculated random distribution ("XX_Randomized Count") fit reasonably well the measured distribution of the individual elements ("XX_Count"). Another analysis indicates a rather homogeneous Sn distribution (figure 5.12(c)), but as the amount of Sn is very low, it is difficult to obtain significant statistics.

Figure 5.13 shows NN-distribution plots of the elements Mg (a) and Si (b) for the long-term naturally aged alloy AA6061 without Sn-addition. After this NA time the sample already reached peak hardness during NA which indicates the existence of Mg-Si co-clusters.

The graphs reveal that the theoretically calculated random distribution ("XX_Randomized Count") does not fit the measured distribution of Mg (figure 5.13(a)). Due to the relatively

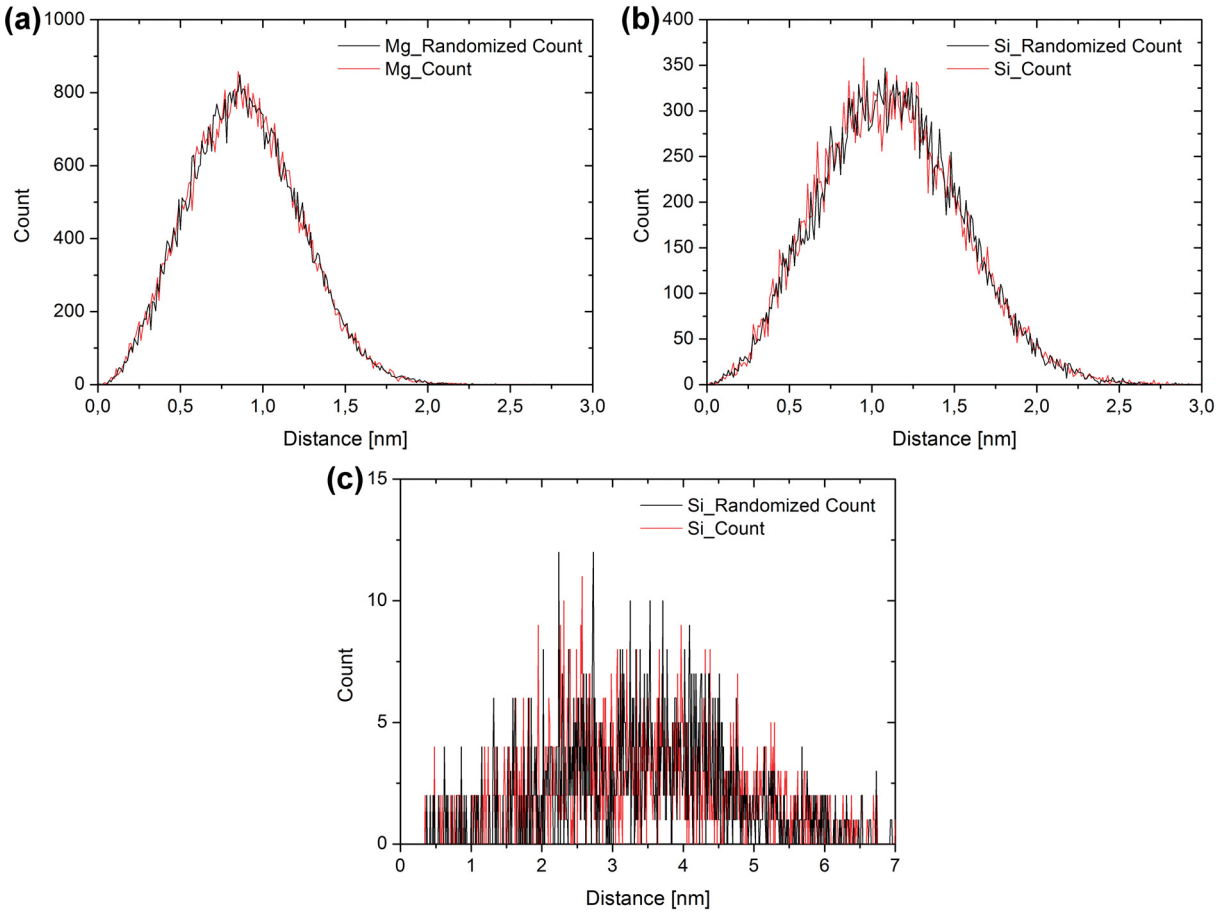

Figure 5.12: Nearest neighbor-distribution analysis of AA6061 containing ∼195 at. ppm Sn and 1.2×10^6 s of NA for (a) Mg, (b) Si and (c) Sn. The analyzed volume contained 7-8 million atoms

small amount of analyzed atoms (1–1.5 million atoms) the result for the Si-distribution (figure 5.13(b)) might seem less clear.

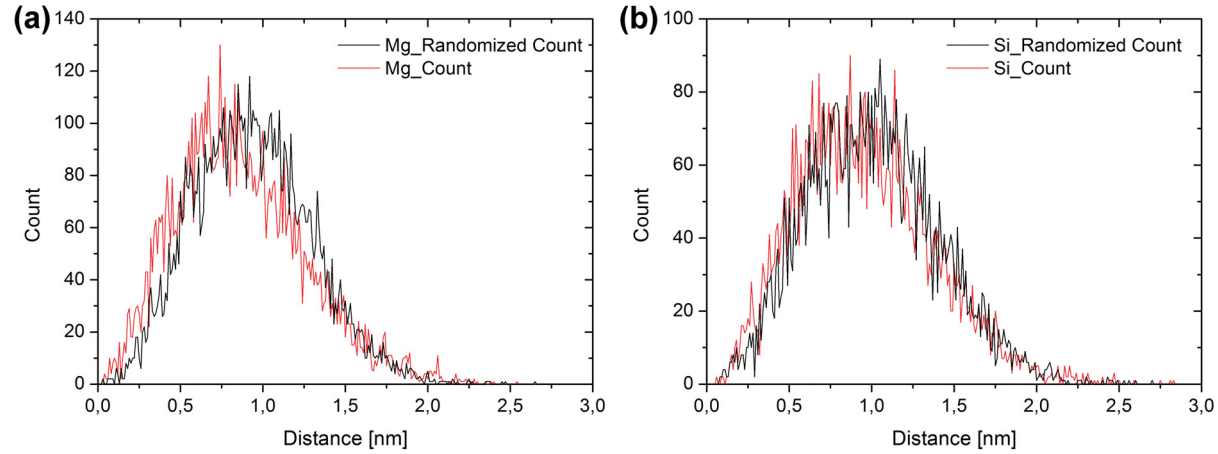

Figure 5.13: Nearest neighbor-distribution analysis of AA6061, long-term naturally aged for (a) Mg and (b) Si. The analyzed volume contained 1–1.5 million atoms

5.2.2.3 Artificial Aging at 170 °C

Figure 5.14 shows the element distribution of Mg (a), Si (b), Cu (c) and Sn (e) in the ∼195 at. ppm Sn-added alloy which was AA at 170 °C for 43.2 ks after 1.2×10^6 s of NPA. Figure 5.14(d) illustrates 5 %-isoconcentration surfaces of Mg. The latter clearly reveals the existence of needle-shaped precipitates. These are also clearly recognizable in the Si- (figure 5.14(b)) and Cu-atom maps (figure 5.14(c)) plots. When figure 5.14(e) (Sn) and another one of Mg, Si or Cu are laid on top of each other also some inhomogeneities of Sn are faintly perceptible at the positions where also Mg, Si and Cu are accumulated. In the following the concentration of Sn in precipitates defined by 5 %-isoconcentration surfaces of Mg is analyzed more closely.

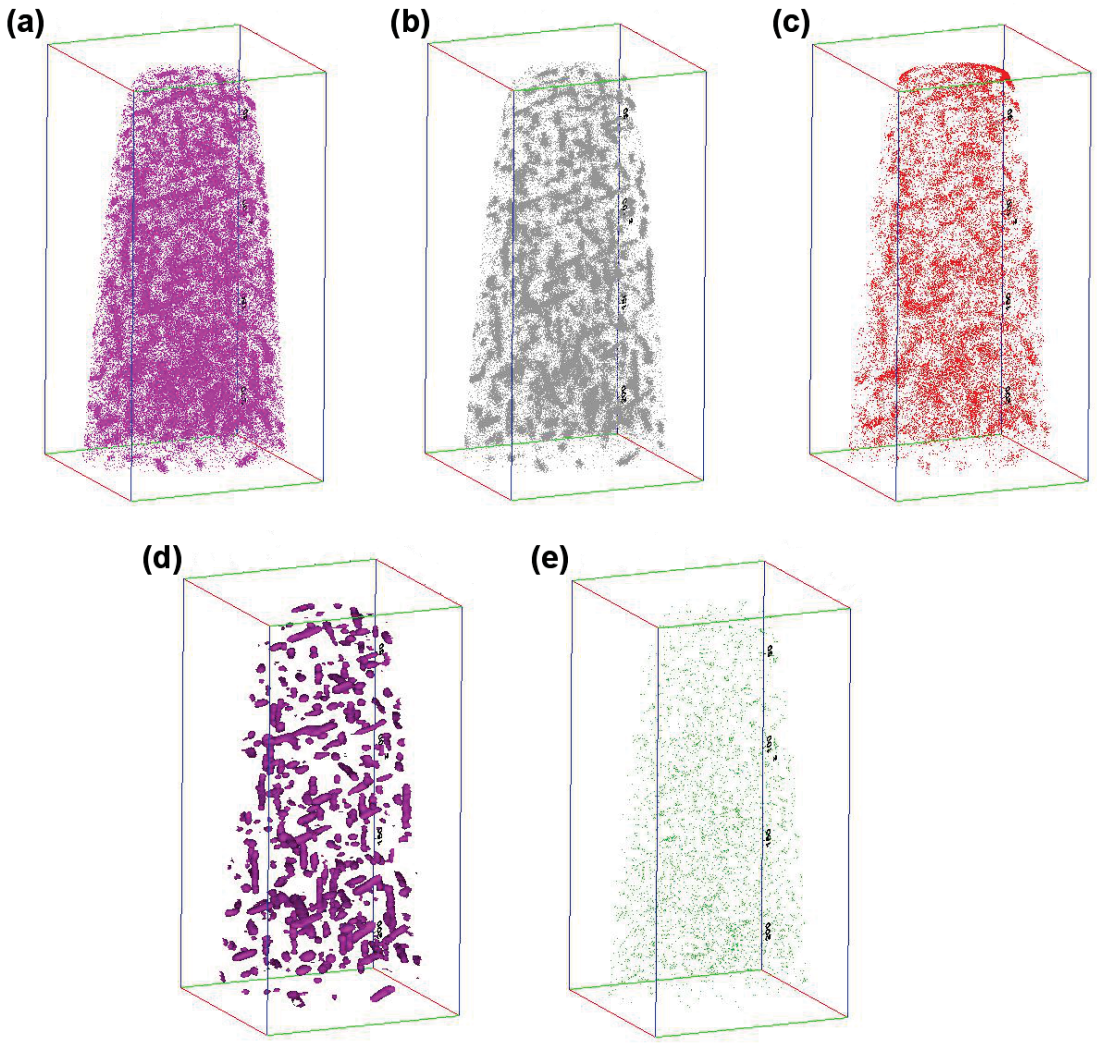

Figure 5.14: Element distribution of (a) Mg, (b) Si, (c) Cu, (e) Sn and (d) 5 %-isoconcentration surfaces of Mg in the ∼195 at. ppm Sn-added alloy artificially aged for 43.2 ks at 170 °C after 1.2×10^6 s of NPA

Table 5.2 lists concentrations of various elements in the particles defined by the 5 % isoconcentration surfaces of Mg ($c_{particle}$) and outside these particles, i.e. in the matrix (c_{matrix}). The

factor in the last column indicates how much the concentration in the precipitate exceeds that in the matrix. High factors are perceived for the elements Si (36.1), Mg (22.7), Cu (12.2) and Sn (26.1). Two other elements, Ga (5.30) and Cr (2.5), also reveal slightly higher factors, but it has to be noted that the Cr value might be lower in reality as one Cr-peak overlaps with Mg. The most astonishing result is however the existence of such a large proportion of Sn atoms in the particles defined by the 5 % isoconcentration surfaces of Mg.

Table 5.2: Concentrations of elements in particles defined by 5 % isoconcentration surfaces of Mg ($c_{particle}$) and outside of these particles (c_{matrix}). Factor=$c_{particle}/c_{matrix}$.

Element	c_{matrix}	$c_{particle}$	Factor
	[at.%]	[at.%]	
Al	99.1805	82.3466	0.8
Mg	0.4620	10.5071	22.7
Si	0.1648	5.9495	36.1
Cu	0.0678	0.8283	12.2
Sn	0.0038	0.0989	26.1
Mn	0.0149	0.0204	1.4
Cr	0.0520	0.1283	2.5
Zn	0.0263	0.0680	2.6
Ti	0.0212	0.0309	1.5
Ga	0.0033	0.0178	5.3
V	0.0035	0.0042	1.2

Figure 5.15 illustrates a NN-distribution plot of Sn using the total dataset (32 million atoms). It clearly demonstrates a deviation of the "Sn_Count"-graph from the "Sn_Randomized Count"-graph which indicates that Sn is inhomogeneously distributed in AA6061 after 43.2 ks of AA at 170 °C and 1.2×10^6 s of NPA.

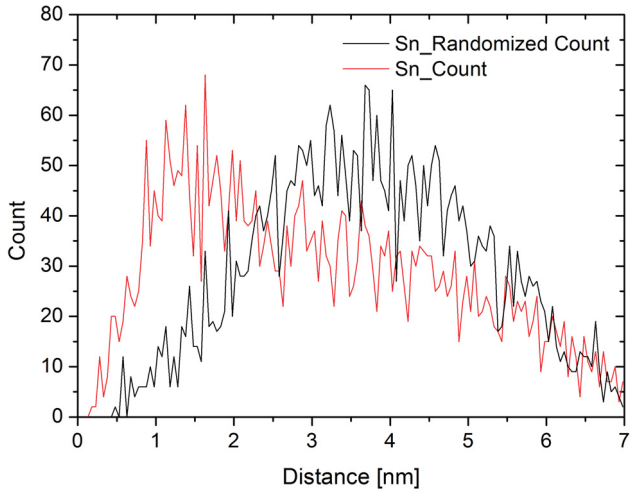

Figure 5.15: Nearest neighbor-distribution analysis for Sn in AA6061 containing ~195 at. ppm Sn for 43.2 ks of AA at 170 °C after 1.2×10^6 s of NPA

6 Discussion

The purpose of this work was to show if microalloying (MA) elements are able to change the precipitation process of Al-Mg-Si alloys showing the negative effect of natural preaging (NPA) on artificial aging (AA). According to the theory this work is based on (see section 2.1.4.1) vacancies are believed to play an important role in the Mg-Si co-cluster formation during NA [24]. It is assumed that a suppression of the co-cluster formation by the addition of MA elements could affect the influence of NPA on AA. One possibility might be that instead or in addition of Mg-Si co-clusters other thermally less stable vacancy-solute clusters could form. During subsequent AA these new clusters might dissolute faster, also already at lower AA temperatures and like this enhance the precipitation kinetics of NPA samples during AA. In the experimental part of this work the technological important Al alloy AA6061, which shows the adverse effect of NPA on subsequent AA, has been studied with addition of selected MA elements.

In all performed pretest heat treatments the three elements Sn, In and Cd continuously showed a high influence. Some other MA elements which were studied in the pretest measurements also showed slight hardness deviations from the reference during various heat treatments, but no strong changes were perceived. Sn, In and Cd however significantly influenced not only the NA kinetics but also the subsequent AA kinetics during AA at 170, 210 and 250 °C. Furthermore a preliminary atom probe tomography (APT) analysis exhibited a more homogeneous Mg and Si distribution after 1.2×10^6 s of NA in the $\sim$195 at. ppm Sn alloy compared to a long-term naturally aged standard AA6061 alloy and the occurrence of Sn atoms at the positions where Mg, Si and Cu atoms are accumulated after subsequent AA for 43.3 ks at 170 °C. The APT results therefore seem to verify that Sn-addition temporarily suppresses the Mg-Si co-cluster formation during NA. These results also indicate that Sn might play a role in the nucleation process during AA, which might be the reason for the measured higher hardness maxima. For the $\sim$195 at. ppm Sn alloy the concentration of solute Sn measured by APT is about 94 ± 15 at. ppm, which should be a realistic order of magnitude as far as the FactSage 6.2^{TM} calculations are concerned, see table 4.2. In the following possible reasons for the effect of MA elements are discussed taking the role of vacancies during aging into account.

6.1 Calculation of Five Frequency Model–Values

Table 6.1 lists ω_i values which were calculated from data either of Simonovic and Sluiter [55] (table 2.2) or Mantina et al. (table 2 in [43]) using the binding enthalpies δH_B, the solute migration enthalpies H_M^B and the Al migration enthalpies $H_M^{Al(1)}$ and $H_M^{Al(3)}$. These data were processed using the formulas given by Mantina et al. [43]: $H_M^{Al(1)}$, H_M^B and $H_M^{Al(3)}$ are applied to equation 2.19 to obtain ω_1, ω_2 and ω_3, respectively. The mean value of table 3 in [43] was used for ν^*, i.e. 19.4·10^{12} Hz. This is a simplification as in reality this value can be half or double which is a small variation compared to the other influences. δH_B was used to calculate ω_4 from $\omega_4 = \omega_3 \exp\left(-\frac{\delta H_B}{kT}\right)$ (also compare with equation 2.10). ω_0 equals the ω_i values of the matrix Al. With these values F in equation 2.20 was possible to calculate from equation 6.1 with $x = \omega_4/\omega_0$:

$$F(x) = 1 - \frac{10x^4 + 180.5x^3 + 927x^2 + 1341}{7(2x^4 + 40.2x^3 + 254x^2 + 597x + 435)} \tag{6.1}$$

F (see next paragraph which revises the meaning of F) was inserted in equation 2.20 to obtain the correlation factor f_2. These calculations were performed for various temperatures to be able to plot f_2 as a function of temperature, see figure 6.1. 630 and 400 K serve as a comparison to the results from Simonovic and Sluiter [55] (630 K) and Mantina et al. [43] (400 K). 523.15, 443.15 and 298.15 K are the heat treatment temperatures used in this work. As far as the calculations with the data of Mantina et al. [43] are concerned, about the same dependence of f_2 from temperature for Mg, Si and Cu was obtained as published in the original paper, compare figures 6.1(a) and 2.15(a). Of the two authors only Simonovic and Sluiter [55] published data for Sn, In and Cd, the corresponding logarithmic f_2 vs. temperature plot is shown in figure 6.1(c). It should be noted that the main influence which is responsible that figure 6.1(b) (data of Simonovic and Sluiter [55]) differs from figure 6.1(a) are the deviating δH_B values of Mg, Si and Cu calculated by Simonovic and Sluiter [55] and Mantina et al. [43], compare table 2.2. Another smaller influence are also varying H_M^B, $H_M^{Al(1)}$ and $H_M^{Al(3)}$ values obtained by the two authors (see table 2.2 and table 2 in [43]). Further the reader should be aware that all calculations are meant to qualitatively illustrate the difference in the alloying behavior in Al between the main alloying elements in AA6061 (Mg, Si and Cu) to the MA elements Sn, In and Cd added to AA6061 in this work.But all in all the results are quite useful as far as trends are concerned.

Table 6.1: Estimation of five jump frequencies ω_i in units of 10^5 Hz for Mg, Si, Cu, Sn, In, Cd and the matrix Al for various temperatures T [K]. From these ω_i-values F, f_2 and ratios $\frac{\omega_4}{\omega_0}$, $\frac{\omega_1}{\omega_3}$, $\frac{\omega_2}{\omega_1}$ are calculated. Used formulas from Mantina et al. [43], data either from [43] or Simonovic and Sluiter [55] (table 2.2). ν^*=19.4·10^{12} Hz (mean value of table 3 in [43]). Values for Al-matrix: ω_i=ω_0 of solutes, for all T: F=0.74, f_2=0.78, all ω_i-ratios=1.00

T	Solute	ω_0	ω_1	ω_2	ω_3	ω_4	F	f_2	$\frac{\omega_4}{\omega_0}$	$\frac{\omega_1}{\omega_3}$	$\frac{\omega_2}{\omega_1}$
630	Mg[43]	4413	706	85099	19567	5342	0.73	0.42	1.21	0.04	120
	Si[43]	4413	13356	7678	1015	7678	0.70	0.70	1.74	13.2	0.57
	Cu[43]	4413	175787	5342	2537	4414	0.74	0.97	1.00	69.3	0.03
	Mg[55]	16795	1699	137152	29780	36044	0.67	0.53	2.15	0.06	80.7
	Si[55]	16795	29780	43625	6466	16795	0.74	0.52	1.00	4.61	1.46
	Cu[55]	16795	243183	63909	9472	9472	0.72	0.80	0.56	25.7	0.26
	Sn[55]	16795	447	1640737	2489	294337	0.36	0.03	17.5	0.18	3674
	In[55]	16795	305	1985864	3013	166002	0.42	0.02	9.88	0.10	6515
	Cd[55]	16795	958	1985864	3647	63909	0.58	0.01	3.81	0.26	2072
523.15	Mg[43]	497	54.7	17543	2987	626	0.73	0.35	1.26	0.02	321
	Si[43]	497	1886	968	84.7	968	0.67	0.70	1.95	22.3	0.51
	Cu[43]	497	42025	626	255	497	0.74	0.99	1.00	165	0.01
	Mg[55]	2486	158	31168	4954	6235	0.65	0.48	2.51	0.03	198
	Si[55]	2486	4954	7846	787	2486	0.74	0.47	1.00	6.29	1.58
	Cu[55]	2486	62122	12426	1247	1247	0.72	0.84	0.50	49.8	0.20
	Sn[55]	2486	32	619000	249	78179	0.33	0.014	31.5	0.13	19648
	In[55]	2486	20	778996	314	39225	0.37	0.009	15.8	0.06	39160
	Cd[55]	2486	79	778996	395	12426	0.53	0.005	5.00	0.20	9859
443.15	Mg[43]	48.7	3.6	3267	404	63.8	0.72	0.29	1.31	0.01	909
	Si[43]	48.7	235	107	6.0	107	0.67	0.71	2.20	39.0	0.46
	Cu[43]	48.7	9162	63.8	22.1	48.7	0.74	0.99	1.00	414	0.01
	Mg[55]	325	13	6438	734	963	0.62	0.42	2.96	0.02	514
	Si[55]	325	734	1263	84	325	0.74	0.43	1.00	8.77	1.72
	Cu[55]	325	14534	2174	144	144	0.71	0.87	0.44	101	0.15
	Sn[55]	325	1.9	219320	22	19066	0.31	0.006	58.6	0.09	117048
	In[55]	325	1.1	287705	28	8446	0.34	0.003	26.0	0.04	264224
	Cd[55]	325	5.5	287705	37	2174	0.48	0.001	6.68	0.15	51851
400	Mg[43]	9.4	0.53	998	98.5	12.8	0.72	0.25	1.35	0.01	1895
	Si[43]	9.4	54.0	22.6	0.93	22.6	0.66	0.72	2.39	57.9	0.42
	Cu[43]	9.4	3129	12.8	3.9	9.4	0.74	1.00	1.00	792	0.004
	Mg[55]	77	2.1	2116	191	258	0.60	0.39	3.33	0.01	1008
	Si[55]	77	191	348	17	77	0.74	0.40	1.00	11.08	1.82
	Cu[55]	77	5216	636	31	31	0.70	0.89	0.41	166	0.12
	Sn[55]	77	0.3	105487	3.8	7046	0.30	0.0035	90.9	0.07	412206
	In[55]	77	0.1	142490	5.2	2859	0.32	0.0015	36.9	0.03	1015937
	Cd[55]	77	0.9	142490	7.0	636	0.44	0.0006	8.21	0.12	167249
298.15	Mg[43]	0.030	0.0006	15.6	0.697	0.045	0.72	0.14	1.50	0.0009	24965
	Si[43]	0.030	0.311	0.097	0.001	0.097	0.61	0.77	3.22	232	0.31
	Cu[43]	0.030	72.2	0.045	0.009	0.030	0.74	1.00	1.00	7749	0.0006
	Mg[55]	0.5	0.004	43	1.7	2.5	0.52	0.27	5.02	0.00	10701
	Si[55]	0.5	1.7	3.8	0.07	0.5	0.74	0.33	1.00	25.2	2.24
	Cu[55]	0.5	143	8.5	0.15	0.15	0.68	0.94	0.30	951	0.06
	Sn[55]	0.5	0.0002	8091	0.009	214	0.29	0.00047	425	0.03	34140867
	In[55]	0.5	0.0001	12111	0.014	64	0.30	0.00015	127	0.01	114512221
	Cd[55]	0.5	0.0012	12111	0.020	8.5	0.37	0.00004	16.8	0.06	10178816

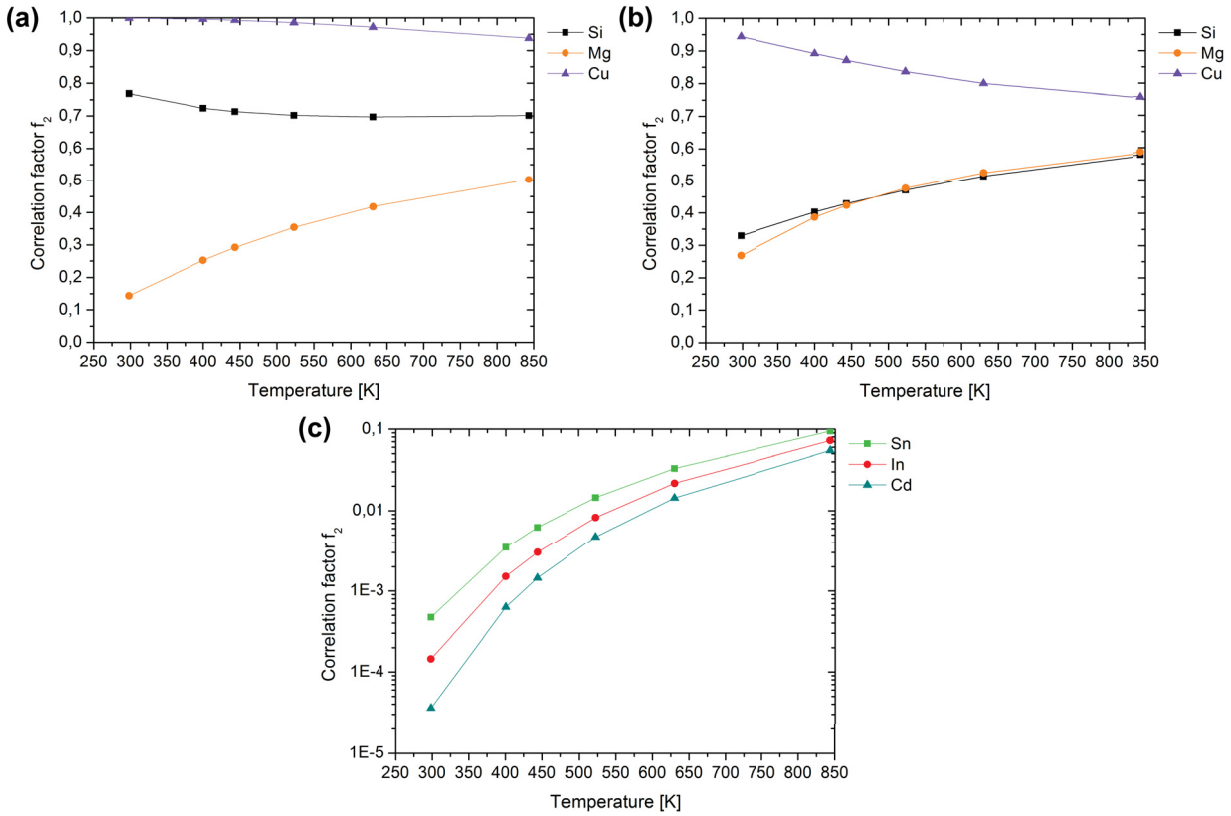

Figure 6.1: Calculated correlation factor f_2 as a function of temperature, compare to table 6.1 using (a) data for Si, Mg and Cu from Mantina et al. [43] or (b) from Simonovic and Sluiter [55] and (c) data for Sn, In and Cd from [55]

In order to help the reader the meaning of the individual five frequency model-values is recapitulated (section 2.3.2.1). Figure 2.12 respectively labels one example of the individual jump frequencies ω_i. There are three possible dissociative jumps which separate a vacancy from a neighboring solute atom, the corresponding dissociative jump frequency is called ω_3. ω_4 signifies the frequency of the reverse jump, i.e. associative jump. ω_2 marks the solute-vacancy exchange and ω_1 describes the vacancy jump around the solute atom, which avoids the break of the solute-vacancy complex. ω_0 denotes a jump not affected by the solute atom, the vacancy can be seen as a free one. It should also be remembered that in general the physical quantities which are compared to experimental diffusion data in dilute alloys are all functions of only three independent ratios of these five jump frequencies, namely ω_2/ω_1 (small value if a vacancy favors to jump around the impurity instead of exchanging places with it), ω_3/ω_1 (small value if a vacancy stays near the impurity) and ω_4/ω_0 (large value if a vacancy likes to jump in the vicinity of the impurity instead of away by preferring to exchange places with a matrix atom). [44] An estimation of f_0 for a FCC lattice with $n = 12$ (like Al) yields ~0.78 [26]. A lower f_2 means that the the impurity motion is correlated to the vacancy, i.e. ω_1 and ω_3 are low while the vacancy and the impurity tend to exchange places (high ω_2), compare to equation 2.20. For higher f_2 reverse jumps are not the rule anymore, i.e. the vacancy does not tend to

remain near the impurity. F means the fraction of dissociating vacancies that are permanently lost from a site and not compensated by to the impurity returning vacancies [29,30].

6.1.1 Interpretation

It is thought reasonable to first only discuss and compare the results from table 6.1 for the main alloying elements Mg, Si and Cu and link these interpretations to the theory of Pogatscher et al. [24] explaining the influence of NPA on AA which has been presented in section 2.1.4.1. Then, based on the calculated five frequency values, it should be easier to imagine how trace amounts of Sn, In and Cd are able to change the precipitation kinetics of the alloy AA6061 in such a fundamental way. Note that for Mg, Si and Cu the results of table 2.3 (original calculations of Mantina et al. [43]) should also be kept in mind.

6.1.1.1 Mg, Si or Cu in the Al Matrix

Mg seems to possess the smallest migration enthalpy H_M^B of the three atoms which consequently results in the largest ω_2 values at all temperatures. One influence to the smaller H_M^B value of Mg is thought to be the larger atomic size of Mg compared to the Al matrix ($r_{Mg}/r_{Al} \sim 1.12$, table 2.1). The large ω_2 value means that many reverse jumps should occur between Mg and the vacancy. But as δH_B is correlated to ω_4/ω_3 and Mg seems to possess just a slight attractive binding enthalpy δH_B (-1 kJ/mol [55]) or even a repulsive one (+6.8 kJ/mol [43]) it should be, from the vacancy point of view, not so important for the vacancy to jump in the vicinity of Mg (ω_4), it also likes to jump away (ω_3). This can be seen from the low ω_4/ω_3 ratios. Furthermore, compared to Si and Cu, Mg exhibits the largest ω_2 and lowest ω_1 values which result in the lowest correlation factor f_2 for Mg. This is still more pronounced in the results of Mantina et al. [43]. Another interpretation of these results is that, although the vacancy does not tend to favorably jump in the vicinity of Mg, a vacancy that once became a first NN of Mg will not easily be released from Mg again because Mg likes to exchange places with it.

With rising temperature the f_2 value of Mg rises (figures 6.1 and 2.15(a)) which means that the Mg-vacancy correlation becomes lower. The data from table 6.1 indicate that the disproportionally dropping ω_2/ω_1 ratio of Mg most influences this development. This could mean that the ability of Mg to hold a vacancy nearby by reverse jumps sinks and instead the vacancy is able to easier jump around a Mg atom (ω_1).

Another point that should be addressed concerning Mg is that as far as the calculations of Mantina et al. [43] (figure 6.1(a)) are concerned, Mg is the only element that shows a significantly rising f_2 with increasing temperature (remember that Mantina et al. only calculated

solute Mg, Si and Cu-interactions with vacancies in Al matrix). Section 2.3.2 discussed that f_2 as a function of ω_i is temperature-dependent as well. Heumann [30] stated that, if $f_2 < f_0$, plus if no divacancies are involved in the diffusion process, f_2 rises with temperature. Mg fulfills both requirements, so the temperature dependent f_2 could mean that no divacancies are involved in the diffusion process, i.e. Mg atoms might only be associated with one vacancy .

Cu is a TM and alloyed in Al smaller than its matrix. Simonovic and Sluiter [55] called Cu a normal "free-electron" metal with a weak attractive δH_B (0 kJ/mol [55], -2.9 kJ/mol [43]) and migration barriers fairly close to that of Al (section 2.4.2.1). The last point also seems to be in accordance with the calculated ω_2, ω_3 and ω_4 values which stay in about the same order of magnitude as the ω_i of the Al matrix (also compare to table 2.3). ω_1 here seems to be an exception, i.e. as its $H_M^{Al(1)}$ value is the lowest of all solutes listed in table 2.2 its ω_1 values by far exceed the ones of all other alloying elements in the alloy AA6061 which have been taken into account in this work. These data yield the following interpretations: As the δH_B tends to be slightly attractive a vacancy likes to be in the vicinity of Cu, but to Cu itself it does not matter if the vacancy is nearby, i.e. Cu does not (or barely) prefer to exchange places with the vacancy (low ω_2). This means that as soon as a vacancy neighbors Cu it can jump around Cu instead, this can be seen from the huge ω_1 values and the small ω_2/ω_1 ratios of Cu. The background of this behavior might be weak hybridization effects. As can be interpreted from section 2.4.1.2 for Cu alloyed in Al hybridization still might play a role as it was found for Ag. So maybe the vacancy likes to be around Cu and Cu allows it because the Al-Cu bond is still important but not too strong. Note that these are assumptions and are for sure in need of a verification. Also no explanation can be provided here, why exactly a vacancy should be attracted to Cu. Regardless of the reason for Cu's behavior the calculated data of table 6.1 imply that as a consequence of the small ω_2/ω_1 ratios Cu from time to time, i.e. by chance, decides to exchange places with a neighboring vacancy which likes to jump around it. After the exchange Cu does not tend to perform a reverse jump and in addition, from the Cu point of view, the vacancy is always free to leave Cu or to come back. Summing up this behavior means that Cu and vacancies are hardly correlated which can be seen from the large f_2 values in the range of 0.89 (400 K) and 0.99 (400 K) [43] in tables 6.1 and 2.3 .

In sum it does not seem surprising that Cu and Mg exhibit relatively similar diffusion coefficients (figure 2.15(b)). On the one hand Mg and a neighboring vacancy perform many reverse jumps which cancel each other and therefore do not contribute to a net Mg diffusion in x-direction. On the other hand most exchanges of Cu with a vacancy, no matter how unlikely, contribute to a net Cu diffusion. Hence one can assume that Mg normally diffuses together with a vacancy. Cu in contrast diffuses independently and at random, but often has the possibility as soon as a vacancy is nearby because of the vacancy that likes to jump around it (large ω_1).

Solute Si atoms in Al for sure behave differently with vacancies than Mg and Cu atoms as can be seen from table 6.1. Si is smaller than Al, but possesses a higher valency (+4) and is no TM. This means that no size effect can be the reason for its attractive δH_B of -5 kJ/mol [55] or -10.6 kJ/mol [43]. This is also indicated by the largest ω_4/ω_3 ratios compared to Mg and Cu. In comparison to Mg the ω_1 values of Si are much larger, but still remain far below the Cu results. On the other hand Si exhibits the largest H_M^B (table 2.2) resulting in an ω_2 value which is much lower than ω_2 of Mg and seems to be in the same order of magnitude as Cu, compare to tables 2.3 and 6.1. The resulting ω_2/ω_1 ratios roughly between $\sim$0.56 [43] and $\sim$1.82 (400K) signify that Si likes to exchange places with vacancies from time to time (ω_2), but the vacancies just as much like to jump around Si (ω_1).

These interpretations might explain why the diffusion coefficient of Si D_{Si} is found to be slightly larger than the one of Mg and Cu (figure 2.15(b)). On the one hand Si attracts vacancies, i.e. they like to jump in its vicinity, and on the other hand vacancies also like to jump around Si which means that Si gets a couple of chances to exchange places with a vacancy. Furthermore, other than Mg and due to the low ω_2, Si does not really prefer to jump back, i.e. make a reverse jump. But due to its attraction to Si the vacancy still might stay nearby for some time longer, i.e. continues to jump around it, so that Si again gets a chance to diffuse and in sum more net jumps in x-direction are the consequence than Mg or Cu are able to perform.

6.1.1.2 Mg, Si and Cu in AA6061

It should be possible now to link these interpretations to the theories which try to describe the Mg-Si co-cluster formation during NA which is believed to be the reason for the negative effect of NPA on subsequent AA. Chang and Banhart [5] already proposed a reasonable scenario based on their DSC results (section 2.1.2.1). During the quench Mg and Si might be able to form solute/vacancy complexes because of the following reasons: Si attracts vacancies most and is for sure able to hold them nearby for some time for the same reasons as discussed above, i.e. Si hinders them from annihilating. Mg on the other hand does not really attract vacancies, but as soon as a vacancy crosses a Mg position on its annihilation path, Mg will not let it pass as it wants to exchange places with it, i.e. Mg holds it nearby. Regarding Cu, Cu does barely attract vacancies and if they should cross its path during annihilating, some vacancies might like to jump around Cu for some time before they leave Cu again. At RT many vacancies have been bound to Si, Mg and Cu due to different reasons. During NA Si is now able to dominate the precipitation process as it could bind most vacancies. Si further more easily allows vacancies to leave it and help other (Si) atoms to diffuse. As a consequence Si forms the from Chang and Banhart [5] proposed Si-rich agglomerates, called C1, from which the vacancies detach easily.

Till shortly after the quench some Mg atoms might have already been able to cluster, i.e. form the C0 clusters which were found by Chang and Banhart [5]. But only with prolonged NA time most Mg atoms are able to contribute to the diffusion process as it takes time for the Mg atoms to diffuse far enough due to the many reverse jumps Mg performs with the vacancy attached to it. This might coincide with the NA period when the Mg-Si co-cluster formation starts.

Summing up it is thought very reasonable that vacancies become imprisoned in Mg-Si co-clusters as proposed by Pogatscher et al. [24] because Si as well as Mg like to interact with vacancies. This assumption is also in accordance with the cluster formation theory of Zurob and Seyedrezai [13], see section 2.4.2.2.

6.1.1.3 Sn, In or Cd in the Al Matrix

Sn, In and Cd are neighboring atoms in the periodic table and significantly larger than its matrix Al with $r_{Sn} > r_{In} > r_{Cd}$ as can be read out of table 2.1. In the following only Sn is treated and afterward compared to In and Cd.

As can be seen from the low f_2 values in table 6.1 and figure 6.1 Sn atoms alloyed in an Al matrix are extremely strong correlated with vacancies at all temperatures. This is because compared to Mg, Cu and Si Sn exhibits the by far largest ω_2 and ω_4 jump frequencies plus the lowest ω_1 and ω_3 values. The strong attractive binding enthalpy of Sn δH_B of $\sim$-25 kJ/mol calculated by Simonovic and Sluiter [55] (table 2.2) already indicates that Sn not easily lets a vacancy jump away again (low ω_3) as soon the vacancy comes into Sn's neighborhood. Sn even strongly attracts the vacancies to come nearby (ω_4). Comparable to Mg as soon as a vacancy is a NN of Sn, Sn starts to exchange places with it followed by many reverse jumps. In contrast to Mg these ω_2 jumps occur much more often and like that solute Sn atoms should not be able to diffuse very fast together with a vacancy. With rising temperature the ω_2/ω_1 ratio disproportionally drops from $\sim 3 \cdot 10^7$ to $\sim 2 \cdot 10^4$, but nevertheless always by far exceeds the ratios of Mg, Cu and Si.

In general In and Cd seem to behave very similar to Sn with regard to their f_2 and ω_i values. The only real difference between these three elements seems to be their δH_B, i.e. the one of In is about -21 kJ/mol [55] while Cd exhibits $\sim$-15 kJ/mol [55]. One possible influence on the higher δH_B of Sn might be that Sn possesses a valency of $+4$ in Al, i.e. an excess valancy of $+1$. Cd is a TM, but as has been treated in section 2.4.1.2 the d states of Cd behave as core states so that no hybridization happens. Because of this it might even be possible for Cd to behave similar to Sn and In in an Al matrix.

6.1.1.4 Sn, In or Cd in AA6061

How is it now possible that trace amounts of Sn, In or Cd are able to change the precipitation kinetics of the alloy AA6061 in such a fundamental way? Again only Sn is treated, but the theory might also be valid for In and Cd.

It is possible that already at the solution treatment temperature of 570 °C Sn atoms are bound to vacancies as was proposed by Čížek et al. [62] for Al-Sn alloys. It would also fit to the theory of Chang and Banhart [5] who believe that solute/vacancy complexes are formed as soon as the solute-vacancy binding energy exceeds the thermal energy, see section 2.1.2.1. Thus if the thermal energy at 570 °C is lower than δH_B of Sn with ∼-25 kJ/mol, Sn should bind vacancies. Meanwhile Mg, Si and Cu are not able to form solute/vacancy complexes at 570 °C. In pure Al a vacancy concentration c_V of about $3.5{\cdot}10^{-4}$ is expected at 570 °C (section 2.2.2). During the quench the Sn atoms stay bound to their vacancy and/or bind new ones due to the large attractive δH_B. This might go so far that Sn prevents that most other solute atoms ever get in contact with annihilating vacancies with whom these other solutes could diffuse at RT.

These thoughts lead to the following theory why solute Sn atoms prevent the clustering of Mg-Si co-clusters during RT storage. On the one hand in section 6.1.1.3 it has been assumed that Sn should be a comparably slow diffuser when attached to one vacancy due to many revers jumps. On the other hand mainly Sn atoms even should have vacancies nearby so that they should be the only solute atoms that are even able to diffuse at RT. Hence it is not surprising that the APT measurement of the alloy containing ∼195 at. ppm Sn reveals a homogeneous distribution of Mg and Si atoms after 1.2×10^6 s of RT storage compared to a long-term naturally aged AA6061 alloy without Sn in which Mg-Si co-clustering had taken place. Thus the APT results seem to verify that Sn-addition temporarily suppresses the Mg-Si co-cluster formation during NA.

In the following it is tried to explain why the different amounts of Sn atoms that have been alloyed in AA6061 for the main study measurements yielded so distinct hardening kinetics during the various heat treatments. For this theory the solubility of Sn at 570 °C in AA6061 plays a role. Already the NA results reveal that there is a difference between the ∼37 at. ppm Sn alloy, the ∼69 at. ppm Sn alloy and the two alloys containing ∼195 and ∼431 at. ppm Sn. The lowest alloyed alloy starts its hardness increase as the first one after remaining about 100.8 ks (28 hours) at the as-quenched hardness. Later, between 3.45×10^5 s (4 days) and 1.2×10^6 s (14 days) of NA, the ∼69 at. ppm Sn alloy starts hardening and at last, during the same time period, the remaining higher alloyed alloys start their hardness rise at a lower rate. During all heat treatments after different NPA times and also at diverse AA temperatures the ∼195 and ∼431 at. ppm Sn alloys follow similar hardening kinetics. This indicates that the real solubility

of Sn should lie between 69 at. ppm and 195 at. ppm which is supported by the FactSage 6.2^{TM} calculations performed in section 4.1.1 that yielded 79 at. ppm. Further the preliminary APT result of ∼94±15 at. ppm Sn solubility also point in this direction.

Assuming now that we regard, say 100 at. ppm Sn soluted in AA6061 and remaining higher alloyed amounts to be precipitated at the grain boundaries. Furthermore about 350 at. ppm vacancies are assumed to exist at the solution treatment temperature of 570 ℃ from which some not survive the quench to RT. As vacancies like to interact with Sn atoms they might be divided up between the soluted Sn atoms at this temperature. But if only ∼37 at. ppm are in the alloy there might exist an excess amount of vacancies that are attracted to Sn. So it is possible that before or during the quench more than one vacancy become bound to a Sn atom, i.e. maybe two or three. This possibility rises the lower the amount of solute Sn in the alloy. Hence in the alloy containing ∼69 at. ppm Sn fewer Sn atoms are able to bind two or three vacancies, a larger amount might only be able to bind one. So if the maximum solubility of Sn is present Sn atoms might only be bound to one or maximally two vacancies after the quench. Note that these quantifications are only used for illustrative purposes and that all these consideration do not take into account that some Sn atoms might also exist as □-Sn_2 complexes as has been proposed for Al-Cu-Sn alloys.

Sn–vacancy complexes containing more than one vacancy are thought to be thermally less stable than Sn–vacancy complexes with just one vacancy. At RT however it might be just easier for excess bound vacancies than for single bound ones to escape from Sn. These escaped vacancies are able to support the Si and Mg diffusion. Thus also a longer time at RT might initiate a release of vacancies from Sn atoms. This could be an explanation why also ∼37 at. ppm Sn are able to suppress clustering at RT for some time but then after about 28 hoursthe alloy suddenly starts hardening. As the ∼69 at. ppm Sn alloy contains less Sn atoms attached to two or three vacancies the Sn-vacancy complexes should be more stable. The maximal amount of Sn in the alloy AA6061 is capable of suppressing the Mg-Si co-cluster formation longest.

These considerations are able to easily explain how just ∼37 at. ppm Sn are able to extremely enhance the precipitation kinetics during AA at 170 ℃ after 28.8 ks (8 hours) of NPA. Compared to all other alloys the Sn–vacancy complexes are thermally least stable, but no co-clusters are formed after 28.8 ks of NPA.

The longer the NPA time the more vacancies have been released from the Sn atoms and imprisoned in Mg-Si co-clusters before AA starts, i.e. the ∼37 and ∼69 at. ppm Sn alloys more and more assimilate their AA kinetics to the reference alloy.

At higher AA temperatures like 250 ℃ after NPA for 1.2×10^6 s vacancies released from the dissolving Mg-Si co-clusters in the reference alloy (or the ∼37 at. ppm Sn alloy) are able to

annihilate fast while helping at the β'' formation. For the alloys containing ~69 or 100 at. ppm Sn in the matrix the vacancies annihilate more slowly due to continuous interactions with Sn atoms which together with the vacancies also help at the β'' formation.

As has been mentioned before the theory treated just earlier tried to explain why the different amounts of Sn atoms that have been alloyed in AA6061 yielded so distinct hardening kinetics during the various heat treatments. Thus the solubility of Cd in AA6061 which is not possible to calculate with FactSage 6.2^{TM} (table 4.2) can be discussed. Note that the OES measurement yielded a concentration of ~411 at. ppm Cd in the pretest alloy (table 4.3). Nevertheless it has been noticed that Cd seems to behave similarly as the alloy containing ~37 at. ppm Sn. Assuming that Cd atoms are also able to bind two or more vacancies a solubility of Cd in this order of magnitude is estimated, remaining higher Cd amounts are thought to be precipitated at the grain boundaries. Like for Sn the Cd/vacancy complexes containing more than one vacancy should be thermally unstable. Note that this assumption just wants to give an idea why a much larger solubitity, say 400 at. ppm, is not thought to be realistic. Maybe Cd's lower δH_B compared to Sn of -15 kJ/mol also contributes to a higher thermal instability of bound excess vacancies.

The In-added alloy seems to behave similar as the ~69 at. ppm Sn alloy. The FactSage 6.2^{TM} calculation revealed a solubility of ~34 at. ppm in AA6061. This result may indicate that In interacts still more strongly with vacancies than Sn yielding a larger proportion of thermally relative unstable solute/vacancy complexes. This assumption would be supported by the lower correlation factor f_2 calculated in table 6.1, but in reality for now it is not possible to provide an answer that is more than just speculation.

6.1.2 Other (Microalloying) Elements in AA6061

Last but not least some reasons are proposed why the other MA elements did not yield results comparable to Sn, In or Cd.

For sure one important factor is solubility. As can be seen from table 4.2 Ca, Sr, Ba, Sb, Pb and Bi are not or hardly soluble in AA6061.

As treated in section 2.5.1.4 each Ag-added system behaves in a different way. Further Ag is a TM for which hybridization effects should still play a role, see section 2.4.1.2. Although Ag is very soluble in AA6061 at 570 °C with 195200 at. ppm, it does not strongly influence the precipitation process as a trace element. This might be explained by its different interaction with vacancies.

For all other TMs (except of Zn) that are already present in the reference alloy AA6061, i.e.

Fe, Mn, Cr, Ni, Ti, V and Zr, following conclusions can be derived. According to Simonovic and Sluiter [55] the strong Al:sp-TM:d hybridization might cause higher migration barriers than for elements that do not hybridize, see section 2.4.2.1 and table 2.3. As a consequence these elements are believed to show no or hardly a correlation to vacancies, i.e. f_2 should lie around 1. Therefore supersaturated quenched-in amounts of these elements cannot influence the precipitation sequence and kinetics of AA6061 strongly due to their lack of interaction with vacancies. Thus the elements showing the strongest interactions with vacancies in AA6061, i.e. Si and Mg, determine the precipitation process.

7 Conclusions and Outlook

It was possible to give a theoretically well-founded explanation why the Mg-Si co-cluster formation in Al-Mg-Si alloys has to be assisted by quenched-in vacancies and can be influenced by microalloying elements. The developed theory is supported by the experimental results obtained out of the selected addition of microalloying elements to the technological important Al alloy AA6061. Trace additions of the elements Sn, In and Cd fundamentally changed not only natural aging kinetics but also artificial aging kinetics in a technological interesting way and even yielded significantly larger hardnesses during artificial aging. Calculations based on first principles data [43,55] gave the possibility to interpret solute-vacancy interactions in a pure Al matrix of soluted Si, Mg, Cu, Sn, In and Cd. These results were the basis for the new theory which is able to explain why Sn, In or Cd-additions to AA6061 temporarily suppress Mg-Si co-cluster formation and assist β'' precipitation during artificial aging.

Although it is believed that an important step has been done to understand the influence of microalloying elements on the precipitation behavior of Al-Mg-Si alloys a lot of open questions remain.

The most important one might be how Sn, In or Cd are able to assist the nucleation of β'' during artificial aging at 170 ℃ after various natural pre-aging periods exactly. In addition further atom probe tomography (APT) studies are required for Sn-addition to AA6061 and artificial aging at 250 ℃ after 1.2×10^6 s (14 days) of natural pre-aging.

Another open question is the influence of Sn, In or Cd-additions on the artificial aging behavior at various temperatures without previous natural pre-aging, i.e. direct artificial aging.

As Sn, In and Cd all show very limited solubility in Al alloys and especially in AA6061 the question arises how combined additions of these elements might influence the natural aging and artificial aging behavior.

Of industrial importance is for sure the question if other alloy properties are changed as well, i.e. for example ductility or corrosion resistance.

Bibliography

[1] J. Banhart, C.S.T. Chang, Z. Liang, N. Wanderka, M.D.H. Lay, and A.J. Hill. Natural aging in Al-Mg-Si alloys - A process of unexpected complexity. *Advanced Engineering Materials*, 12(7):559–571, 2010.

[2] F. Ostermann. *Anwendungstechnologie Aluminum*. Berlin: Springer-Verlag, 2007.

[3] T. Sato. Early stage phenomena and role of microalloying elements in phase decomposition of aluminum alloys. In *Materials Science Forum*, volume 331, Charlottesville, VA, USA, 2000. Trans Tech Publications, Uetikon-Zuerich, Switzerland.

[4] J. Banhart, M.D.H. Lay, C.S.T. Chang, and A.J. Hill. Kinetics of natural aging in Al-Mg-Si alloys studied by positron annihilation lifetime spectroscopy. *Physical Review B - Condensed Matter and Materials Physics*, 83(1):014101(13), 2011.

[5] C.S.T. Chang and J. Banhart. Low-temperature differential scanning calorimetry of an Al-Mg-Si Alloy. *Metallurgical and Materials Transactions A: Physical Metallurgy and Materials Science*, 42(7):1960–1964, 2011.

[6] M. Zhou, S.-c. LI, Z.-q. Zheng, and P.-y. Yang. Kinetic Monte Carlo simulation of microalloying effect in Al-Ag alloys. *Transactions of Nonferrous Metals Society of China (English Edition)*, 17(3):461–467, 2007.

[7] T. Sato, S. Hirosawa, K. Hirose, and T. Maeguchi. Roles of microalloying elements on the cluster formation in the initial stage of phase decomposition of Al-based alloys. *Metallurgical and Materials Transactions A: Physical Metallurgy and Materials Science*, 34(12):2745–2755, 2003.

[8] Ian Polmear. *Light Alloys - From Traditional Alloys to Nanocrystals*. Butterworth-Heinemann, imprint of Elsevier, fourth edition, 2006.

[9] W.F. Miao and D.E. Laughlin. Differential scanning calorimetry study of aluminum alloy 6111 with different pre-aging treatments. *Journal of Materials Science Letters*, 19(3):201–203, 2000.

[10] G.A. Edwards, K. Stiller, G.L. Dunlop, and M.J. Couper. The precipitation sequence in Al-Mg-Si alloys. *Acta Materialia*, 46(11):3893–3904, 1998.

[11] M. Murayama and K. Hono. Pre-precipitate clusters and precipitation processes in Al-Mg-Si alloys. *Acta Materialia*, 47(5):1537–1548, 1999.

[12] K. Yamada, T. Sato, and A. Kamio. Effects of quenching conditions on two-step aging behavior of Al-Mg-Si alloys. In *Materials Science Forum*, volume 331, Charlottesville, VA, USA, 2000. Trans Tech Publications, Uetikon-Zuerich, Switzerland.

[13] H.S. Zurob and H. Seyedrezai. A model for the growth of solute clusters based on vacancy trapping. *Scripta Materialia*, 61(2):141–144, 2009.

[14] A. Serizawa, S. Hirosawa, and T. Sato. Three-dimensional atom probe characterization of nanoclusters responsible for multistep aging behavior of an Al-Mg-Si alloy. *Metallurgical and Materials Transactions A: Physical Metallurgy and Materials Science*, 39(2):243–251, 2008.

[15] H.K. Hasting, W. Lefebvre, C. Marioara, J.C. Walmsley, S. Andersen, R. Holmestad, and F. Danoix. Comparative study of the β"-phase in a 6xxx Al alloy by 3DAP and HRTEM. *Surface and Interface Analysis*, 39(2-3):189–194, 2007.

[16] H.S. Hasting, A.G. Frøseth, S.J. Andersen, R. Vissers, J.C. Walmsley, C.D. Marioara, F. Danoix, W. Lefebvre, and R. Holmestad. Composition of β" precipitates in Al-Mg-Si alloys by atom probe tomography and first principles calculations. *Journal of Applied Physics*, 106(12):123527(9), 2009.

[17] H.W. Zandbergen, S.J. Andersen, and J. Jansen. Structure determination of Mg_5Si_6: particles in Al by dynamic electron diffraction studies. *Science*, 277(5330):1221–1225, 1997.

[18] S. J. Andersen, H. W. Zandbergen, J. Jansen, C. Traeholt, U. Tundal, and O. Reiso. The crystal structure of the β" phase in Al-Mg-Si alloys. *Acta Materialia*, 46(9):3283 – 3298, 1998.

[19] R. Vissers, M.A. van Huis, J. Jansen, H.W. Zandbergen, C.D. Marioara, and S.J. Andersen. The crystal structure of the β' phase in Al-Mg-Si alloys. *Acta Materialia*, 55(11):3815 – 3823, 2007.

[20] N. Maruyama, R. Uemori, N. Hashimoto, M. Saga, and M. Kikuchi. Effect of silicon addition on the composition and structure of fine-scale precipitates in Al-Mg-Si alloys. *Scripta Materialia*, 36(1):89–93, 1997.

[21] D.A. Porter and K.E. Easteriling. *Phase Transformations in Metals and Alloys*. London: Chapman & Hall, 1981.

[22] H. Zhang, Y. Wang, S.L. Shang, C. Ravi, C. Wolverton, L.Q. Chen, and Z.K. Liu. Solvus boundaries of (meta)stable phases in the Al-Mg-Si system: First-principles phonon calcu-

lations and thermodynamic modeling. *Calphad: Computer Coupling of Phase Diagrams and Thermochemistry*, 34(1):20–25, 2010.

[23] A. Ried, P. Schwellinger, and H. Bichsel. Untersuchungen über den Zwischenlagerungseffekt bei AlMgSi-Legierungen. *Aluminium*, 53:595–599, 1977.

[24] S. Pogatscher, H. Antrekowitsch, H. Leitner, T. Ebner, and P.J. Uggowitzer. Mechanisms controlling the artificial aging of Al-Mg-Si Alloys. *Acta Materialia*, 59(9):3352–3363, 2011.

[25] H. Seyedrezai, D. Grebennikov, P. Mascher, and H.S. Zurob. Study of the early stages of clustering in Al-Mg-Si alloys using the electrical resistivity measurements. *Materials Science and Engineering A*, 525(1-2):186–191, 2009.

[26] P. Haasen. *Physical Metallurgy*. Cambridge University Press, third edition, 1996.

[27] H.J. Wollenberger. Point defects. In Robert W. Cahn and Peter Haasen, editors, *Physical Metallurgy*, volume 2, chapter 18. Elsevier Science B.V., fourth, revised and enhanced edition, 1996.

[28] A. Seeger. Investigation of point defects in equilibrium concentrations with particular reference to positron annihilation techniques. *Journal of Physics F: Metal Physics*, 3(2):248–294, 1973.

[29] G.E. Murch. Diffusion in crystalline solids. In R. W. Cahn, P. Haasen, and E.J. Kramer, editors, *Materials Science and Technology*, volume 5 - Phase Transformations in Materials, chapter 2. VCH Verlagsgesellschaft mbH, 1991.

[30] T. Heumann. *Diffusion in Metallen*. Springer Verlag, 1992.

[31] K. Furukawa, J.-I. Takamura, N. Kuwana, R. Tahara, and M. Abe. Quenched-in vacancies in aluminium. *Journal of the Physical Society of Japan*, 41(5):1584–1592, 1976.

[32] R.C. Picu and Z. Xu. Vacancy concentration in Al-Mg solid solutions. *Scripta Materialia*, 57(1):45–48, 2007.

[33] F.D. Fischer, J. Svoboda, F. Appel, and E. Kozeschnik. Modeling of excess vacancy annihilation at different types of sinks. *Acta Materialia*, 59(9):3463–3472, 2011.

[34] J.E. Dorn and J.B. Mitchell. Vacancies in binary alloys. *Acta Materialia*, 14:70–73, 1966.

[35] F. Faupel and T. Hehenkamp. Calculation of impurity-vacancy and impurity-impurity interactions from enhancement of solvent and solute diffusion. *Physical Review B*, 34(4):2116–2124, 1986.

[36] F. Faupel and T. Hehenkamp. The effect of non-random solute distribution around vacancies on the enhancement of solvent and solute diffusion. *Acta Metallurgica*, 35(3):771–774, 1987.

[37] G. Bérces and I. Kovács. Vacancies and vacancy complexes in binary alloys. *Philosophical Magazine A: Physics of Condensed Matter, Structure, Defects and Mechanical Properties*, 48(6):883–901, 1983.

[38] K. Binder. Spinodal decomposition. In R. W. Cahn, P. Haasen, and E.J. Kramer, editors, *Materials Science and Technology*, volume 5 Phase Transformations in Materials, chapter 7. VCH Verlagsgesellschaft mbH, 1991.

[39] F.R. Fickett. Aluminum – 1. A review of resistive mechanisms in aluminum. *Cryogenics*, 11(5):349 – 367, 1971.

[40] C. Panseri, F. Gatto, and T. Federighi. Interaction between solute magnesium atoms and vacancies in aluminium. *Acta Metallurgica*, 6(3):198–204, 1958.

[41] C.P. Flynn. Atomic migration in monatomic crystals. *Physical Review*, 171(3):682–698, 1968.

[42] J. R. Beeler. *Radiation Effects Computer Experiments*, pages 1–9999. North-Holland, Amsterdam, 1983.

[43] M. Mantina, Y. Wang, L.Q. Chen, Z.K. Liu, and C. Wolverton. First principles impurity diffusion coefficients. *Acta Materialia*, 57(14):4102–4108, 2009.

[44] J.L. Bocquet, G. Brebec, and Y. Limoge. Diffusion in metals and alloys. In Robert W. Cahn and Peter Haasen, editors, *Physical Metallurgy*, volume 1, chapter 7. Elsevier Science B.V., fourth, revised and enhanced edition, 1996.

[45] J.R. Manning. Correlation factors for impurity diffusion. bcc, diamond, and fcc structures. *Physical Review*, 136(6A):A1758–A1766, 1964.

[46] M. Doyama. Vacancy-solute interactions in metals. *Journal of Nuclear Materials*, 69-70(C):350–361, 1978.

[47] L. F. Mondolfo. *Aluminum alloys: Structure and properties*. London and Boston Butterworths, 1976.

[48] C. Wolverton. Solute-vacancy binding in aluminum. *Acta Materialia*, 55(17):5867–5872, 2007.

[49] H. Dirkes and T. Heumann. Calculation of the free enthalpy of binding of impurity-vacancy in FCC very dilute alloys. *Journal of Physics F: Metal Physics*, 12(5):L67–L69, 1982.

[50] R.W. Balluffi and P.S. Ho. Binding energies and entropies of solute atoms and vacancies in metals. In *Diffusion; papers presented at a seminar of the American Society for Metals, October 14 and 15, 1972*. American Society for Metals, 1973.

[51] S. Hirosawa, T. Sato, A. Kamio, and H.M. Flower. Classification of the role of microalloying elements in phase decomposition of Al based alloys. *Acta Materialia*, 48(8):1797–1806, 2000.

[52] Alan Cottrell. *Concepts in the Electron Theory of Alloys*. IOM Communications Ltd, 1998.

[53] N.H. March and J.S. Rousseau. Kanzaki forces and electron theory of displaced charge in relaxed defect lattices. In *Interatomic Potentials and Simulation of Lattice Defects*, pages 111–138. Battelle Institute Materials Science Colloquia, 1972.

[54] G. Neumann. Impurity diffusion in pure metals. In *Diffusion and Defect Monograph Series*, number 7, pages 3–22, Tihany, Hung, 1983. Trans Tech Publications, Aedermannsdorf, Switz.

[55] D. Simonovic and M.H.F. Sluiter. Impurity diffusion activation energies in Al from first principles. *Physical Review B - Condensed Matter and Materials Physics*, 79(5):054304(12), 2009.

[56] I.J. Polmear. Control of precipitation processes and properties in aged aluminum alloys by microalloying. *Materials Forum*, 23:117–135, 1999.

[57] John E. Hatch. *Aluminum: properties and physical metallurgy*. Aluminum Association, ASM International, 1984.

[58] G. Erdélyi, K. Freitag, and H. Mehrer. Diffusion of tin implanted in aluminium. *Philosophical Magazine A: Physics of Condensed Matter, Structure, Defects and Mechanical Properties*, 63(6):1167–1174, 1991.

[59] D. Vanderbilt. Soft self-consistent pseudopotentials in a generalized eigenvalue formalism. *Physical Review B*, 41(11):7892–7895, 1990.

[60] G. Kresse and J. Hafner. Norm-conserving and ultrasoft pseudopotentials for first-row and transition elements. *Journal of Physics Condensed Matter*, 6(40):8245–8257, 1994.

[61] A.D. Le Claire. Correlation effects in diffusion in solids. In *Physical Chemistry*, volume 10, pages 261–330. Academic Press, New York, 1970.

[62] J. Čížek, O. Melikhova, I. Procházka, J. Kuriplach, I. Stulíková, P. Vostrý, and J. Faltus. Annealing process in quenched Al-Sn alloys: A positron annihilation study. *Physical Review B - Condensed Matter and Materials Physics*, 71(6):064106–1–064106–13, 2005.

[63] J.M. Silcock and H.M. Flower. Comments on a comparison of early and recent work on the effect of trace additions of Cd, In, or Sn on nucleation and growth of θ' in Al-Cu alloys. *Scripta Materialia*, 46(5):389–394, 2002.

[64] S. Hirosawa, T. Sato, J. Yokota, and A. Kamio. Comparison between resistivity changes and Monte Carlo simulation for GP zone formation in Al-Cu base ternary alloys. *Materials Transactions, JIM*, 39(1):139–146, 1998.

[65] L. Bourgeois, T. Wong, X.Y. Xiong, J.F. Nie, and B.C. Muddle. Interaction between Cu and Sn in the early stages of ageing of Al-1.7at.%Cu-0.01at.%Sn. *Materials Science Forum*, 519-521(1):495–500, 2006.

[66] L. Bourgeois, C. Dwyer, M. Weyland, J.-F. Nie, and B.C. Muddle. The magic thicknesses of θ' precipitates in Sn-microalloyed Al-Cu. *Acta Materialia*, 60(2):633–644, 2012.

[67] W.F. Miao and D.E. Laughlin. Effects of Cu content and preaging on precipitation characteristics in aluminum alloy 6022. *Metallurgical and Materials Transactions A: Physical Metallurgy and Materials Science*, 31(2):361–371, 2000.

Acronyms

3DAP	Three-Dimensional Atom Probe
AA	Artificial Aging
Al	Aluminum
APFIM	Atom Probe Field Ion Microscopy
APT	Atom Probe Tomography
DFT	Density-Functional Theory
DSC	Differential Scanning Calorimetry
EDX	Energy-Dispersive X-ray Spectroscopy
FCC	Face Centered Cubic
GGA	Generalized Gradient Approximation
HRTEM	High Resolution Transmission Electron Microscopy
ICP	Inductively Coupled Plasma
LDA	Local Density Approximation
LDOS	Local Density Of States
MA	Microalloying
NA	Natural Aging

NFE Nearly Free Electron
NN Nearest-Neighbor
NPA Natural Preaging

OES Optical Emission Spectrometry

PALS Positron Annihilation Lifetime Spectroscopy
PAS Positron Annihilation Spectroscopy
PFZ Precipitate-Free Zone

RT Room Temperature

Sn Tin

TEM Transmission Electron Microscopy
TM Transition Metal

VASP Vienna Ab initio Simulation Package

List of Tables

List of Figures